Position Self-Sensing in the Presence of Creep, Hysteresis, and Self-Heating for Piezoelectric Actuators

by

Mohammad Nouroz Islam

B.Sc. in Industrial and Production Engineering, Bangladesh University of Engineering and Technology, 2005
M.Sc. in Industrial and Production Engineering, Bangladesh University of Engineering and Technology, 2008

A THESIS SUBMITTED IN PARTIAL FULFILLMENT OF
THE REQUIREMENTS FOR THE DEGREE OF

DOCTOR OF PHILOSOPHY

in

THE COLLEGE OF GRADUATE STUDIES

(Mechanical Engineering)

THE UNIVERSITY OF BRITISH COLUMBIA

(Okanagan)

July 2013

Abstract

Piezoelectric ceramic actuators are widely used in micro-/nano-positioning systems due to expedient characteristics such as fast response time, high stiffness, high resolution, etc. However, nonlinear effects such as hysteresis and creep affect the position accuracy of the systems if not compensated. Often, feedback position sensors are mounted to the systems to eliminate hysteresis and creep. Nonetheless, installation of feedback sensors can be prohibitive due to space constraints, reliability and cost. Alternatively, position self-sensing techniques are used to eliminate the position sensor. In this research, the objective is to develop a position self-sensing technique considering the nonlinear effects. To model the actuators for control or self-sensing, they are often considered as capacitive elements. A novel real-time impedance measurement technique is developed based on high frequency measurements to obtain clamped capacitance. Based on the real-time measurement, an improved constitutive model and parameter identification technique is presented which includes the position dependent capacitance. As a means for position self-sensing, position is linearly related to charge. However, charge measurement is prone to drift and require sophisticated hardware to implement. The new relationship between position and capacitance opens a new avenue for non-traditional position self-sensing; however, due to measurement noise, this new technique is only useful for slow operations. In this research, a novel position observer is presented that fuses the capacitance-based self-sensing with the traditional charge-based self-sensing. This allows the position estimation over a frequency band ranges from 0Hz to 125Hz where creep and rate-dependent hysteresis are observed. The estimation error is close to 3% when compared to a position sensor. Continuous operations at frequencies larger than 20Hz contribute to self-heat generation in the actuators. This elevated temperature is detrimental to the performance and life of the actuator. In this research, a self-heat generation model is presented based on power loss in the actuator to predict the temperature rise. The predicted temperature is then used to compensate the temperature related variation in the position observer. The temperature prediction error is less than 2°C which creates a position estimation error close to 4% up to a temperature variation of 55°C.

Preface

The thesis presents the research findings on position self-sensing and control of piezoelectric actuator which was conducted in the Control and Automation Laboratory, at the School of Engineering, UBC, under supervision of Dr. Rudolf Seethaler. Part of the thesis has been published in peer-reviewed journals and conference proceedings. The contributions highlighted in the thesis are as follows:

A novel real-time piezoelectric impedance measurement technique is presented in Chapter 3 which was published in World Intellectual Property Organization in November 2012 for a patent application as "Apparatus and Method for In Situ Impedance Measurement of a Piezoelectric Actuator"[1]. The results and the measurement technique were also published in IEEE Canadian Conference for Electrical and computer engineering in 2011 as "Hysteresis independent on-line capacitance measurement for piezoelectric stack actuators"[2]. The technique was developed by Dr. Seethaler while I was responsible for experimental validation and writing the conference manuscript.

In Chapter 4, an improved electromechanical model for piezoelectric actuators is presented that employs the real-time impedance measurement technique developed in Chapter 3. Part of the chapter was published in the Journal of Intelligent Material, Systems and Structures published by Sage Journals as "An Improved Electromechanical Model and Parameter Identification Technique for Piezoelectric Actuators"[3]. The article presents a novel method to identify the pa-

[1] Rudolf J. Seethaler, and Islam, Mohammad N. "Apparatus and method for in situ impedance measurement of a piezoelectric actuator", WO2012149649, WIPO, (2012).

[2] Islam, Mohammad, N., Rudolf J., Seethaler, and Mumford, David. "Hysteresis independent on-line capacitance measurement for piezoelectric stack actuators." Electrical and Computer Engineering (CCECE), 24th Canadian Conference on. IEEE, (2011):1149–1153.

[3] Islam, Mohammad N., and Rudolf J. Seethaler. "An improved electromechanical model and parameter identification technique for piezoelectric actuators." Journal of Intelligent Material

rameters of the electromechanical piezoelectric model. My responsibility was to simulate the model, conduct experiments to validate the model and prepare the manuscript.

A novel position observer is presented in Chapter 5 which partly is published in IEEE/ASME Transaction on Mechatronics as "Sensorless Position Control for Piezoelectric Actuators Using a Hybrid Position Observer"[4]. The observer is able to predict the position of the piezoelectric actuator over a wide range of frequencies where nonlinearities such as creep and rate-dependent hysteresis take place. The results of creep and rate dependent hysteresis in open loop condition presented in this chapter is published in Review of Scientific Instruments as "Note: Position self-sensing for piezoelectric actuators in the presence of creep and rate-dependent hysteresis"[5]. Experimental results of closed loop control are presented in Chapter 6 which are partly published in IEEE/ASME Transaction on Mechatronics[4]. My roles were to conduct the experiments, analyze the data and prepare the manuscript for the articles.

Finally, a new model for self-heat generation is presented in Chapter 7 where power loss due to self-heating is yielded to estimate the temperature increase in piezoelectric actuators. A version of this chapter is submitted in Review of Scientific Instruments entitled as "Real-Time Temperature Estimation Due To Self-Heating in Piezoelectric Actuators"[6]. In this study, I developed the self-heat generation model, conduct the experimental validation of the model and prepare the manuscript for the article. In accordance to the copyright law, the published materials in the journals, transactions and conference proceedings are included with the permission of the publishers.

Systems and Structures (2013):1049–1058.

[4]Islam, Mohammad N., and Rudolf J. Seethaler. "Sensorless position control for piezoelectric actuators using a hybrid position observer." Mechatronics, IEEE/ASME Transactions on, (2013):1âĂŞ-9.

[5]Islam, Mohammad N., and Rudolf J. Seethaler. "Note: Position self-sensing for piezoelectric actuators in the presence of creep and rate-dependent hysteresis." Review of Scientific Instruments (2012): 116101–116103.

[6]Islam, Mohammad N., and Rudolf J. Seethaler. "Real-time temperature estimation due to self-heating in piezoelectric actuators." Review of Scientific Instruments(2013): submitted.

Table of Contents

List of Tables

List of Figures

Glossary of Notation

A	Surface area of the actuator.
C_P	Clamped piezoelectric capacitance.
C_T	Free piezoelectric capacitance.
C_e	Effective piezoelectric capacitance.
E	Electric field.
F	External force.
$G(s)$	Real system.
$L(s)$	Observer gain.
R_P	Piezoelectric resistance.
ΔT	Change in temperature.
Γ	Function for capacitance based position self-sensing.
α	Force-voltage proportionality constant.
$\bar{x}$	Measured piezoelectric position.
ϵ_0	Permittivity in vaccuum.
ϵ_{CCLmax}	Maximum controller error in closed loop.
ϵ_{OCLmax}	Maximum observer error in closed loop.
ϵ_{TCLmax}	Maximum total error in closed loop.
ϵ_{TOLmax}	Maximum total error in open loop.
γ	Self-heating model parameter.
$\hat{G}(s)$	Modeled system.
$\hat{x}$	Estimated piezoelectric position using an observer.
$\hat{x}_I$	Charge based position self-sensing.
$\hat{x}_{C_p}$	Capacitance based position self-sensing.

ω_s	Switiching frequency of HPO.
ρ	density.
τ	Time constant.
ζ_s	Observer damping.
a_0	Charge-position relationship slope.
b	Actuator damping.
b_0	Model intercept.
b_j	Model coefficients.
b_{Tn}	Self-heat geneation model coefficients.
c	Specific heat.
d_{33}	Piezoelectric charge/strain coefficient.
f_r	Ripple frequency.
f_s	Sampling frequency.
f_{BW}	Bandwidth.
f_{PB}	Passband width.
$f_{r_{folded}}$	Folded ripple frequency.
g	Self-heat geneation model coefficient.
k	Stiffness.
k_P	Piezoelectric stiffness.
k_T	Overall heat transfer coefficient.
k_s	Spring stiffness.
k_{33}	Piezoelectric coupling coefficient.
m	Moving mass in the test-bed.
n_f	Number of frequency folds.
n_p	Number of cycles over which Fourier transform is performed.
n_s	Number of Samples per folded ripple frequency.
q	Charge.
t_{ss}	Timespan in steady-state.
u	Hysteresis loss per driving cycle per unit volume.
x	Piezoelectric position.

Acknowledgments

I would like to express my heartiest gratitude to my thesis supervisor Dr. Rudolf Seethaler who provided me the opportunity to work on an interesting topic of piezoelectric actuators. Through his professional guidance and generous support throughout the period, the goals were possible to achieve in this study. His honest dedication to the research, attention to detail and quest for innovation has set an example in front of me which I have aimed to achieve in my professional career.

I would like to thank the members of my thesis supervisory committee Drs. Abbas Milani, Solomon Tesfamariam, and Ryozo Nagamune for their valuable comments to the research findings. I also would like to thank Drs. Lukas Bichler, Kenneth Chau and Wilson Eberle for providing access to their lab facilities.

This thesis would not be smooth without the kind and timely support of the Laboratory manager Russell LaMountain and the machinist Alex Willer who generously helped me to build the test-setup for the experiments and granted access to different tools and facilities.

I would like to acknowledge the funding support from NSERC on a strategic grant project which provided the necessary financial support throughout the period.

I also would like to thank David Mumford, from Westport Innovations Inc. for his initial support in developing test setup and setting the goals for this research. Also, I would like acknowledge the feedback of Dr. Nimal Rajapakse, the principal investigator of the project, for his valuable comments at the progress meetings.

My deepest gratitude goes to my parents who sacrificed their pleasure for the betterment of me throughout their lives. Without their continual support from a distant place, it would be extremely difficult to continue this long journey.

Finally, I would like to take the opportunity to thank my wife, Angela Nusrat for her continual support, encouragement and appreciation since I met her.

Dedication

This thesis is dedicated

to my ever caring parents

Selina Akhter

Mohd. Nazrul Islam Fakir

to my beloved wife

Angela Nusrat

and to my loving son

Nazif Islam

Chapter 1

Introduction and Literature Review

Piezoelectric ceramic actuators are widely used in micro-/nano-positioning applications due to their superior mechanical and electrical properties over traditional actuators. The active material permits miniaturization of the actuators which is a very desirable property in different micro-/nano-positioning applications. However, piezoelectric ceramic actuators suffer from nonlinearities such as hysteresis and creep which affects the positioning accuracy. Several attempts have been made earlier to address these issues by developing different models for hysteresis and creep and using these models for sensorless position control. Another branch of sensorless control is the self-sensing technique where position is reconstructed by measuring some electrical parameter such as charge, capacitance, etc. In this research, the goal is to develop a reliable position self-sensing for feedback control in the presence of hysteresis and creep nonlinearity. This eliminates the requirement of a dedicated position sensor in the actuation system. Most of the self-sensing techniques are affected by temperature variation. Hence, the effect of temperature on the position self-sensing is also investigated in this research.

This chapter provides required background for the research which includes the fundamentals of piezoelectricity, hysteresis behaviour and their modeling approaches, creep nonlinearity and modeling, actuator modeling, different position control schemes, self-sensing position estimation and self-heating phenomenon. Finally, the motivation, objective and the thesis organization is presented at the end of the chapter.

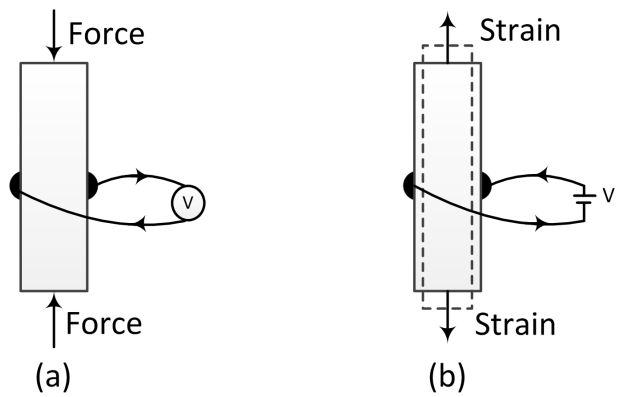

Figure 1.1: (a) Direct effect of piezoelectricity (b) indirect effect of piezoelectricity

1.1 Piezoelectricity

Piezoelectricity is a material property which generates charge when pressure is applied to the material. This property is first discovered by Jacques and Pierre Curie in 1880 during a study of charge generation due to pressure in different crystalline structures such as quartz, tourmaline, etc. [1]. The term 'piezoelectricity'is first proposed by Hankel where the prefix 'piezo' is derived from a Greek word 'piezen'which means 'to press' [1]. A reverse effect of piezoelectricity, based on the fundamental thermodynamic principles, is proposed by Lippmann in 1881 which is later verified by the Curies [1].

Thus, the piezoelectric effect is classified either as direct effect or the indirect effect. Figure 1.1 (a) shows the direct effect where electric charge or voltage is generated due to applied mechanical stress. Piezoelectric sensing applications such as displacement or force sensors are based on the direct effect of piezoelectricity. The indirect effect is shown in Figure 1.1 (b), where mechanical strain is generated due to applied electric charge or voltage. Piezoelectric actuation is based on the indirect effect of piezoelectricity [2].

The natural piezoelectric materials such as quartz, Rochelle salt etc. demonstrate little piezoelectric effect. In the 20th century, metal oxide based piezoelectric ceramic materials such as Barium titanate $BaTiO_3$ and Lead zirconate

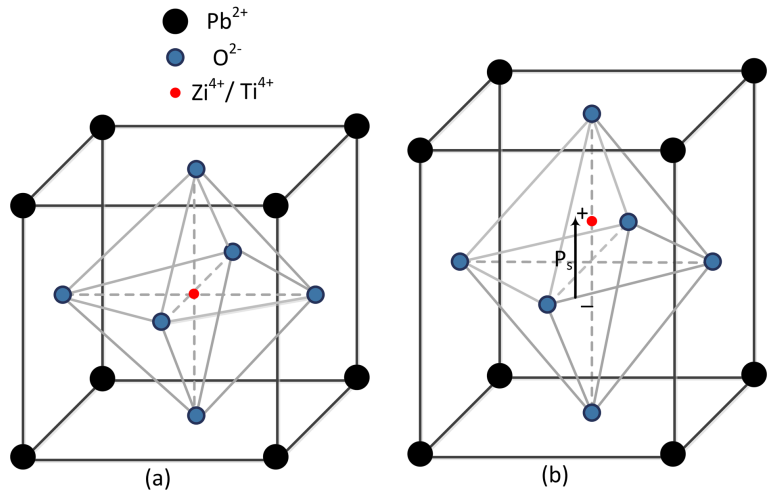

Figure 1.2: Piezoelectric crystal structure (a) Cubic (above Curie temperature, T_C) (b) Tetrahedral (below Curie temperature, T_C)[4]

titanate (PZT, $PbZi_xTi_{(1-x)}O_3$ [0 ≤ x ≤ 1]) were developed with improved piezoelectric properties. PZT is a solid solution of $PbZiO_3$ and $PbTiO_3$. Among the artificial piezoelectric materials, PZT is the most widely used for sensing and actuation due to its large sensitivity and high operating temperature in comparison to other ceramic materials [3]. The crystallographic structure of PZT materials is similar to the perovskite structure where the oxygen ions (O^{2-}) are face centered in the unit cell (Figure 1.2 (a)) [5]. There are two types of metal ions: a small tetravalent ion[4], usually Titanium (Ti^{4+}) or Zirconium (Zr^{4+}), is located in the lattice of relatively larger divalent metal ions such as Lead (Pb^{2+}) or Barium (Ba^{2+}). Depending on the temperature, the crystal structure varies. Above the Curie temperature, the perovskite crystal structure demonstrates a simple cubic shape without any dipole in the structure. However, below the critical Curie temperature, a tetragonal or a rhombohedral lattice structure is observed depending on the composition of the material. In the tetragonal or rhombohedral phase, the central Titanium (Ti^{4+}) or Zirconium (Zr^{4+}) ion is moved to one side and creates an asymmetry in the structure which leads to a spontaneous polarization, P_S. Due to the polarization, a dipole moment is created in the crystal (Figure 1.2 (b)). Regions having the same dipole direction are called Weiss do-

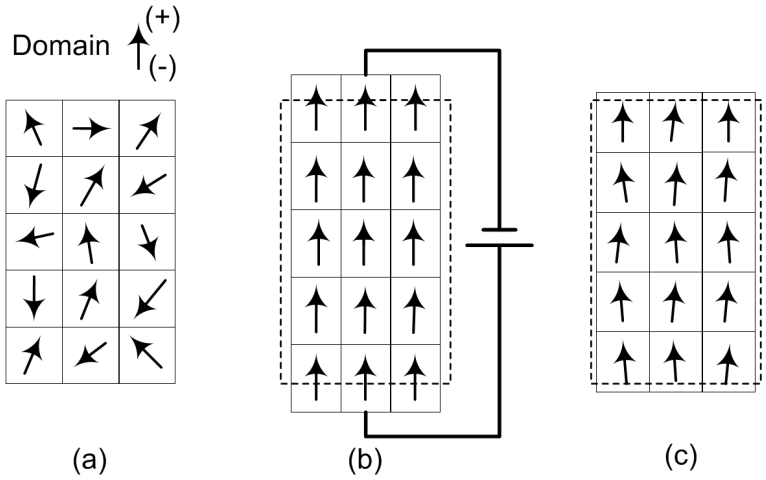

Figure 1.3: (a) No net polarization before poling (b) polarization in the direction of electric field during poling (c) polarization after poling[4]

mains [6]. Although there is a dipole moment associated with the crystal, the net effect due to the dipoles in the crystals is cancelled due to the random orientation of Weiss domains in the materials before the poling process (Figure 1.3 (a)). Hence, no piezoelectric effect is observed in the ceramic material before the poling process. To pole the ceramic material, it is heated slightly below the Curie temperature and a high DC electric field is applied to the materials. This aligns the Weiss domains in the direction of the electric field (Figure 1.3 (b)). The electric field is then removed and a permanent polarization of the material is achieved through poling in the direction of the applied electric field (Figure 1.3 (c)). Upon cooling, this polarization remains present in the material. When an electric field is applied across the Weiss domains, the domains tend to align more to the electric field direction and this changes the dimension of the material. The relationship between applied voltage and dimensional change is not linear for all types of PZT materials. Nonlinearities such as hysteresis are common in PZT materials. Moreover, the change in dimension is also a function of time for a constant electric field which results in creep. In addition to hysteresis and creep, vibrational dynamics also take place in applications near the resonant frequency. Figure 1.4 shows the change in the nonlinear behaviour of the

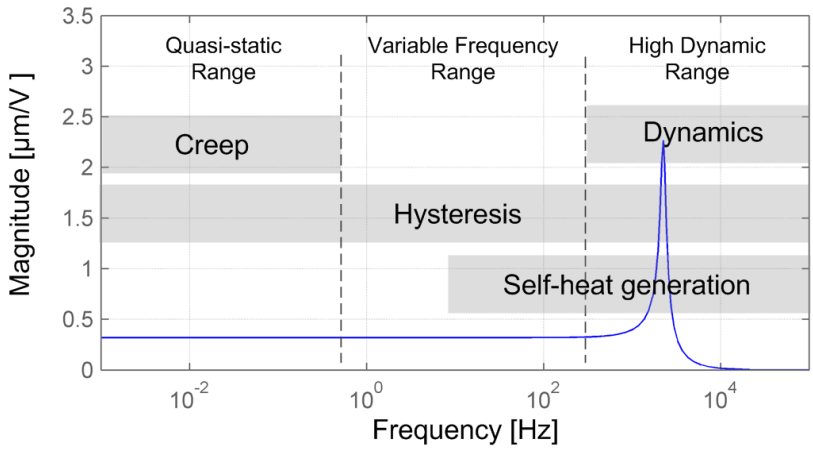

Figure 1.4: Nonlinear effects on piezoelectric actuator response at various frequencies

piezoelectric ceramics with the driving frequency. For low operating frequencies, the creep and hysteresis phenomena take place. At higher frequencies, the creep phenomenon is absent but the hysteresis phenomenon is still present. For long time continuous operation, another phenomenon named 'self-heat generation' is observed with hysteresis. These nonlinear effects are discussed in the upcoming sections.

1.2 Hysteresis

Hysteresis is a common phenomenon in piezoelectric materials due to their domain switching behaviour. It results from the rotation of the domains by either 180° or non-180° in the presence of an electric field or a mechanical stress larger than a critical value. For the non-polarized piezoelectric ceramics, the polarization-electric field (P-E) hysteresis is shown in Figure 1.5.

At point 'A', the domains are oriented randomly and hence, no net polarization is present in the element. When an electric field is applied and the domains start to align in the direction of the electric field. At point 'B' most of the domains are in the direction of the electric field. When the electric field is reversed, the polarization is not zero for zero electric field. The polarization at point 'C' is

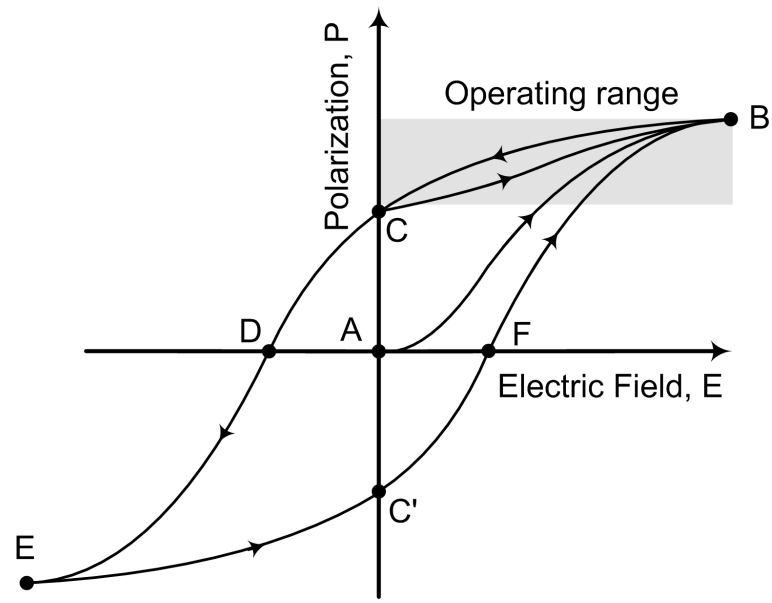

Figure 1.5: Polarization-electric field hysteresis [7]

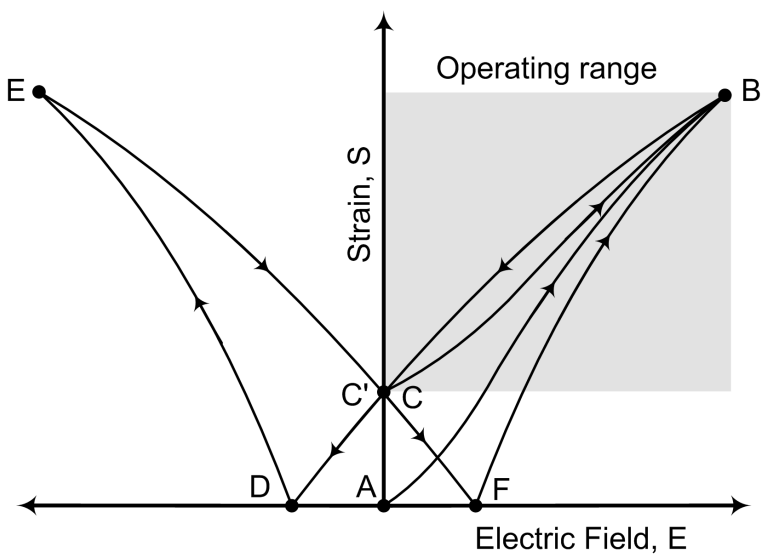

Figure 1.6: Strain-electric field hysteresis [7]

called the remnant polarization, P_r where the domains are still in the direction of the electric field as in point 'B'. To achieve zero polarization, the electric field is further reduced in the negative direction. The electric field at point 'D'is the critical value beyond which domain switching takes place. The critical value of the electric field is known as the coercive field, E_c [7]. If the electric field is further reduced, then all the domains are reoriented again in the direction of the negative electric field and reaches to point 'E' where most of the domains are in the opposite direction of the domains in point 'B'. In the reversal, at 'C', the element has negative remnant polarization, $-P_r$. At point 'F', the polarization is zero at positive coercive field, $+E_c$. The curve between 'A-B' is known as the virgin curve or initial loading curve [7]. The hysteresis loop presented by the curves 'B-C-D-E-C′-F' is commonly known as the outer hysteresis loop while the loop presented by 'B-C' is known as the inner hysteresis loop. A very well know butterfly plot (S-E) is presented in Figure 1.6 where the hysteresis between strain and electric field is shown. The points 'A-F' have the same characteristics in terms of polarization in both P-E and S-E plots. For positioning applications, the butterfly hysteresis (S-E) is more important since it shows the relationship between position and voltage. In applications, the operation region is limited to the inner hysteresis loop where unipolar electric field is applied to achieve displacement in one direction. Hence, many researchers are interested in modeling the inner loop of the piezoelectric hysteresis [7]. This will be elaborated further in Section 1.6.3 on hysteresis modeling.

1.3 Creep

The creep phenomenon is defined as the drift of the piezoelectric actuator (PEA) position over time for a constant applied voltage. This is very common in static piezoelectric operations. Figure 1.7 shows the schematic relationship of creep behavior. The creep nonlinearity is related to the change in remnant polarization (increase or decrease) due to applied voltage [8]. If the voltage change is increased the remnant polarization is also increased and continues to increase even though the voltage reaches at steady state [8]. A similar effect is observed in the opposite direction of the voltage change. Several attempts have been made

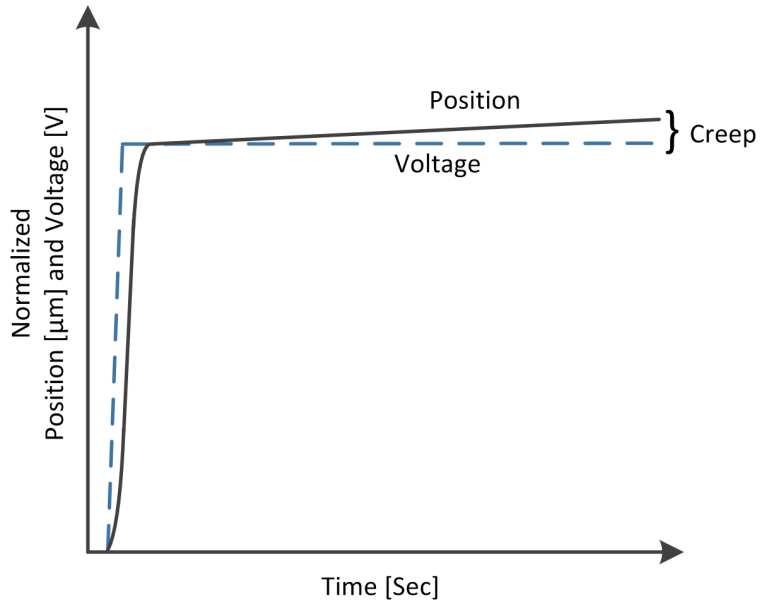

Figure 1.7: Piezoelectric creep behaviour

to model piezoelectric creep behaviour. Since creep is logarithmic with time, a nonlinear logarithmic function can represent the creep behaviour [8–10]. A nonlinear log(t)-type creep model is shown in Equation 1.1.

$$G_{Cr1} = x(t) = x_0 \left[1 + \gamma \log_{10} \frac{t}{t_0} \right] \tag{1.1}$$

where, $x(t)$ is the model output, x_0 is the nominal displacement of the actuator at t_0 seconds after applying the driving voltage, and γ is the creep parameter which defines the rate of logarithmic function [8]. A major limitation with the nonlinear creep model is that the creep rate is dependent on the time parameter, t_0 which is used to fit the model [11]. In addition to that, model inversion is not very convenient for feedforward control approaches [10].

1.4 Vibration

Vibration effects in the PEAs may occur when they are operated close to the first natural frequency of the system. In some applications, such as scanning

tubes or cantilevers, the natural frequency is low and substantial vibrations are observed. In some systems such as scanning tubes, the vibrations occur at such a low frequency that the rate-dependent hysteresis effect is modeled as a vibration effect [12]. Usually to incorporate the vibration dynamics, a second order system model is sufficient [13–15]. However, for high levels of accuracy, higher order models are used specially when pure inverse models are required for open loop control [12, 16]. The parameters of the vibration dynamic models are usually obtained through appropriate fitting of the frequency response of the actuator by selecting the order in a dynamic signal analyzer [12, 16, 17]. Usually the displacement range is limited to 10% of the stroke to neglect the hysteresis effect in measurement [16]. In contrast to scanning tube type actuators, or bending actuators, stack type actuators have a very high mechanical natural frequency. It is recommended by the manufacturer that for positioning applications of actuators, resonant frequency should be avoided [18].

1.5 Piezoelectric Actuators (PEAs)

Piezoelectric materials are extensively used as sensors, actuators, or transducers utilizing either the direct or indirect piezoelectric effect. Based on the indirect effect, an applied voltage or charge is used to create a strain in the piezoelectric system for force or position applications. Properties such as high compressive strength, fast rise time, high resolution, high pressure resistance, compactness etc. made the piezoelectric actuators (PEAs) ideal candidates for numerous micro-/nano-systems such as micro-positioning stages, inkjet-printing, surgical robots, fuel injection, drug delivery, etc. Due to advanced manufacturing technologies, piezoelectric materials can be formed almost into any shape. Different types of PEAs are developed by the manufacturers for different applications. Broadly, they are classified as rod or stack type actuators (extensional mode) and bender type or stripe actuators (flexural mode) [19] which have wide variety of applications.

1.5.1 Stack Actuators

Stack actuators are usually multilayered where several piezoelectric ceramic layers are connected in series mechanically and in parallel electrically [14]. In multilayered stack type actuators, piezoelectric ceramic layers are sandwiched between two electrodes where the polarization of the ceramics is in the opposite direction for two consecutive layers. The stack type actuators provide low strain and high blocking force. The stack actuators are classified into either discrete type or co-fired type. In discrete type actuators, separately prepared piezoelectric discs or rings are connected to the metal electrode with adhesive. The layer thickness of these actuators is usually larger than 0.1 mm (as an example in [20]). The operating voltage is usually high for these type actuators typically ranging from 500 V to 1000 V to obtain the required electric field. The co-fired actuators (monolithic type) are manufactured by high temperature sintering of the ceramic material and electrode. Since they are co-fired, the layer thickness of the ceramics can be reduced to 0.02 mm [21]. This makes it possible to drive these co-fired actuators with relatively low voltage typically less than 200 V. The construction of a multilayered stack actuator is shown in Figure 1.8.

1.5.2 Bender Actuators

In comparison to the stack type actuator, the bender type actuator provide larger displacement. The generated force for bender type actuators is small in comparison to stack actuators. The natural frequency of the benders is also small in comparison to stack actuators. The deflection in bender type of actuator is perpendicular to the electric field direction. Usually, the bender actuators consist of a piezo/metal combination or a piezo-piezo combination. In the piezo-metal combination (in Figure 1.9(a)), when the ceramic is energized the actuator deflects proportional to the voltage. This arrangement is usually used when deflection is required in a single direction. In piezo/piezo combinations, both the layers can be polarized in the same direction (parallel connection (in Figure 1.9(b))) or in opposite direction (series (in Figure 1.9(c))). In the parallel connection, the deflection is twice as large as in the series connection [22]. The piezo-piezo combination allows bending in both directions. Figure 1.9 shows

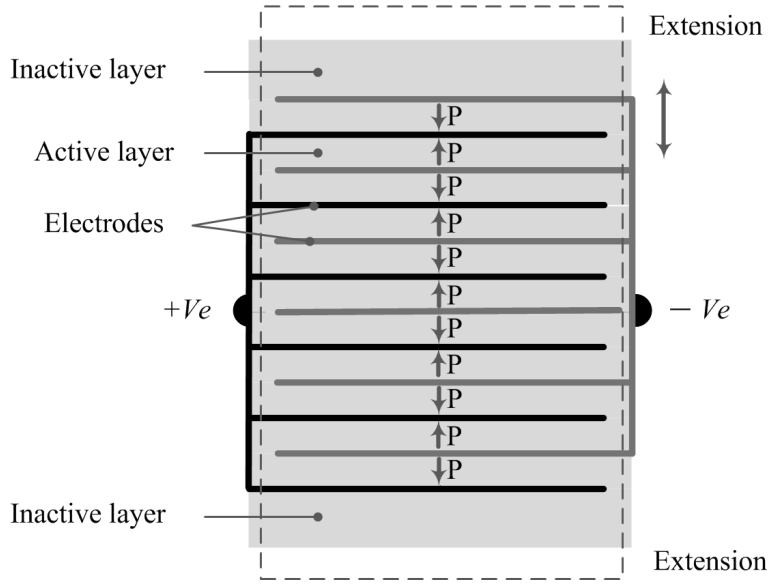

Figure 1.8: Multilayer piezoelectric stack actuator

the construction of different bender type actuators.

1.6 Piezoelectric Actuator Modeling

Piezoelectric actuator models are broadly classified into linear and nonlinear models. Linear models do not consider hysteresis or creep related nonlinearities and are applicable for hard piezoelectric materials. Nonlinear models try to incorporate hysteresis and/or creep phenomena. Phenomenological models are widely used to describe the nonlinear behaviour of the piezoelectric materials since the nonlinear effects such as creep and hysteresis and their dependencies are often difficult to describe.

1.6.1 Linear IEEE Model

In the classical description of piezoelectric constitutive equations [23], the piezoelectric materials are modeled by linear equation as follows:

$$S_\lambda = s_{\lambda\mu} T^\mu + d_{\lambda i} E^i, \tag{1.2}$$

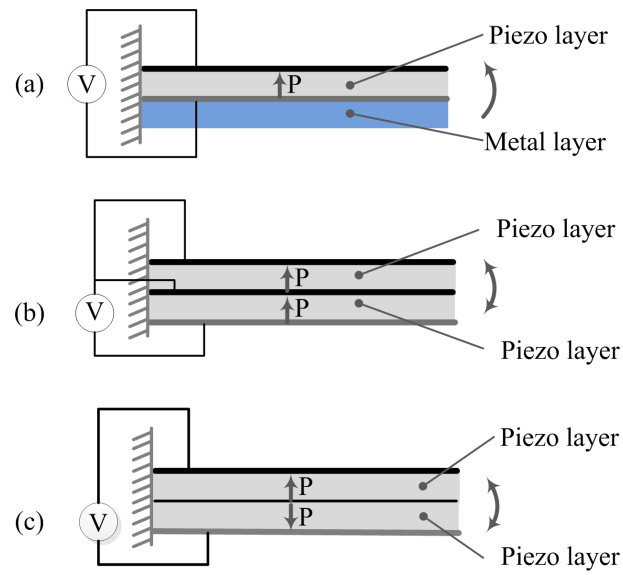

Figure 1.9: Piezoelectric bender actuator (a) Piezo-metal combination (b) Piezo-piezo combination in parallel connection (c) Piezo-piezo combination in series connection [22]

$$D_i = d_{\mu i} T^{\mu} + \epsilon_{il} E^{l}, \tag{1.3}$$

where, independent variables, T denotes the applied stress and E is the electric field which are linearly related to dependent variables, S strain and D electrical displacement with constants such as, mechanical compliance (s), piezoelectric constant (d) and dielectric constant (ϵ). The indices, λ, $\mu = 1,2,3\ldots,6$ and i, $l = 1,2,3$ are the 'tensor' expression in the material coordinate system. Based on the operating modes of the actuators, the expression can be reduced to one directional case for simplicity. It is important to note that the IEEE model does not include the dynamics of the PEA. Moreover, the piezoelectric hysteresis is not considered in the model.

1.6.2 Nonlinear Physical Model

Goldfarb and Celanovic [13] proposed an electromechanical model for PEAs that attempts to include both dynamic actuation and hysteresis effects. Since

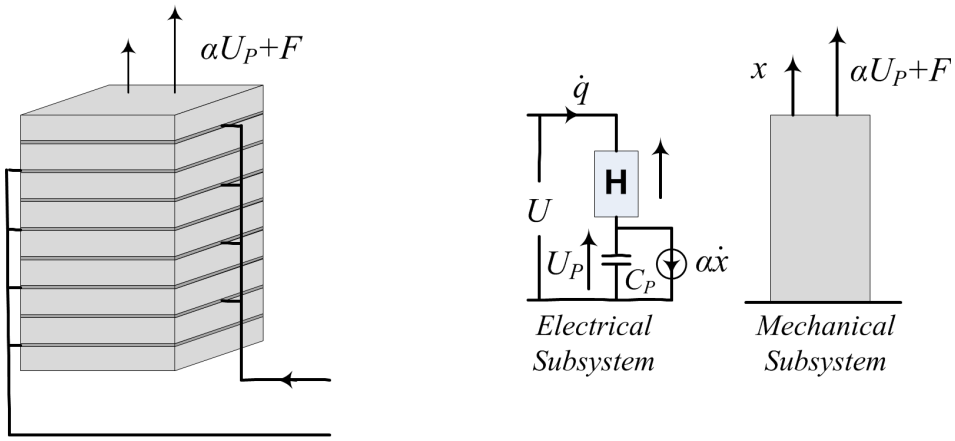

Figure 1.10: Electromechanical model of PEA [24]

their model aims to service control applications, they used readily measurable variables of voltage, charge, force and displacement instead of electric field, electric displacement, stress and strain. A diagram of this model for stack actuators is shown in Figure 1.10 and the constitutive relationships are shown in Equations 1.4-1.7:

$$m\ddot{x} + b\dot{x} + kx = \alpha U_P + F, \tag{1.4}$$

$$q = C_P U_P + \alpha x, \tag{1.5}$$

$$U = U_P + U_H, \tag{1.6}$$

$$U_H = f(q). \tag{1.7}$$

Equation 1.4 is known as the 'force equation' which models the mechanical subsystem of the actuator while Equation 1.5 is known as 'charge equation' which models the electrical subsystem of the actuator. The electrical subsystem is coupled to the mechanical subsystem with the force-voltage proportionality constant, α. In the mechanical subsystem, the generated piezoelectric force is linearly related to the linear piezo voltage, U_P through the force-voltage proportionality constant, α. In the 'force equation', both the generated piezoelectric force, αU_P and the externally applied force, F drive the second order mass-spring-damper system that is comprised of a moving mass, m, viscous damp-

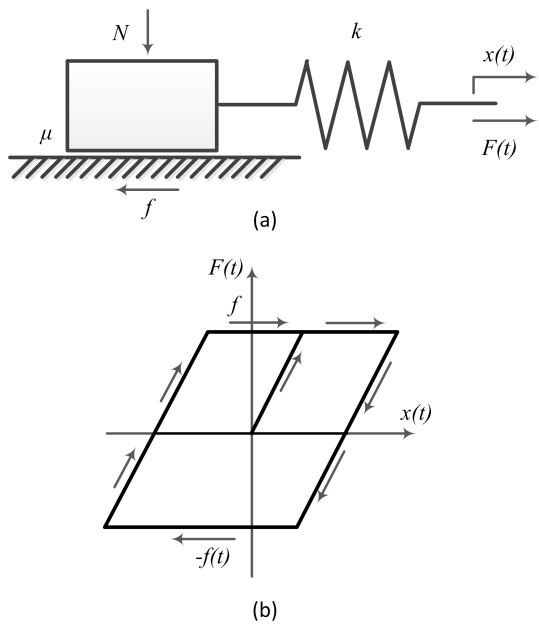

Figure 1.11: (a) An elementary elasto-slide hysteresis operator, (b) force-displacement hysteresis mapping of a single operator [13]

ing with a coefficient, b and stack stiffness, k while x, $\dot{x}$ and $\ddot{x}$ are the position, velocity and acceleration respectively. In the electrical subsystem described in the 'charge equation', the linear piezoelectric voltage, U_P results in charge, q flowing into the actuator. The charge flow is proportional to the clamped capacitance, C_P and the elongation of the actuator. To include hysteresis, a dipole, H is introduced in the electrical subsystem which reduces the voltage available to drive the actuator. This reduction in voltage occurs due to the polarization voltage associated with the dipoles within the piezoelectric ceramic [25]. The polarization voltage, U_H opposes the applied voltage, U and reduces the piezo voltage to U_P. Equation 1.6 shows that the applied voltage is a summation of the linear voltage and the polarization or hysteresis voltage. Equation 1.7 represents the hysteresis model which describes the hysteresis voltage as a function of charge. This is due to the assumption in the model that the hysteresis is solely present in the electrical subsystem. A Maxwell elasto-slide operator is the building block for the generalized Maxwell slip model which is used to capture

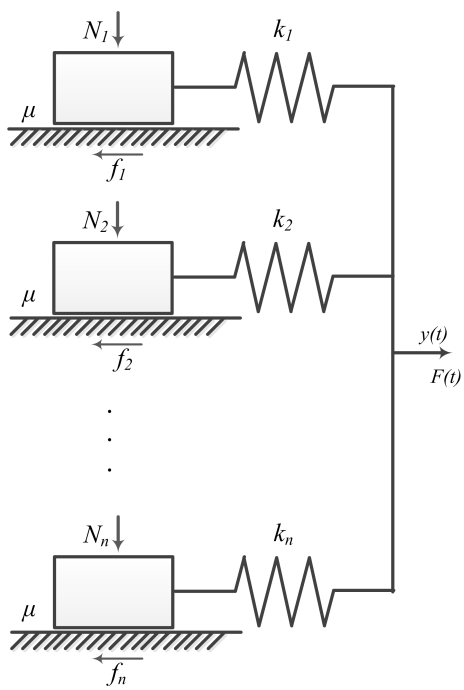

Figure 1.12: Generalized Maxwell slip model for piezoelectric hysteresis [13]

the rate-independent hysteresis behaviour in the proposed model [13]. Similar to hysteresis phenomenon observed in the elastic-plastic deformation of stress and strain in solid materials or electric field strength vs the flux density in magnetic material; the model can be used for piezoelectric hysteresis modeling. The basic model consist of massless energy storage elements such as a mechanical spring connected to a massless block. The massless system is considered sliding on a surface with Coulomb friction which is the rate-independent dissipative element in the system. This system is called a Maxwell elasto-slide operator which is presented in Figure 1.11(a). The constitutive equation of the system is shown in Equation 1.8:

$$F(t) = \begin{cases} k\{x(t) - x_b(t)\}, & k\{x(t) - x_b(t)\} < f = \mu N, \\ f sgn(\dot{x}), & else, \end{cases} \tag{1.8}$$

where, k is the stiffness of the spring, x_b is the block displacement, x is the displacement of the block which is the input, f, is the break-away friction force (μN), μ is the friction coefficient and N is the normal force. A fundamental force-displacement hysteresis behaviour, observed for a displacement input, $x(t)$ to the system, is shown in Figure 1.11. To capture the complete hysteretic behaviour, n elements are connected in parallel, where each of the elements has a monotonically increasing break-away force, f_i. The schematic of the Maxwell slip model comprising of n elasto-slide elements is shown in Figure 1.12. The complete model is shown in Equation 1.9:

$$F_i(t) = \begin{cases} k_i\{x(t) - x_{bi}(t)\}, & k\{x(t) - x_{bi}(t)\} < f_i = \mu N_i, \\ f_i sgn(\dot{x}), & else, \end{cases} \tag{1.9}$$

$$F(t) = \sum_{i=1}^{n} f_i(t) \tag{1.10}$$

where, i is the index for n number of elements connected in parallel in Figure 1.12. A similar analogy can be drawn for voltage and charge in the electrical domain which represents the piezoelectric hysteresis. In that case the stiffness term, k_i is replaced with inverse capacitance, C_i^{-1} and the input displacement is replaced with charge, q_i. The break-away force is essentially replaced with a

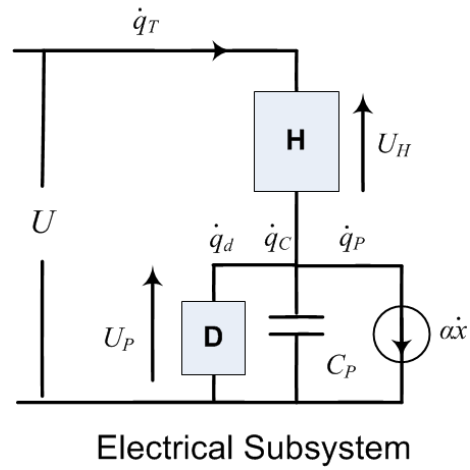

Figure 1.13: Extended electromechanical model with a drift operator [26]

break-away voltage, v_i. The equivalent constitutive model, known as Maxwell Resistive Capacitive (MRC) model, is shown in Equation 1.11:

$$U_{Hi}(t) = \begin{cases} C_i^{-1}\{q(t) - q_{bi}(t)\}, & k\{q(t) - q_{bi}(t)\} < v_i, \\ v_i sgn(\dot{q}), & else, \end{cases} \tag{1.11}$$

$$U_H(t) = \sum_{i=1}^{n} U_{Hi}(t), \tag{1.12}$$

where, U_H is the hysteresis voltage.

The electromechanical model is augmented by Adriaens et al. [14] where a mechanical operator is proposed to include the higher order dynamics for a large frequency range. To include the higher harmonics it is necessary to model the mechanical system as a distributed model instead of a lumped mass system. Also, the hysteresis behaviour is modeled with a differential equation instead of an MRC model. However, for most of the piezoelectric stack actuators, the application frequency range is well below the mechanical resonance frequency which reduces the mechanical operator into stiffness compliance [27], [28]. An extension of the model presented in [14] is proposed in [26] which accounts for the creep behaviour in addition to the hysteresis phenomenon with a drift op-

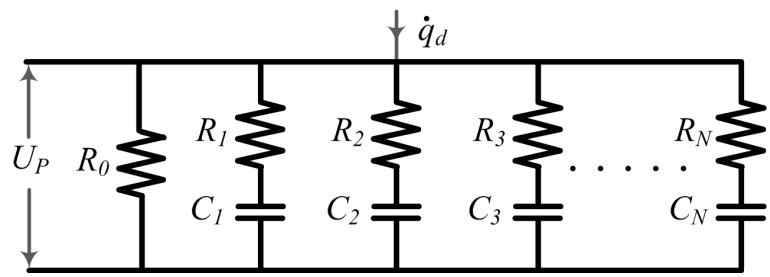

Figure 1.14: Drift operator with lossy resistance [26]

erator, D. Similar to the model presented in [13], the hysteresis phenomenon is modeled using the generalized Maxwell operator, H. The extended model with a drift operator (electrical domain) is shown in Figure 1.13.

The proposed drift operator, D consists of N number of series RC elements which are connected in parallel shown in Figure 1.14. The creep is considered similar to charge drift and hence the drift charge, q_d is obtained through the model shown in Equation 1.13:

$$G_{Cr_1}(s) = \frac{q_d(s)}{U_P(s)} = \frac{1}{Rs} + \sum_{i=1}^{N} \frac{C_i}{R_i C_i + 1}, \tag{1.13}$$

where, U_P is the linear piezoelectric voltage, R is a resistive element to account for the dielectric losses while the R_i and C_i elements model the creep behaviour. These linear models accurately predict the creep behaviour when the model starts from a known initial state. However, the past history of the hysteresis affects the creep behaviour which in not accounted in the linear models [29].

1.6.3 Phenomenological Model

The hysteresis behaviour between voltage and position attracts a large research interest since it is useful for designing feedforward controllers for position actuation applications. Figure 1.15 shows a typical hysteresis loop. It is observed that the voltage-position hysteresis phenomenon is a function of the rate of the input [27, 30–32]. Based on this, voltage-position hysteresis is classified into two groups: 1) rate-independent hysteresis and 2) rate-dependent

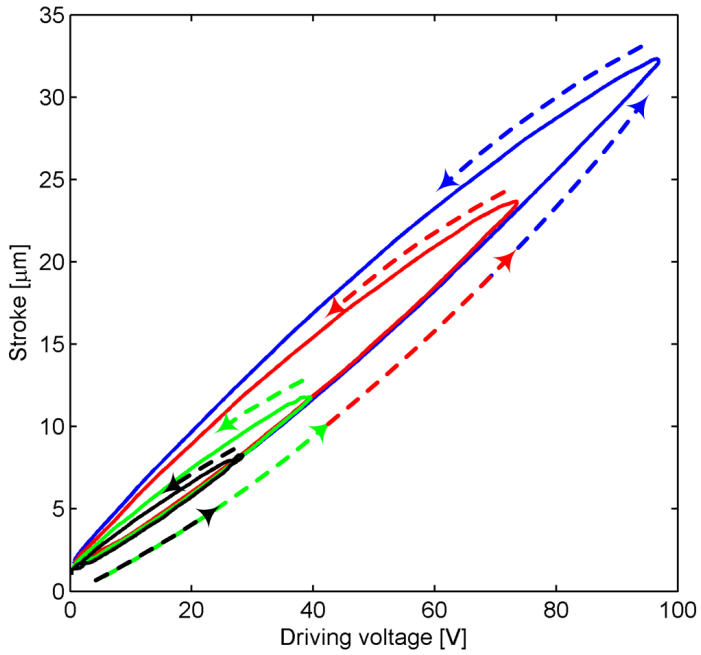

Figure 1.15: Voltage-stroke hysteresis loops at different voltages

hysteresis. The corresponding hysteresis models are then also classified as rate-dependent models and rate-independent models. The rate-independent hysteresis modeling assumes that the hysteresis behavior is not influenced by the rate of change of input or frequency. However, in practice rate dependence often plays an important role.

1.6.3.1 Rate-independent Model

Initial hysteresis models consider that the hysteresis behaviour is independent of driving frequencies or rate of operation. Several attempts were made to model the rate-independent hysteresis phenomenon. Among which, the classical Preisach model (CPM) [12, 33], and the Prandtl-Ishlinskii (PI) operator [29] are the most studied and modified. The CPM is a phenomenological model, where a function is defined to model the piezoelectric hysteresis through nu-

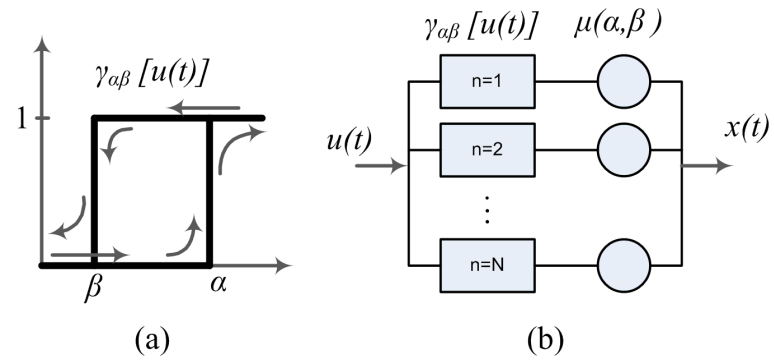

Figure 1.16: (a) Preisach operator or hysteron (b) Preisach model with N operators

merous Preisach operators, called Hysterons [34], $\gamma_{\alpha\beta}[u(t)]$ as presented in Figure 1.16 (a). For an input value, $u(t)$ larger than α, the Hysteron value is set to $+1$ and for values lower than β the value is set to -1. A weighting function, $\mu(\alpha\beta)$ is multiplied with the hysteron. Connecting the hysterons in parallel provides the output shown in Figure 1.16(b). The CPM model is realized in Equation 1.14:

$$x(t)_{CPM} = \iint_{\alpha<\beta} \mu(\alpha,\beta)\gamma_{\alpha\beta}[u(t)]d\alpha d\beta, \tag{1.14}$$

where, $x(t)$ is the output of the operator for an input of $u(t)$. The accuracy of the classical Preisach model is limited to a single operating frequency. Moreover, the smoothness of the hysteresis modeling is dependent on the number of hysterons (numerous) which is computationally expensive [28, 30].

The Prandtl-Ishlinskii (PI) model is an important sub-model of the Preisach model that is developed to address the computational complexity and inversion problem of CPM [29, 30]. The PI hysteresis model is based on the play or backlash operator which is generally used in gear backlash modeling with one degree of freedom [30]. Equation 1.15 presents an expression for the PI model with n play operators:

$$x(t)_{PI} = \sum_{i=1}^{N} \gamma^{i}_{wr}[u, y_0](t)$$

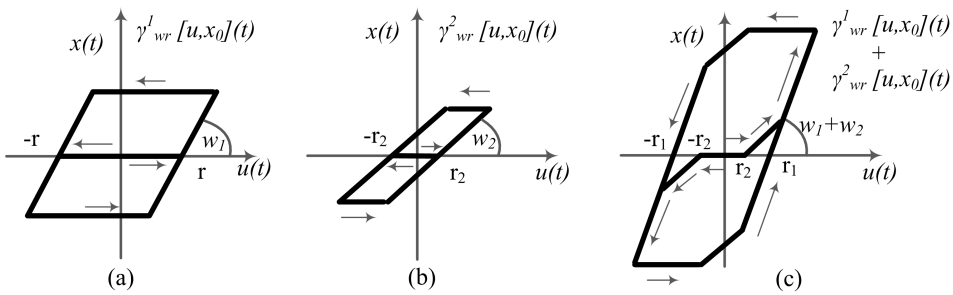

Figure 1.17: (a), (b) Elementary play operators with different weights and threshold values (c) superpositioning of the play operators in (a) and (b) [35]

$$= \sum_{i=1}^{N} w^i max\{x(t) - r^i, min\{x(t) + r^i, y(t-T)\}\} \tag{1.15}$$

where, $\gamma^i_{wr}[u, y_0](t)$ is the ith play operator with w is the weight (slope) which is the gain of the backlash operator, r is the control input threshold value, $y_0 \in R$ and usually set to zero, T is the sampling time, $u(t)$ is the model input, and $x(t)_{PI}$ is the model output. Figure 1.17 (a) and (b) show the elementary play operators with different weight functions, w and threshold values, r. A simple PI model is created by the superposition of the two play operators shown in Figure 1.17 (a) and (b), which leads to the Figure 1.17 (c).

Although the PI hysteresis model is simpler than the CPM, the classical PI is limited to the symmetric hysteresis modeling. In many practical scenarios, the piezoelectric hysteresis is not symmetric in nature. Hence a modified PI operator is proposed by [30] where a saturation operator is connected to the hysteresis operator in series. A saturation operator, defined as a superposition of weighted linear one-sided dead-zone operators, is shown in Equation 1.16:

$$\mathbf{S_d}[x](t) = [S_{d0}[x](t), S_{d2}[x](t), \cdots, S_{dm}[x](t)] \tag{1.16}$$

where,

$$S_d[x](t) = \begin{cases} max\{x(t) - d, 0\}, & for\ d > 0, \\ x(t), & for\ d = 0, \end{cases}$$

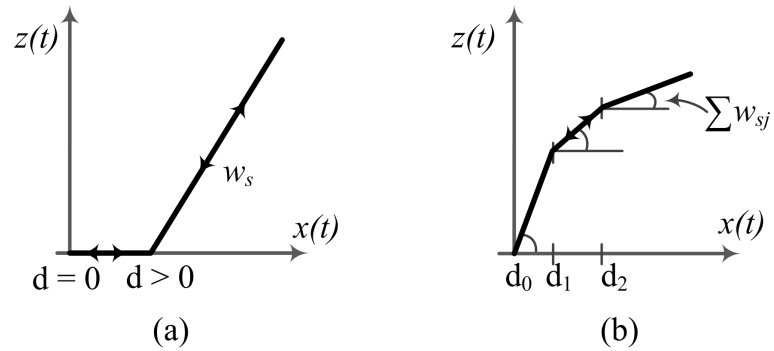

Figure 1.18: (a) a one sided dead-zone operator (b) summation of the dead-zone operators for asymmetry [30]

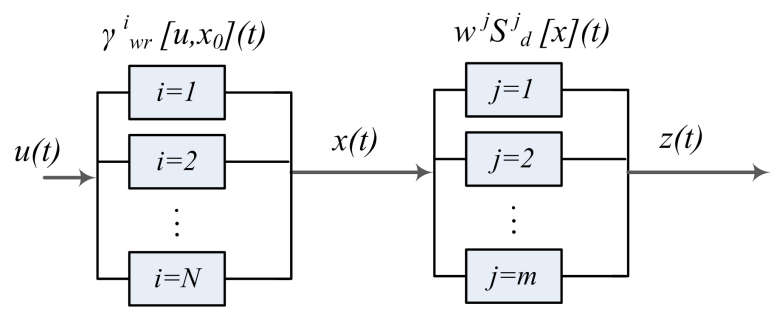

Figure 1.19: A modified structure of PI model

$$\mathbf{d} = [d_0, d_1, \cdots, d_m]^T.$$

The dead-zone operator is shown in Figure 1.18. The output of the modified PI operator for asymmetric hysteresis is shown in 1.17. The complete structure of PI operator is presented in Figure 1.19 and Equation 1.17.

$$\mathbf{z}(t)_{PI} = \mathbf{w}_s^T \mathbf{S}_d[x](t), \tag{1.17}$$

where,

$$w_s = [w_{s0}, w_{s1}, \cdots, w_{sm}]^T.$$

1.6.3.2 Rate-dependent Model

The hysteresis models discussed in the previous section are rate-independent models which can predict the hysteresis behaviour for a limited frequency range. For large frequency ranges, the aforementioned models require modifications to achieve acceptable levels of accuracy. Modifications have been suggested for both the Preisach and PI hysteresis models to incorporate the rate-dependent effects [30, 32, 33, 36, 37]. The dynamic Preisach model (DPM) includes a structure where the weighting function $\mu(\alpha, \beta)$ is modified to address the rate-dependency. This is achieved by introducing additional dynamic operators [33, 36] or a neural network [32]. The additional dynamic operators are functions which are dependent on the average input voltage between two consecutive input extrema and the rate of change of the input voltage between the input extrema [33]. Moreover, an additional function, named mirror function is defined to correlate the CPM to the DPM. The output of the DPM suggests that it is a function of both the output of the closest extremum value and the output of the CPM value at the nearest extremum. Although, it is shown that the hysteresis can be modeled over a frequency range of 0-800 Hz within reasonable error (6.4%), it required a priori knowledge of the input voltage waveform to attain the dynamic operators [33]. Unfortunately, this is not very convenient when the future input is not known. A slightly different method is proposed in [36] where the weighting function is extended to include a parameter which is a function of the rate of the input voltage. The function is simplified with the assumption that the higher order derivatives are negligible. This limits the model accuracy to a frequency range of 0.01-10 Hz. A neural network to address the rate dependency is proposed in [32]. In this case, the weighting function is modified using a neural network. It is shown that the modeling accuracy is achieved within 4% of the maximum displacement for a frequency range of 2-32 Hz. The PI model can also be modified to incorporate rate dependent phenomena [30]. The weights in Equation 1.16 are modified with the rate of actuation, $u(t)$. The percentage error for a frequency range of 1-19 Hz continuous operation is measured at 5.3%. One of the major drawbacks of the PI operators is a singularity problem when the PI weight turns to zero. A similar problem occurs if the slope is negative. Then the

preliminary assumption of a monotonically increased loading curve is violated and the model fails. In the proposed model, the singularity occurs at 40 Hz [30].

1.6.3.3 Other Phenomenological Hysteresis Models

Other phenomenological models in the literature include the Bouc-Wen (BW) model [38], the Duhem model [39], a memory based model (MBM) [40], a polynomial based model [41], a first order differential equation model, [42] etc. Although these models can predict the hysteresis behaviour, significant improvement in accuracy is not realized over the previously discussed methods. Moreover, some of these models require more complex computation in comparison to their modeling performance which limits their wide acceptability.

1.6.4 Cascaded Phenomenological Model for Hysteresis, Creep, and Vibrational Dynamics

A phenomenological model structure is proposed in [12] where the hysteresis and creep phenomena are modeled using hysteresis and creep operators. Once the models are developed they are cascaded to complete the piezoelectric model shown in Figure 1.20. In the proposed model by [12], CPM is used to model the hysteresis.

To overcome the limitations of the model described in Equation 1.1, a linear creep model is presented in [12] which is a series connection of several springs and dampers as shown in Equation 1.18:

$$G_{Cr2}(s) = \frac{x(s)}{U(s)} = \frac{1}{k_0} + \sum_{i=1}^{N} \frac{1}{c_i s + k_i}, \tag{1.18}$$

where, k_0 is the elastic constant, c_i and k_i are the dampers and springs of the ith creep element. The model is presented in Figure 1.20.

The vibrational dynamics is modeled by a higher order transfer function. To develop the complete model, first the creep submodel is constructed at low frequency condition where the vibrational dynamics is not present. Then the vibration submodel is developed at high frequencies when the creep is neglected. Finally the hysteresis model is developed and cascaded to the other submod-

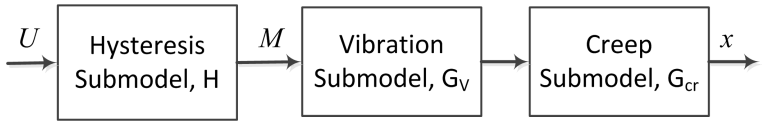

Figure 1.20: Cascaded model of PEA [12]

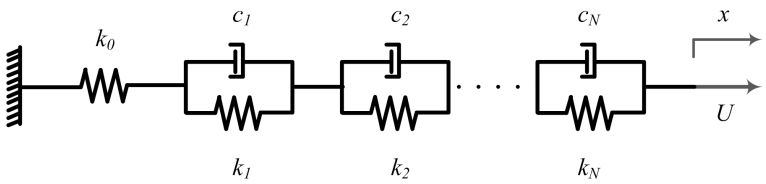

Figure 1.21: Visco-elastic creep model with elastic component [12]

els. The input voltage, U generates a mechanical output through the hysteresis model which is the input for the creep and vibration submodel. Finally, the position, x is obtained from the complete model. It is important to note that the rate-dependent hysteresis is embedded in the vibration submodel since the model is aimed for a system (piezo tube scanner for atomic force microscope) whose first natural frequency is very small (typically in the range of 500-1000 Hz). Hence, vibration occurs at relatively low frequencies even before observing considerable rate dependency in the hysteresis behaviour. The advantage of the model is that it is purely phenomenological which does not require the underlying physics for the system. Moreover, the hysteresis model is not restricted to a particular operator rather any model previously discussed (CPM, PI or MRC) can be used to represent hysteresis. Similarly, any linear model can be implemented to model the creep behaviour. The major drawback of this type of model is that the modeling uncertainty limits the accuracy of the position controller. Moreover, if the hysteresis behaviour changes due to some external factors such as temperature or aging the model cannot predict the piezoelectric behaviour accurately.

1.7 Position Control of PEA

PEAs are widely used in many micro-nano positioning applications. However, due to nonlinearities such as creep or hysteresis, position control of these

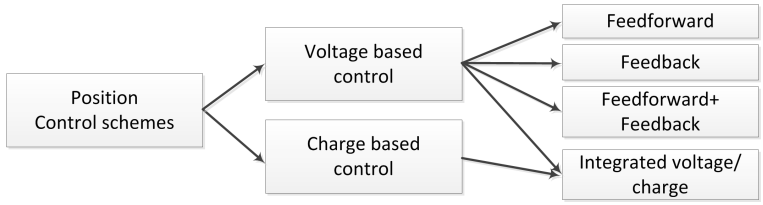

Figure 1.22: Different position control schemes

actuators is challenging. Hysteresis can result in up to 15% position error [43]. The positioning error due to creep varies from 1-40% [43, 44]. For high accuracy positioning applications, the nonlinearities must be compensated. The control schemes to counter the nonlinearities are classified into five major categories: 1) feedforward voltage control [12, 27, 30, 38, 43, 45, 46], 2) feedback voltage control [47–50], 3) feedforward with feedback control [24, 27, 47, 48, 50], 4) charge control [51–53], and 5) integrated voltage/charge control [17, 54]. The schematic shown in Figure 1.22 presents different position control principles for PEAs which are discussed in the following sub-sections.

1.7.1 Feedforward (FF) Voltage Control

Feedforward voltage control scheme is a model based control scheme where a dedicated position sensor cannot be incorporated due to space and/or cost constraints. Moreover, additional sensors can lead to reliability problems which can be avoided through a feedforward control scheme. The broad idea is presented in [12] where an accurate phenomenological model of the PEA is developed and inverted. The inverted model is then fed with the desired position, x_d input and a voltage, U_m is obtained from the inverted model. The inverted model output, U_m is the input voltage for the piezoelectric plant which is responsible for the required displacement, x. The feedforward control structure is presented in Figure 1.23. All three effects (hysteresis, creep and vibration) are considered in [12, 44] where the hysteresis is compensated by inverse CPM [12] and an inverse PI model [44], respectively. The creep is modeled by a Kelvin-viogt system in [12] and an ARMAX (Auto Regressive Moving Average with eXternal inputs) model in [44], respectively. Finally, the vibration is compensated by

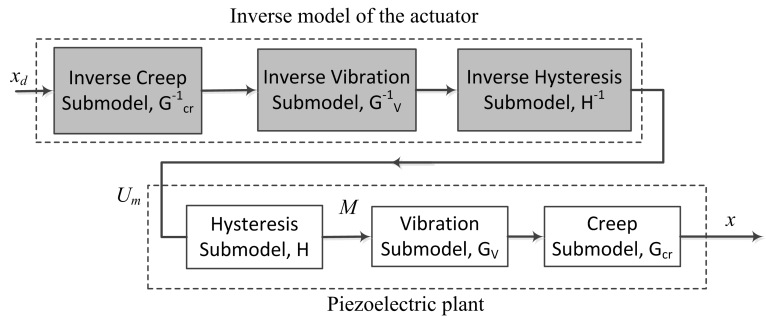

Figure 1.23: Feedforward control scheme for the PEA [12]

a higher order model obtained from a signal analyzer in [12]. In [44], the oscillations are damped with an input shaping technique. In most of the feedforward schemes, the hysteresis compensation is stressed since this is the major nonlinearity present in the piezoelectric positioning in all frequency ranges. Different hysteresis models and their inversions with rate dependent compensation is implemented by [38, 40, 46, 55]. The creep compensation is often added with the hysteresis compensation in the feedforward control scheme [10, 29, 44]. The major limitation of the feedforward approach is that the model has to be very accurate to control the position. Hence, any model uncertainty or any disturbance in the plant causes error in positioning. The other limitation of the inversion model is that the convergence of the inversion is not guaranteed all the time. To mitigate the requirement for an accurate model and in order to allow disturbances, the feedforward control scheme is often augmented with a feedback system. In the following section, the pure feedback and feedforward/feedback system is discussed.

1.7.2 Feedback (FB) Voltage Control

In applications where the space and cost in not a limiting factor, the PEA position control system is often equipped with a dedicated feedback sensor that is used to compensate for hysteresis and creep. Different sensors such as LVDT [56], capacitive probes [57], Hall sensors [58], laser interferometers [55], strain gauges [59], laser triangulation methods [60], or laser vibrometers [61], etc. are

used as position sensors. A comparison of the sensors is presented in Table 1.1 [62].

Table 1.1: Comparison of the feedback sensors

Type	Cost	Size	Precision	Resolution	Others
Triangulation	High	Large	High	High	Limited measurement range
Laser vibrometer	Very high	Large	High	High	High bandwidth, Sensor drift
Strain guage	Low	Small	Low	Medium	Fragile, temperature effect
LVDT	Low	Small	Medium	Medium	Requires contact
Capacitive or inductive probe	Low or Medium	Medium	High	High	Requires proximity
Hall effect sensor	Low or Medium	Medium or Large	Medium	High	Requires proximity

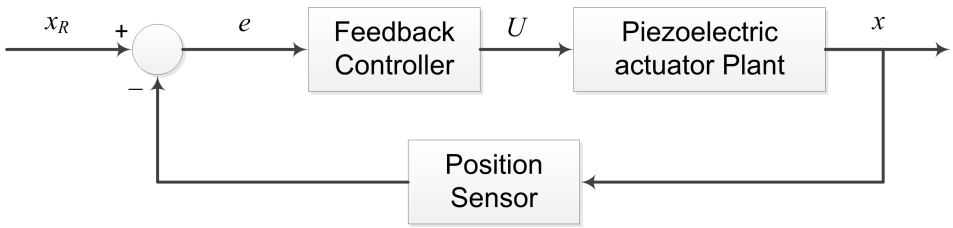

Figure 1.24: Feedback control scheme [11]

A Block diagram of the feedback (FB) control scheme is presented in Figure 1.24. For low frequency applications or point to point control, classical Proportiona-Intergral-Derivative (PID) controllers or multiple integrators are commonly used for tracking [11, 63–66]. The advantage of PID or integral controllers is that they provide high gain feedback which can substantially minimize the hysteresis and creep at low frequencies. However, at large frequencies, the PID controller is limited by the phase lag and limited gain margin [11]. This results in tracking error in classical PID controllers at high frequencies. To overcome this limitation, PID controllers can be augmented with feedforward control schemes [47, 48], or Neural networks [67]. Advanced controllers such as state feedback [60, 68] sliding model control [27], H-infinity control [69], etc. have also been developed for tracking control of PEAs.

1.7.3 Feedforward/Feedback (FF/FB) Control Scheme

To improve the gain margin of the classical PID controller, a feedforward model is often included with feedback control. This not only improves the low gain margin of the feedback control, but it also improves the performance of the feedforward control since the feedback loop accounts only for model uncertainty and plant disturbance [11]. A common feedforward/feedback control scheme is presented in Figure 1.25. This FF/FB structure is used by [15, 24, 46–48]. To model the feedforward branch, different inverse hysteresis models have been used, such as CPM [15, 48], MRC [13, 70], PI [30, 44], or Boc-Wen [46]. In [47], a high gain feedback is used to compensate for the nonlinear hysteresis and creep while the feedforward branch accounts for linear vibration dynam-

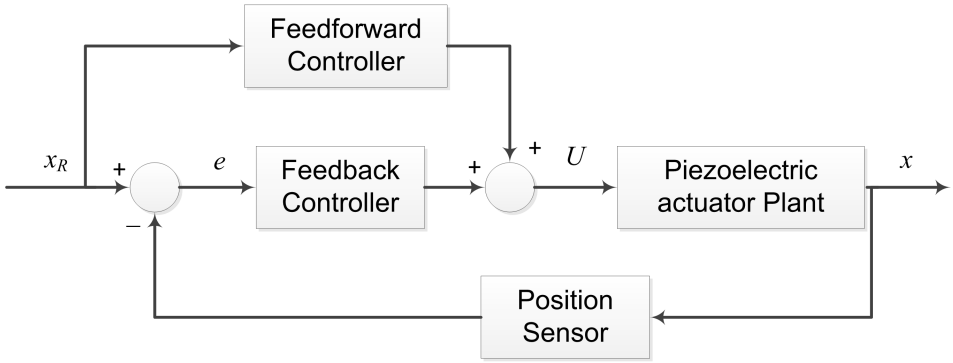

Figure 1.25: Feedforward branch with feedback control scheme [11]

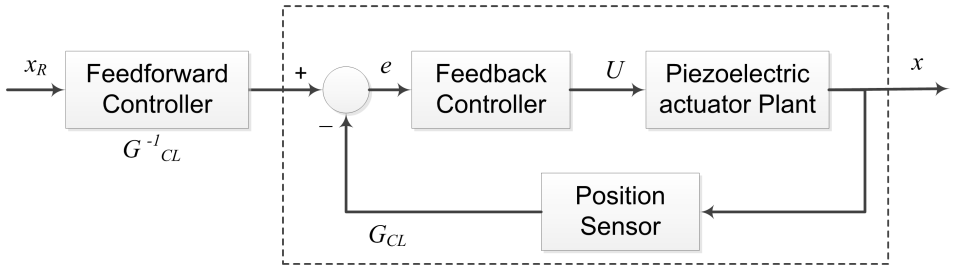

Figure 1.26: Feedback-linearized inverse feedforward control [47]

ics. Another FF/FB structure is presented in [47] and is shown in Figure 1.26. Here, an inverse model of the closed loop system is cascaded to the closed loop system. In the closed loop system, the feedback controller uses a high gain to compensate the non-linear hysteresis. Once a linearized closed loop system, G_{CL} is obtained, the feedforward branch is implemented by inverting the linear system, G_{CL} . The advantage of the system lies in the simplicity of the inversion of the linear system, G_{CL} in contrast to the inversion of the complex nonlinear hysteresis models such as CPM and higher order dynamic models. However, the low gain margin of the feedback is still present in this structure [11].

1.7.4 Charge Control Scheme

Unlike the voltage-position relationship, charge is linearly related to position in PEAs [13, 17, 53, 62]. Charge based controllers are based on this lin-

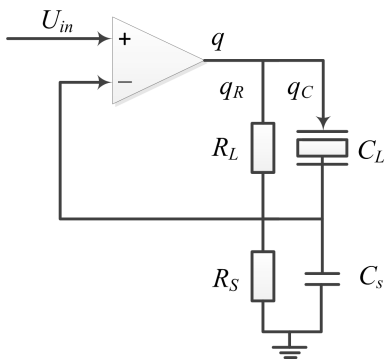

Figure 1.27: Typical charge control scheme [52]

ear charge-position relationship. Significant hysteresis reduction is possible by charge based position control. A typical charge control scheme is presented in Figure 1.27. A sensing capacitance, C_S is added to the piezoelectric capacitive load, C_L. An amplifier with a gain, K_A compensates the difference between the reference voltage, U_{in} and voltage across the sensing capacitance. To include the parasitic resistances, R_L and R_S are added to the model shown in Figure 1.27. The major problem with charge based controllers is the poor low frequency or DC performance due to charge drift. Improved charge control schemes require additional circuitry which adds complexity in the implementation [52, 53]. A different architecture for charge control is shown in [71]. In this case, additional electrode layers are added to the PEA and the induced charge in the electrodes were used for position estimation through an inverse function between charge and position. However, long-term charge drift is not considered in this study.

1.7.5 Integrated Voltage/Charge Control

An interesting integration of the charge based control and voltage based feedfroward technique is presented in [17] for piezoelectric tube scanners. In this article, the charge based technique handles the hysteresis nonlinearity while the voltage feedforward accounts for the dynamics. In this architecture, the charge amplifier is used for a traditional charge based control. This can successfully reduce the hysteresis non-linearity. However, in the presence of higher

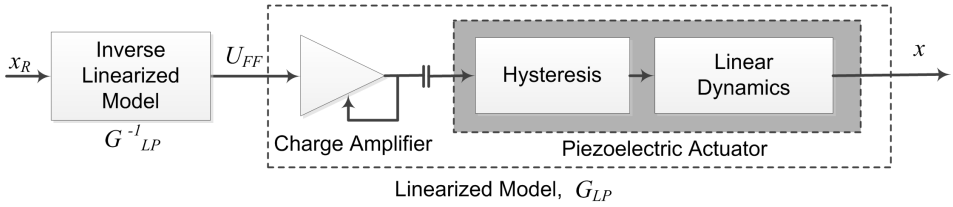

Figure 1.28: Integrated voltage/charge control [17]

dynamics, the charge based control cannot compensate for these errors. So, a simple inverse function of the hysteresis linearized charge control is developed which produces the feedforward voltage, U_{FF}. The advantage of this system is that it avoids complicated and sensitive models for vibration and hysteresis. The structure for this type of control structure is shown in Figure 1.28. However, this also requires a sophisticated charge amplifier.

1.8 Position Self-sensing (PSS)

Self-sensing is a technique where position or force is obtained in PEAs without having dedicated sensors. Such a technique is first proposed in [72] for vibration suppression of structures. Later, this technique is used in vibration suppression of beams [73–75], scanning tubes [76], etc. Self-sensing techniques are also used for position reconstruction and control applications. Broadly, the self-sensing technique can be classified into three types: 1) capacitance bridge self-sensing, 2) charge based self-sensing, and 3) piezoelectric self-sensing.

1.8.1 PSS Using Capacitance Bridge

In capacitance based self-sensing, a capacitance of equal value of the PEA is used in a capacitance bridge [72, 73]. Since, piezoelectric materials act as both sensor and actuator, in the presence of any deformation or strain in the actuator, a voltage, U_{PEA}, proportional to the strain or deformation is induced to the actuator. A schematic of the capacitance bridge is shown in Figure 1.29. The objective of the self-sensing structure is to obtain a sensing signal, U_s which is proportional to the induced voltage which can then be used as a feedback signal

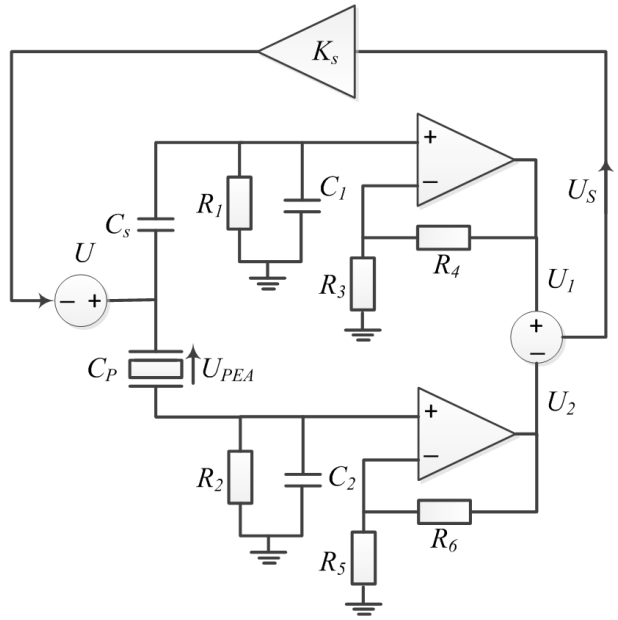

Figure 1.29: Capacitance bridge based self-sensing [73]

to control the vibration through a gain K_s. To obtain the sensing signal, a capacitance bridge is created similar to the Figure 1.29. A voltage source, U is applied to both the piezoelectric capacitive load, C_P and the reference capacitor, C_s. An induced voltage, U_{PEA} is generated due to strain in the actuator. This creates an imbalance in the bridge and the voltage difference between the two branches provides a sensing signal, U_s proportional to the induced voltage. Considering the leakage resistances, R_1 and R_2 sufficiently large and unity gain of the op-amp the following relationships can be deduced:

$$U_1 = \frac{C_s}{(C_1 + C_s)} U, \tag{1.19}$$

$$U_2 = \frac{C_P}{C_2 + C_P} (U - U_{PEA}), \tag{1.20}$$

$$U_s = U_1 - U_2 = \frac{C_s}{C_2 + C_s} U - \frac{C_P}{(C_2 + C_P)} (U - U_{PEA}). \tag{1.21}$$

Considering the ideal condition where $C_s = C_P$, the strain voltage is related to

the induced voltage as follows:

$$U_s = \frac{C_P}{C_2 + C_P} U_{PEA}. \tag{1.22}$$

The sensing signal is feedback to the source voltage and hence the vibration control is achieved. A slight variation of the similar structure is proposed where the sensing signal is obtained as a rate of change of the induced voltage [77]. Though this proposed technique is simple to implement, it has several limitations in practice. The size of the reference capacitance, C_S has to be equally large as the piezoelectric capacitance, C_P. Moreover, the temperature change has an effect on the capacitance values which demand a tedious continual tuning of the reference capacitance [73]. The other problem is to obtain an accurate piezoelectric capacitance, C_P. Hence, any mismatch in the capacitance value creates instability in the feedback control. An adaptive implementation is suggested in [78, 79] to address this problem.

1.8.2 PSS Using Charge Measurement

The other class of position self-sensing technique relies on the linear charge-position relationship [13, 17, 53, 62]. Current is integrated through a charge amplifier and the position is estimated from the charge measurement and the constitutive relationships. The estimated position can then be used in a feedback control scheme employing PID or PI controllers similar to the ones discussed in sections 1.7.4. A charge based position self-sensing structure is presented in Figure 1.30. The position is estimated in two steps: 1) an applied voltage, U_{in} produces a strain, x and charge, q. The charge is measured through an integrator circuit and a charge amplifier. Then the output voltage, U_{out}, is related to the measured charge, 2) In the second step, the position is estimated using the constitutive relationships between output voltage and charge as well as charge and position. Charge drift usually occurs when charge is obtained from current integration in the presence of any offset voltage. The position estimator in Figure 1.30 aims to compensate for this charge drift. Charge feedback approaches are presented in [25, 71].

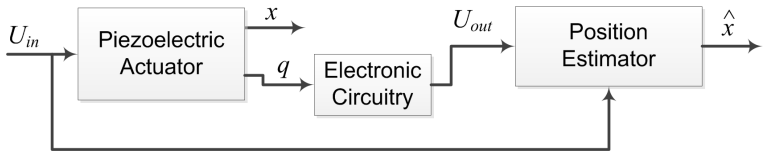

Figure 1.30: Charge based position self-sensing [80]

1.8.3 PSS Using Piezoelectricity

Position self-sensing is also obtained from the direct effect of the PEA itself. This approach is used in piezoelectric tube scanners where a part of the piezoelectric material is used for actuation while the remainder is used for sensing [81]. In this approach, the driving voltage, U creates an induced voltage, U_S in the sensing part of the tube which is proportional to the piezoelectric extension. The signal can be used for position estimation or vibration suppression in the scanners. An implementation diagram of this setup is shown in Figure 1.31. The disadvantage of this approach is that since a part of the actuator is used for sensing, the range of the actuator is reduced.

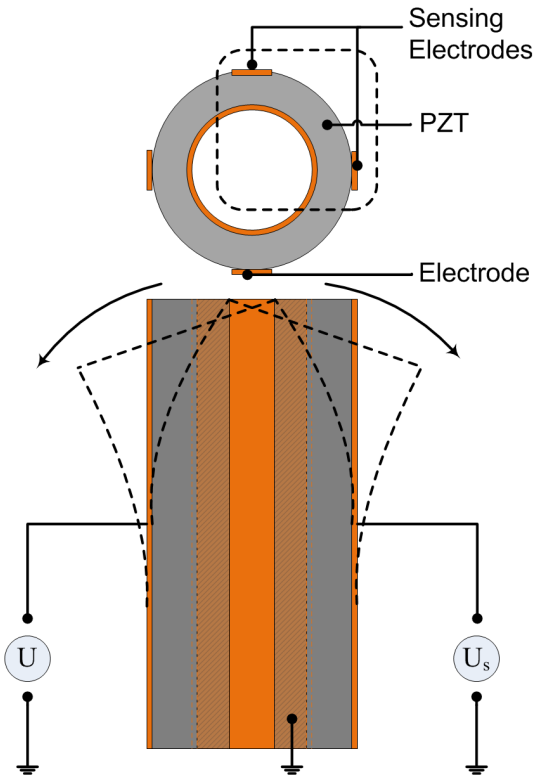

Figure 1.31: Piezoelectric position self-sensing

1.9 Errors in Piezoelectric Positioning

To verify the performance of different position controllers for PEAs, maximum tracking errors are usually compared as an indicator for improvement. For step responses, sometimes steady-state errors are also compared. There are a number of factors which may affect the performance of the controller. Among them driving frequency plays an important role, since the nonlinear effects of creep, hysteresis and vibrational dynamics appear at different frequency ranges. A number of controllers are based on feedforward phenomenological models (in Figure 1.23) only, which are designed to operate only for a limited frequency range where multiple effects are not visible. Moreover, modeling inaccuracy and plant uncertainty also affect the controller performance. To obtain a more reliable controller, often these feedforward controllers are added to a feedback controllers (in Figure 1.25) where the latter compensate for modeling inaccuracy and plant uncertainty while the feedforward model improves the dynamics of the controller [11]. Figure 1.32 shows some of performance of various position control schemes in terms of maximum tracking error where sinusoidal signals of fixed frequencies or mixed frequencies are used as a reference signal. The errors and the aim for different models presented in the literature as well as the performance of the models are presented in Table 1.2.

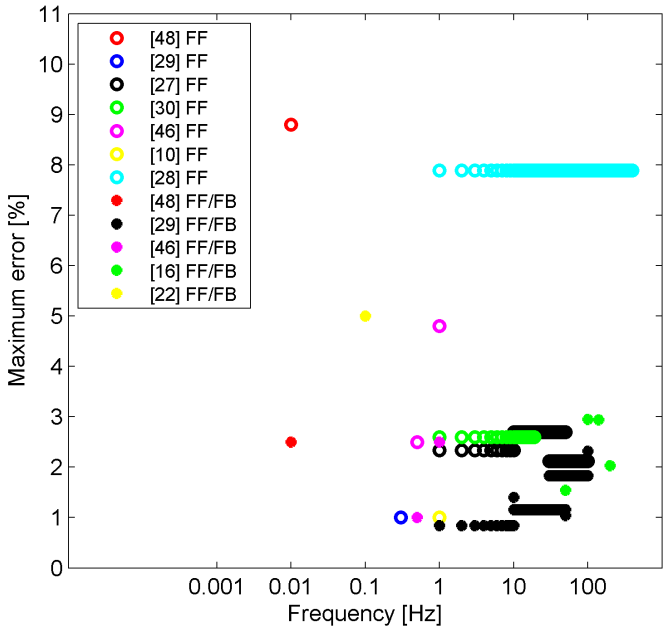

Figure 1.32: Maximum errors with operating frequencies. The circular markers indicate the FF controller while the solid markers show the FF/FB controller results.

Table 1.2: Error comparison between different models

Model type	Reference	Rate, R Hysteresis, H Creep, C Vibration, V	Control method	Type of profiles	Frequency range [Hz]	% error maximum
PI	[45]	H	FF	Sinusoidal	0.1	2.5
PI	[27]	R–H	FF FF/FB	Mixed Sinusoidal Mixed Sinusoidal	1–50 1–100	2.12–2.7 0.84–2.32
CPM	[48]	H	FF PD FB PD FB/FF	Sinusoidal	0.01	8.8 6.5 2.5
PI	[30]	R–H	OL RI FF RD FF	Mixed Sinusoidal	1–19	17.3 8 5.3
BW	[46]	H	FF FF/FB FF FF/FB	Sinusoidal Sinusoidal	0.5 1	2.6–3.1 0.88–1 4.8 2.5
MRC	[70]	H	FF/SS-FB	Trapezoidal	2 ms static 2 ms dynamic	2 3
Self-sensing	[62]	H–C	FF + Model	Step		0.55–2.5
Transfer function	[47]	H-C-V	FF FF/FB FB	Sinusoidal Triangular Step	1–300 200	4.88 2.95 1.48
Memory based	[82]	H	FF	Ramp Triangular Mixed Sinusoidal	60 sec 1	0.7 1.4 4.3
PI	[31]	R–H	FF	Multi Sinusoidal Sinusoidal	Random 12	1–6 2–3

1.10 Self-Heating

Self-heat generation is a phenomenon which occurs in PEAs when they are continuously driven at high frequency under high electric field. Substantial temperature rise is observed in [21, 83–85] which may affect the performance and durability of the actuator. Moreover, the hysteresis behavior may change due to temperature variation which affects the phenomenological model and feed-forward control of the actuator. Also, due to temperature variation, the model parameter such as piezoelectric capacitance (in Equation 1.5) is also affected. It is reported in [21] that the self-heating phenomenon is a function of frequency, electric field and effective volume of the actuator. In [83], it is shown that a temperature rise increases the current in the actuator.

Self-heat generation results from losses such as mechanical damping and dielectric losses. At high frequencies close to resonance, it is thought that the mechanical losses play a major role in heat generation while at frequencies lower than the resonance frequency, the dielectric losses contribute most to heat generation [86]. The dielectric loss is caused by the ferroelectric hysteresis loss which primarily occurs due to domain switching [84, 86, 87]. A theoretical model is proposed in [21] to model the self-heating phenomenon which is based on the law of energy conservation. The model assumes that rate of heat generation is proportional to the frequency and the hysteresis loss per driving cycle per unit volume, u. Zheng et al. [21] also studied the geometric changes in different actuators. They conclude that the steady-state temperature rise is a linear function of ratio of effective actuator volume to surface area. They also show that hysteresis varies with temperature. However, the temperature effect on the hysteresis loss is not considered in their model.

The self-heating model presented in [21] is extended in [84] which includes a heat sink attached to the actuator in order to reduce the actuator temperature due to self-heat generation. Instead of the loss term, u presented in [21], displacement hysteresis, D_f (an equivalent parameter to u calculated from the strain-electric field hysteresis) is introduced in the model. The model predicts the self-heating phenomenon in the presence of a heat sink and concludes that the self-heating temperature increase is reduced by 39% by the introduction of

the heat-sink. However, the model does not account for the mechanical losses due to friction between the heat sink and the actuator. A different temperature prediction model is proposed in [83], where it is shown that temperature change due to self-heating increases the current flow. The change in the current measurement is used to measure the change in temperature.

1.11 Scope of the Work and Objectives

PEAs exhibit rate-dependent hysteresis and creep in voltage driven scheme. These phenomena occur over a wide frequency range. Charge based operation reduces the hysteresis significantly. However, it requires sophisticated hardware to implement charge based schemes. Position feedback sensors reduce the hysteresis and creep behavior significantly. However, implementation of dedicated position sensors is sometimes prohibitive due to cost and space constraints. Researchers have developed several hysteresis models for use in feedforward position controllers. However, complex mathematical modeling is required to obtain accurate models which are often affected by uncertainty of the plant. Hence, these models are only useful for a limited range of frequencies. Piezoelectric position self-sensing provides a means to predict the position from charge information. However, charge based PSS is limited to high frequencies and prone to drift due to any offset present in the current measurement. Other self-sensing approaches have limitations such as temperature instability due to piezoelectric capacitance variation, loss of stroke, etc. In addition to that, temperature variation due to self-heat generation phenomenon substantially affects the self-sensing strategies which are not very well studied in earlier research. Considering these aspects, the main objectives in this research are:

- To develop a PSS scheme which is independent of phenomenological models of hysteresis and creep.
- To obtain a self-heat generation model for actuator temperature prediction.
- To adapt the developed PSS for temperature variation due to self-heat generation.

To achieve the main goals, several sub-goals are set. They are as follows:

- To characterize the behaviour of piezoelectric actuator, a real-time impedance measurement is required. The impedance measurement provides a novel quasi-static parameter identification technique based on the constitutive relationship.

- To obtain an improved electromechanical model with the real-time impedance measurement. The improved model is based on a position dependent capacitance which is considered constant in the original model proposed in [13].

- To obtain an improved PSS scheme that is useful over an extended frequency range. A new capacitance based self-sensing method is presented which is combined with a traditional charge based self-sensing to improve the position estimation through an observer over a wide frequency range.

- To obtain a closed loop position control system that employs the developed PSS scheme as a feedback sensor. The newly developed position observer is used as a replacement of a traditional position sensor to obtain a self-sensing control strategy.

- To obtain a sensorless temperature measurement for an improved self-sensing scheme in the presence of self-heat generation. A self-heat generation model is proposed based on the hysteresis loss relying on the constitutive relationship to predict the temperature of the actuator in the presence of self-heating.

- To obtain a temperature compensated PSS in the presence of self-heating. This is a novel contribution where a temperature compensated position self-sensing is proposed based on the self-heat generation model developed in the previous sub-goal. The arrangement provides temperature and position estimation in the presence of self-heat generation.

The objectives and sub-goals that are connected to the chapters are presented in Figure 1.33.

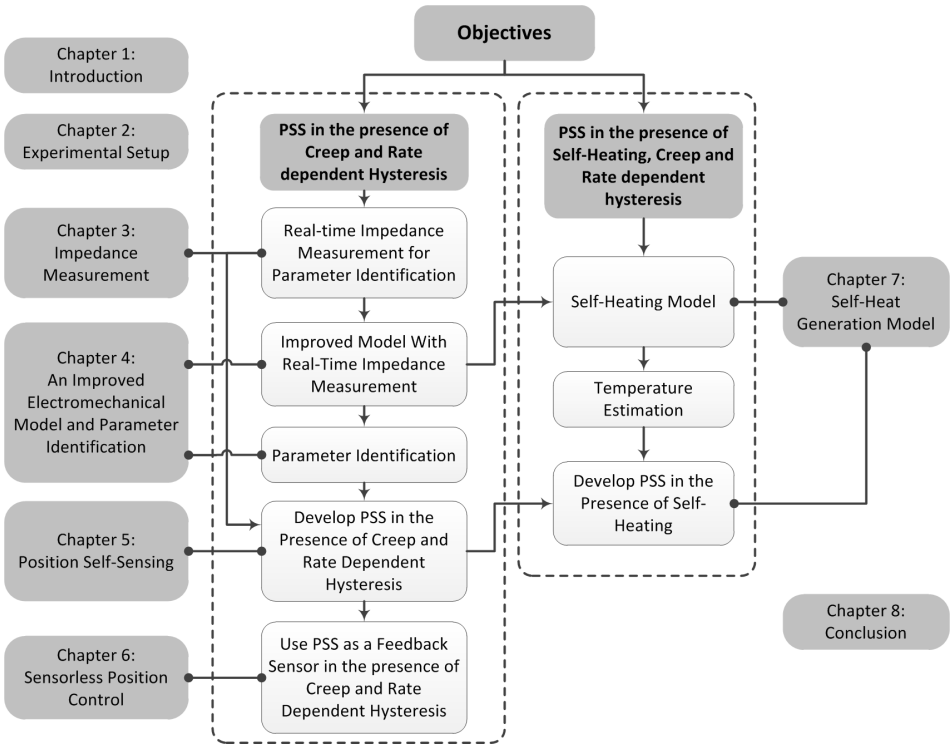

Figure 1.33: Projection of the objectives and sub-goals connected to different chapters

1.12 Thesis Organization

The chapters in this dissertation are organized as follows. The experimental setup is presented in Chapter 2 where a test-bed with a high mechanical natural frequency is designed. This allows to perform high frequency tests in the current test-bed.

In Chapter 3, a novel real-time impedance measurement technique is presented which provides impedance measurements during the normal operation of the actuator. High frequency ripple signals are superimposed on driving signals which facilitates the real-time impedance measurement. This measurement technique shows that effective actuator impedance varies with actuator stroke.

In Chapter 4, position dependent capacitance is added to the traditional electromechanical model by Goldfarb et al. [13] and the improved model is verified experimentally. The power balance is also checked and proved unaffected due to the inclusion of the position dependent capacitance. Finally, a novel method to identify the model parameters is also presented in this chapter.

In Chapter 5, the position-capacitance relationship is exploited in order to define a novel position self-sensing technique. A hybrid position observer (HPO) is presented which combines two separate position self-sensing signals: 1) charge based PSS and 2) capacitance based PSS. The charge based PSS suffers at low frequencies due to integration error while the capacitance based PSS is limited to low frequency operation due to measurement noise. Hence, the position observer yields the advantages of each PSS technique and provides an improved position self-sensing over a wide frequency range. The position observer is tested in open loop and compared with a traditional position sensor from 0 Hz to 100 Hz where creep and rate dependent hysteresis are present.

In Chapter 6, the newly developed HPO is used as a position feedback in a simple integral position controller and results are shown for single and multiple driving frequencies as well as for a scenario with actuator creep.

In Chapter 7, actuator self-heating is studied. This phenomenon occurs during continuous operation at driving frequencies higher than 20 Hz. A self-heat generation model is proposed based on the power loss of the PEA which em-

ploys the constitutive model of the PEA. The model predicts the temperature due to self-heating with 3% accuracy in the presence of different frequencies from 0 Hz to 150 Hz. Further, the presented HPO is adapted for temperature variation and employed to the self-heat generation model to predict the temperature. A circular arrangement is proposed where the predicted temperature is used to correct the temperature related variation in the HPO. HPO position estimation is then compared with a traditional position sensor in the presence of self-heat generation.

Finally, the contributions of the present research and future research recommendations are presented in Chapter 8.

Chapter 2

Experimental Setup

To investigate the characteristics and validate the model of piezoelectric actuators, an experimental test-bed is designed and manufactured. The purpose of the test stand is to facilitate the preloading of the actuator for high frequency operations (for high speed applications, the actuator manufacture recommends a preload of 15 MPa [18]) and mounting the sensors for parameter measurements. In [20], an experimental test setup is presented to characterize the piezoelectric actuator. However, the actuator used in that setup is large and the setup design require a large mass for the preloading. The large moving mass reduces the natural frequency significantly which limits the high frequency operations in that setup. Moreover, a force sensor is mounted between the large preload mass and the actuator which lowered the natural frequency even further. The natural frequency of the test-bed presented in [20] is 511 Hz. Hence, the test setup is limited to operate in the quasi-static range.

To improve the operational range, a new design presented in this research with an aim to reduce the moving mass. Also, the force sensor is moved between the PEA and the solid base in the proposed design. In addition, a soft spring is used to provide the necessary preload to the actuator. The preload assembly is redesigned which has a much smaller mass than the one in [20]. The natural frequency of the newly developed test-bed is 2500 Hz which allows high frequency operations up to 500 Hz. In the following sections, the mechanical and the electrical components of the test-bed and the experimental setup are discussed.

2.1 Mechanical Components

The mechanical components include the actuator, frame, preload assembly, needle and ball seats. The individual components are discussed below.

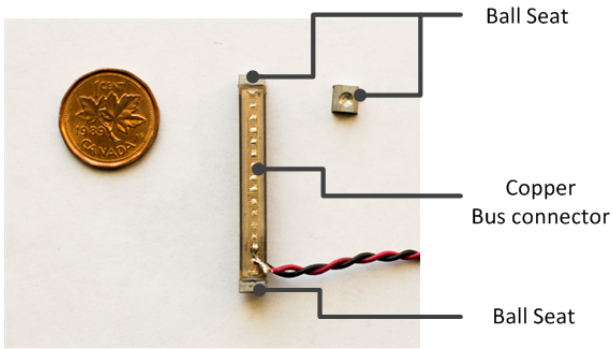

Figure 2.1: Piezoelectric actuator and ball-seats

2.1.1 Actuator

The piezoelectric stack actuator under test is manufactured by Physik Instrumente, one of the leading piezoelectric actuator and positioning device manufacturing companies in the world. A wide range of piezoelectric actuators is available for different applications. In this study, the PI-885.90 model type is used which provides a nominal displacement of 32 ± 10 μm at 100 V. The PI monolithic actuators are used in this research due to low driving voltage requirement. The properties and geometric dimensions are presented in Table 2.1. The actuator is shown in Figure 2.1.

2.1.2 Frame

The frame provides the structure of the test-bed where all the mechanical components are integrated. The frame consists of 4 plates: two vertical plates and two horizontal plates. The vertical plates (side walls) are slotted to hold the horizontal plates which are bolted from the sides. The horizontal plates (top plate and base plate) hold the whole assembly of the mechanical components, the actuator and the force sensor. The top plate has a large threaded bore to hold the preload assembly. Figure 2.2 shows the frame of the test-bed.

Table 2.1: Actuator properties [18]

Properties	Values
Actuator dimension	4.95 mm×4.67 mm × 36 mm
Stiffness	25 Nμm^{-1}
Capacitance (at 1 kHz-1V_{PP})	3.1 ± 20%μF
Blocking force	950N at 120 V
Nominal displacement	32 ±10%μm at 100 V
Operating range	-20 – 135 V
Maximum temperature	-40 – 150°C
Resonant frequency (at 1V_{PP} unloaded)	40000 Hz
Active volume (v)	740 mm^3
Surface area (A)	640 mm^2
Layer thickness (t_P)	~55 μm
Density (ρ)	7800 kg·m^{-3}
Specific heat (c)	350 J·$kg^{-1} \cdot K^{-1}$

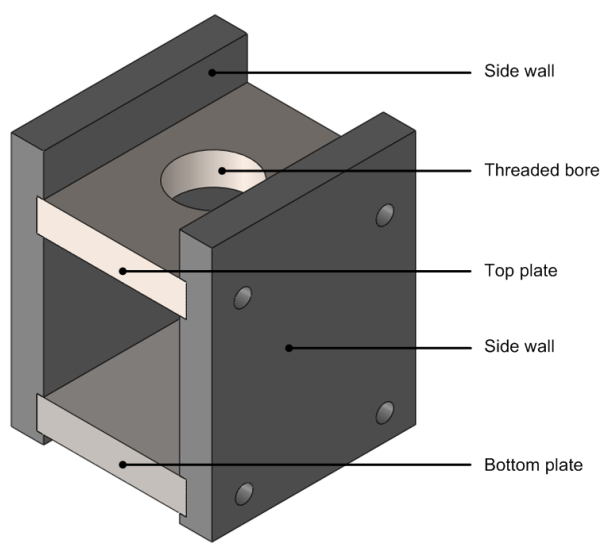

Figure 2.2: Frame of the test-bed

2.1.3 Preload Assembly

The preload assembly includes a cap, a preload plate, a thrust bearing and a steel ball attached to the needle. The cap is an essential part of the preload assembly. The top of the cap is machined to a hexagonal nut to facilitate preloading. The cap is threaded externally which fits into the threaded bore in the top plate. Figure 2.3 shows that the cross sectional view of the cap. A pocket is created inside the cap which holds the preload spring and the thrust bearing. The preload spring is a soft helical spring of stiffness 40 $\mathrm{N \cdot mm^{-1}}$. To achieve a preload of 15 MPa, 360 N force is required for the cross sectional area of the selected actuator. For a pitch of 1.5 mm, 6 turns of the cap is sufficient to provide necessary preload to the actuator. The thrust bearing prevents any torsional force (torque) to the actuator while preloading it. The spring is placed between the thrust bearing and the preload plate which provides the preload to the actuator through a steel ball. The steel ball holds the needle and it is placed on a ball seat which is attached to the actuator. Any movement in the actuator results in needle displacement.

2.1.4 Needle

A steel needle is connected to the steel ball through a tolerance fitting. Any misalignment in the needle and the preload assembly during preloading causes friction between the cap and the needle. A Teflon sleeve (in Figure 2.3) is placed between the needle and the cap which reduces the frictional force from 25 N to 5 N during the needle movement. A force sensor is used to measure the force variation during the operation. The position measurement is performed at the free end of the needle.

2.1.5 Ball Seats

While mounting the actuator in the test-bed and preloading, any misalignment may cause damage to the actuator. Hence, it is suggested to use steel balls while mounting the actuator. To facilitate the mounting of the actuator between the steel balls, end caps are attached to the piezoelectric actuator. The end caps

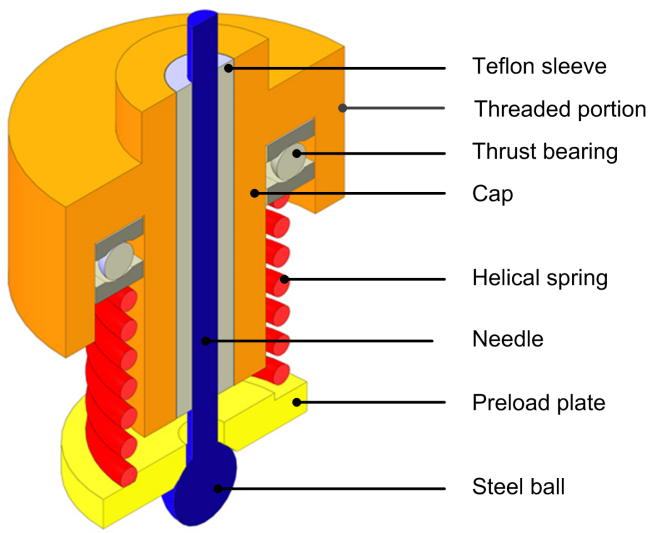

Figure 2.3: Preload assembly

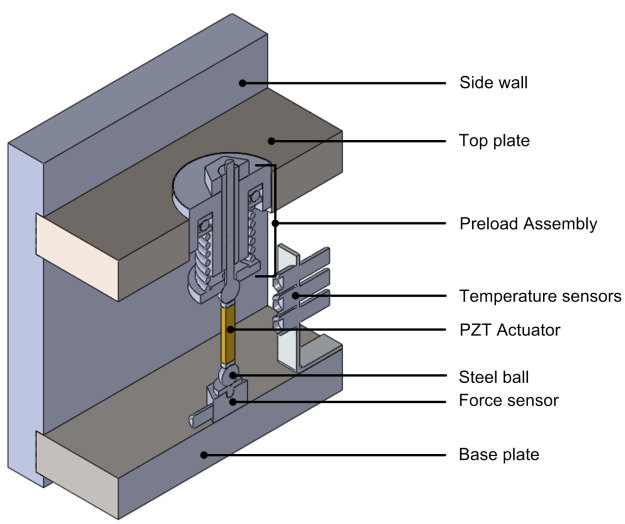

Figure 2.4: CAD drawing of the test-bed

are indented with the ball-end mills having the same radius as the steel balls to ensure a better contact between the balls and the caps. High temperature epoxy is used to attach the end caps to the actuator. The ball seats are shown in Figure 2.1. The complete test-bed is shown in Figure 2.4.

2.2 Electrical Components

The electrical components are responsible to drive the actuator, perform the measurements and data acquisition. This includes the piezoelectric amplifier which drives the actuator. Different types of sensors are used to measure current, force, position and temperature. A simple 1:100 voltage divider is used to measure the voltage signal. The measured quantities are recorded with a fast data acquisition system through dSPACE/Controldesk®. The models are run in MATLAB/SIMULINK®. The electrical components are illustrated in brief in the following subsections.

2.2.1 Piezoelectric Actuator Driver

Piezoelectric actuator driver or amplifier are required to amplify the control signal to drive the actuator. The power of the amplifier is one of the deciding factors in amplifier selection. Large driving current is required to operate the actuator at high frequencies. In this research, a high power piezoelectric amplifier (E617.00F) is used which provides 2000 mA of peak current while the average current output is 1000 mA. The amplifier has an input range of -2 to 12 V and a gain of 10. A separate 24 V DC power supply is used to feed the power amplifier.

2.2.2 Current Sensor

To measure the current flow, a high resolution (1 mA) current sensor (Tektronix TCP312) is used. Once measured, charge is calculated from the current measurement through integration in the MATLAB/SIMULINK®.

2.2.3 Force Sensor

A force sensor (PCB-208C2) is mounted at the bottom of the test setup which measures the force variation during piezoelectric actuation. The force sensor is considered stiff enough (1.05 kN·μm^{-1}) to resist the deflection due to piezoelectric actuation and hence the complete displacement is registered at the other end of the actuator which is connected to the needle. Contrary to setup presented in [20], the force sensor is not mounted between needle and actuator, but rather between actuator and frame. This has two advantages: 1) mounting the actuator is simplified, and 2) the moving mass is reduced and the bandwidth of the test-bed is increased.

2.2.4 Position Sensor

A pair of high speed laser vibrometers (Polytec-HSV2002) is employed to measure the position of the needle through a differential measurement of laser sensors. One of the sensor is used for the piezoelectric actuator movement while the other sensor is used to measure the test-bed vibration due to external sources. The differential measurement cancelled any unwanted noise present in the measurement. The resolution of the measurement system is 0.3 μm while the bandwidth of the measurement is 250 kHz. A high resolution capacitive sensor (PI D510.050) is also employed to measure the displacement of the actuator. However, the sensor bandwidth is not attractive for high speed measurements (close to the mechanical bandwidth of the test-bed).

2.2.5 Temperature Sensor

Infrared (IR) temperature sensors (Micro Epsilon CT-CF15) are used to measure the temperature change in the actuator due to self-heating or environmental temperature variation. The infrared sensors are calibrated for the piezoelectric actuator surface using thermistors at room temperature. A converging lens is used in front of the IR sensors to reduce the spot size to less than 5 mm which is the width of the actuator. Three IR sensors are used to measure the temperature at the top, middle and at the bottom of the actuator. A sensor mount is used

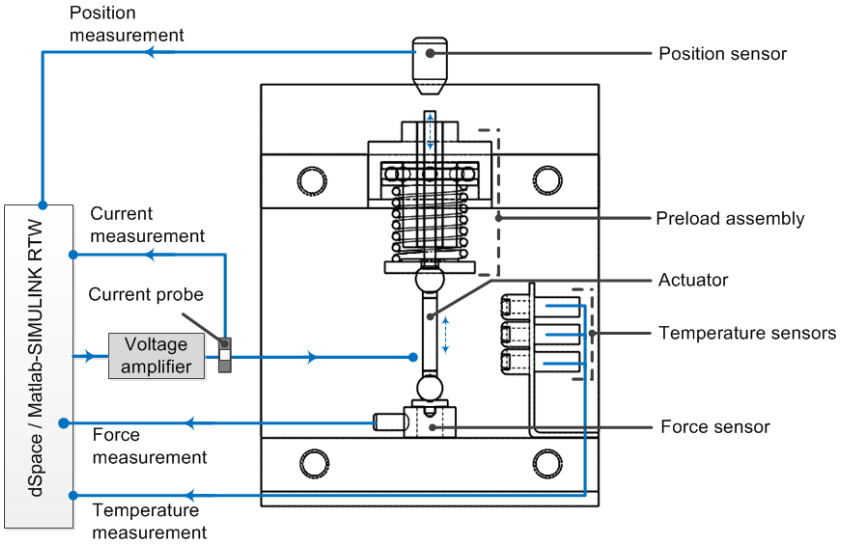

Figure 2.5: Schematic of the experimental setup

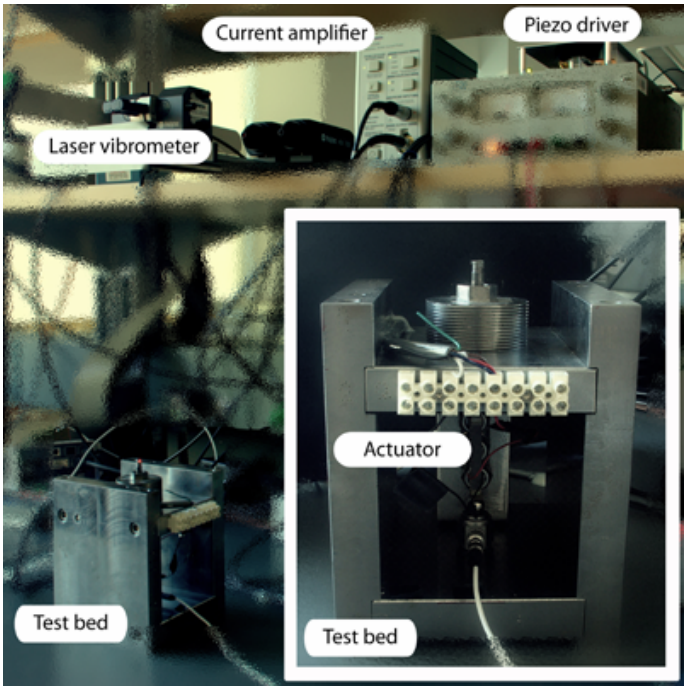

Figure 2.6: Experimental setup and the test-bed ([88] ©2013 IEEE)

which ensures the correct spacing (10 mm) between the sensors and the piezoelectric actuator surface. The complete schematic of the experimental setup is shown Figure 2.5. Figure 2.6 presents the picture of the setup and the test-bed.

2.2.6 Data Acquisition

A high speed data acquisition system (dSpace CPL1103) is employed to capture the experimental data. The experiments are modeled in SIMULINK® environment and implemented through MATLAB/Real Time Workshop®. The graphical user interface is designed in dSpace/ControlDesk® to facilitate real-time plotting and data recording.

2.3 Summary

The experimental setup that is used to characterize and test the actuator is presented in this chapter. The setup is carefully designed to provide a high operational range by reducing the moving mass in the setup. The experimental setup is divided into two major components: 1) mechanical components and 2) electrical components. The mechanical components are mostly related to the parts which facilitate the mounting of the actuator. The electrical components are responsible for measurements and data collection. The setup is used to characterize the actuator first and then the control experiments are performed on the setup.

Chapter 3

Impedance Measurement

As an electromechanical component, modeling of PEAs is an essential part in implementation of these elements in real systems. In Chapter 1 (Section 1.6.2), it is shown that in the electrical domain, the piezoelectric actuators are modeled as capacitive elements. To obtain an accurate model of the actuator, the clamped capacitance of the actuator [13, 24] needs to be measured. Usually the clamped capacitance is measured from the free capacitance. The principle of the capacitance measurement technique is simple and relies on the basic theory of electric fields:

$$C = \frac{I_{rms}}{2\pi f \cdot U_{rms}} \tag{3.1}$$

where, the root mean square (rms) value of a sinusoidal driving voltage is denoted by U_{rms}, I_{rms} is the rms value the resulting current, f is the frequency of the voltage signal, and C is the measured capacitance. This type of measurement is usually carried out at frequencies around 1 kHz. However this leads to two problems when applied to piezoelectric actuators. Firstly, the applied voltage and resultant current include charge and voltage hysteresis that distorts the capacitance measurement. Secondly, the measured capacitance is the unclamped capacitance since the actuator displaces due to the applied voltage [89]. Thus, constitutive relationships are required to convert it to the clamped capacitance value used in the standard control model by Goldfarb et al. [13]. In this chapter, a novel real-time impedance measurement technique is presented which facilitates the clamped capacitance measurement required for the model. Also, it provides an effective resistance measurement of the piezoelectric actuator.

3.1 Measurement Principle

To resolve the limitations in traditional measurements, an improved approach is proposed where a high frequency low voltage signal (termed ripple voltage in the remainder of this thesis) is used to measure the capacitance instead of a traditional low frequency signal. The ripple voltage frequency, f_r must be much larger than the resonant frequency of the test bed. This will ensure that there is no mechanical movement of the actuator due to the ripple voltage. Also, the magnitude of the ripple voltage needs to be small in order to ensure that hysteresis is minimized [90]. To yield the additional benefit of a real-time capacitance measurement, the high frequency ripple signal is superimposed with the low frequency driving signal. In this way, the capacitance measurement can take place in real-time without influencing the low frequency displacement of the actuator or vice versa. This real-time capacitance measurement is not only novel [91], but also very useful since it provides the basis for the sensorless control algorithms presented in Chapters 5. There are two possible ways to superimpose the ripple onto the driving signal: 1) using a summing circuit which merges the high frequency ripple signal with a low frequency driving signal, and 2) using a boost converters with fixed carrier frequency which provides a constant frequency ripple voltage.

3.2 Superpositioning Through Summing Circuit

A summing circuit similar to the one shown in Figure 3.1 may be used to superposition the ripple signal, U_r, on the driving voltage, U. The driving voltage, U is sourced from the piezoelectric amplifier. The ripple signal, U_r may be generated through a signal generator. Transient voltage suppression (TVS) diode is used to protect the signal generator from voltage spikes. Also, a low pass filter may be required to filter out any noise present in the driving signal. The ripple frequency is varied through a function generator.

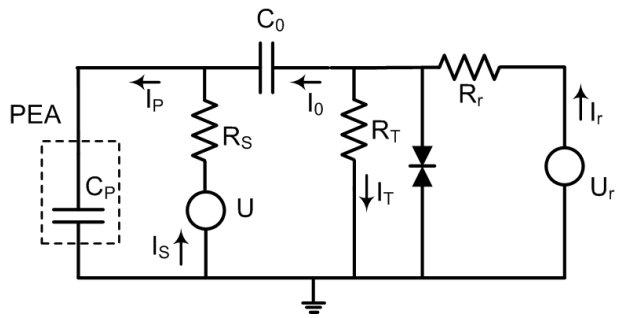

Figure 3.1: Superposition of signals through summing circuit

3.3 Superpositioning Through Boost Converter

To drive the piezoelectric actuator, a DC-DC boost converter is employed to amplify the control signal from the data acquisition board (Section 2.2.1). This amplifier automatically superimposes a high frequency ripple voltage (~0.1% of the maximum voltage range) onto the driving voltage. The magnitude and frequency of the amplifier output voltage ripple is close to ~100 mV and ~100 kHz respectively. While driving the actuator, the high frequency (~100 kHz) ripple voltage is superimposed onto the driving voltage, U, which results in a ripple current, I_r. For the test bed in this thesis, the ripple voltage, U_r does not affect the displacement of the actuator. This is due to the fact that the ripple frequency is much larger than the mechanical bandwidth (~2500 Hz) of the setup. Figure 3.2 shows the velocity of the actuator due to the ripple voltage. The free velocity is measured when the actuator is not mounted in the test-bed (mechanical bandwidth ~40 kHz) while the clamped velocity is measured when the actuator is mounted in the test-bed (mechanical bandwidth ~2500 Hz). The figure clearly indicates that the actuator shows close to zero velocity due to the ripple voltage when placed in the test-bed.

3.4 Effect of Frequency on the Actuator Capacitance

Piezoelectric capacitance measurement is largely affected by the measurement frequency. Hence, it is important to specify the frequency at which the

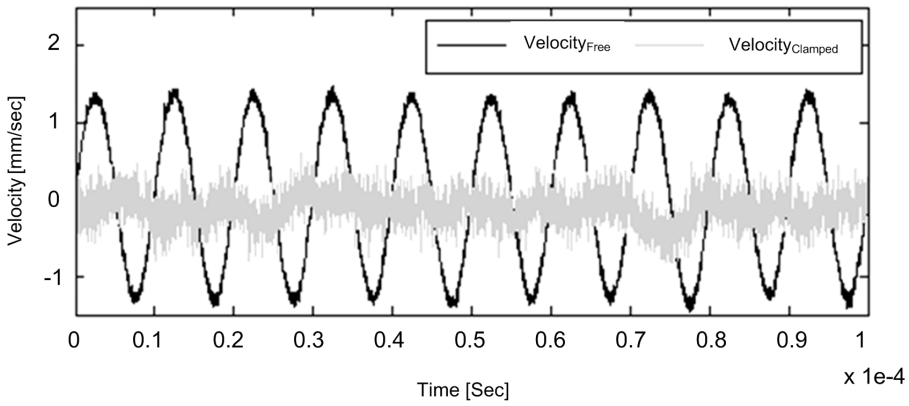

Figure 3.2: Velocity measurement in clamped and free condition [89] ©2011 IEEE

capacitance measurement takes place. The piezoelectric actuator is modeled as a pure capacitor near the driving frequency since the phase angle between the voltage, U and resultant current, I is close to 90°. The phase lag between the low frequency normalized voltage and normalized current is shown in Figure 3.3. The normalization of the signals are obtained by dividing the signals with their maximum magnitudes. So, the expressions for the capacitance measurement in Equation 3.1 are valid. However, at frequencies close to the ripple frequency of 100 kHz the phase angle between the ripple voltage, U_r and ripple current, I_r is close to 65°. The phase difference between the high frequency ripple voltage and current is presented in Figure 3.4.

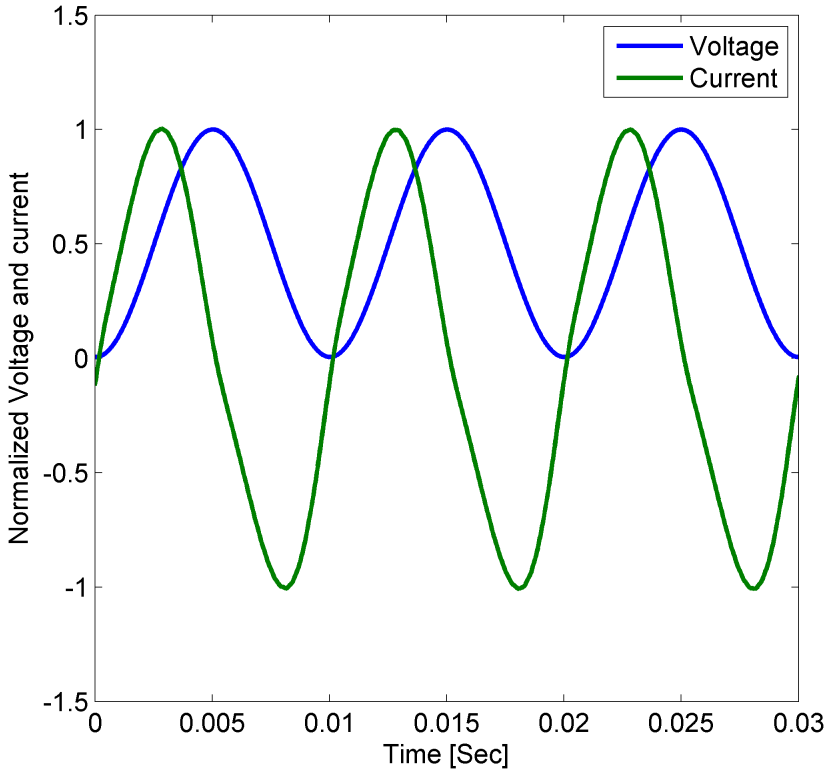

Figure 3.3: Normalized voltage and current at 10 Hz

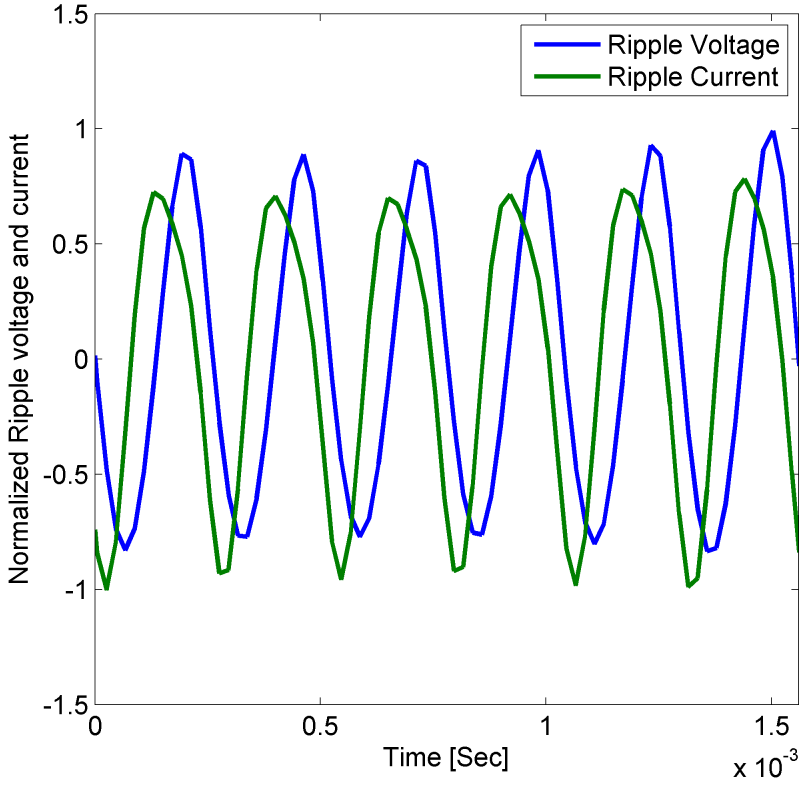

Figure 3.4: Normalized ripple voltage and ripple current at 100 kHz

At high frequencies, the piezoelectric actuator is modeled as a resistor-capacitor combination connected in series instead of a pure capacitive load. To avoid ambiguity with the capacitance measured at low frequencies, the measured capacitance at 100 kHz is called 'effective capacitance' in the remainder of the thesis. The expression for the effective capacitance measurement is as follows:

$$C_e = \frac{I_{r_{rms}}}{2\pi f_r \cdot U_{r_{rms}}}. \tag{3.2}$$

3.5 Impedance Measurement Algorithm

The voltage amplifier/driver uses a boost converter, which amplifies the control voltage by a factor of ten and superimposes a 100 kHz ripple voltage, U_r, onto the driving voltage, U. The superpositioning of the low frequency driving voltage, U (100 Hz) and high frequency ripple voltage, U_r (100 kHz) is shown in Figure 3.5. To apply the proposed measurement technique, it is imperative to extract the high frequency ripple voltages from the low frequency driving voltages since the ripple quantities are employed to measure the impedance. To facilitate this extraction, the current and voltage signals are passed through two identical second order high pass active filters. The circuit diagram of the active filter is shown in Figure 3.6. The capacitance and resistance values for the filter were obtained from a Sullen-key topology implementation [92]. The cut-off frequency of the filters is set to 18000 kHz. Once the ripple quantities are extracted, the next step in the measurement is to decide on the sampling frequency of the measurement.

3.5.1 Selection of the Sampling Frequency

The sampling frequency selection plays an important part in the proposed measurement technique. Shannon's sampling theorem indicates that for a ripple frequency of 100 kHz, one would need to sample at more than 200 kHz in order to ensure that the ripple signal can be reconstructed without frequency folding. Unfortunately, sampling at this high frequency is expensive. However,

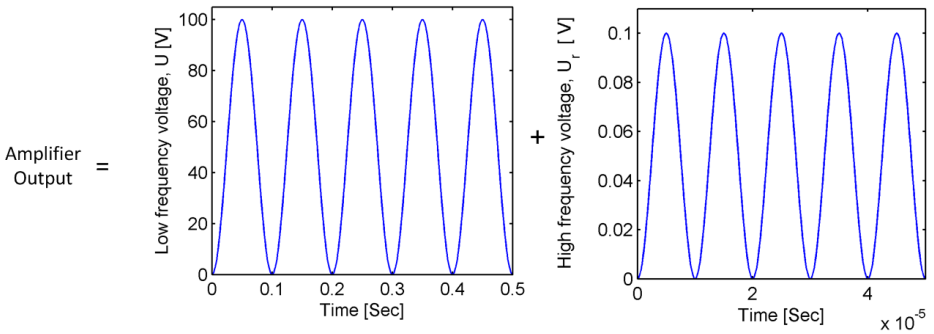

Figure 3.5: Amplifier output while supplying the driving voltage [89] ©2011 IEEE

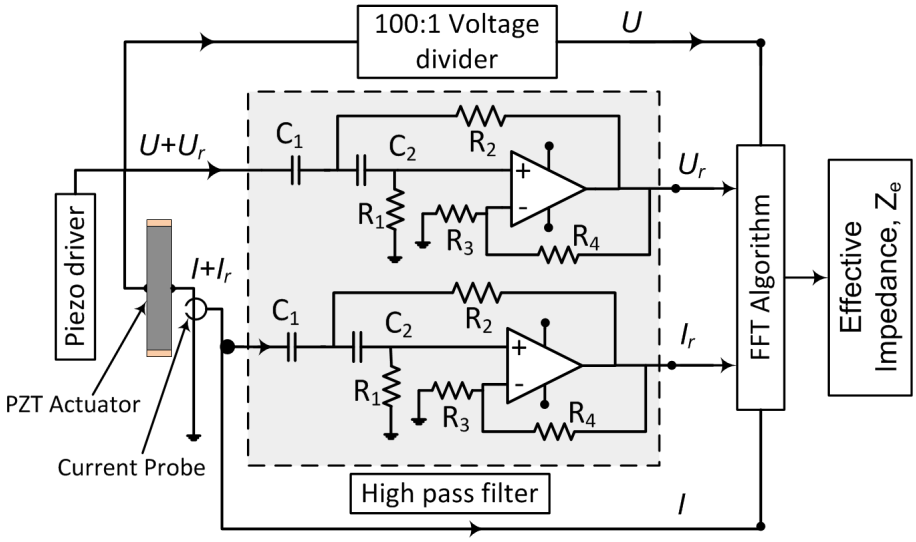

Figure 3.6: Piezoelectric impedance measurement circuit

since the exact frequency of the ripple frequency is known, it is possible to predict where this frequency folds to when lower sampling rates are employed. This feature of the impedance measurement technique is quite novel and has been patented in [91]. To ensure that the sampled signals produce no leakage in the subsequent Fourier transform, the folded ripple frequency, $f_{r_{folded}}$, needs to be an integer multiple of the sampling frequency, f_s:

$$n_s = \frac{f_s}{f_{r_{folded}}} \tag{3.3}$$

Figure 3.7 shows the folding of the ripple frequency, f_r, around the Nyquist frequency, f_N=$\frac{f_s}{2}$, and the zero frequency. From the four cases with folds between zero and three, one can generalize the following relationship between the sampling frequency, f_s, the ripple frequency, f_r, the number of samples per folded ripple period, n_s, and the number of folds n_f:

$$f_s = \frac{2n_s f_r}{n_f n_s + 2}, \quad for n_f = 0,2,4... \tag{3.4}$$

$$f_s = \frac{2n_s f_r}{(n_f + 1)n_s - 2}, \quad for n_f = 1,3,5... \tag{3.5}$$

For a ripple frequency of 100 kHz, there are many possible sampling frequencies for different combinations of number of samples per folded ripple frequency, n_s, and number of frequency folds, n_f. The number of samples per folded ripple frequency, n_s, needs to be chosen such that the subsequent Fourier transform is numerically inexpensive. Both n_s=4, and n_s=12 lead to computationally efficient Fourier transforms. Once n_s has been selected, the number of frequency folds, n_f determines the sampling frequency as well as the folded ripple frequency. One would usually aim to keep the sampling frequency at as low a value as possible while maintaining the folded ripple frequency at a value higher than the mechanical bandwidth of the test-bed.

Table 3.1 shows possible combinations of sampling frequency, f_s, and folded

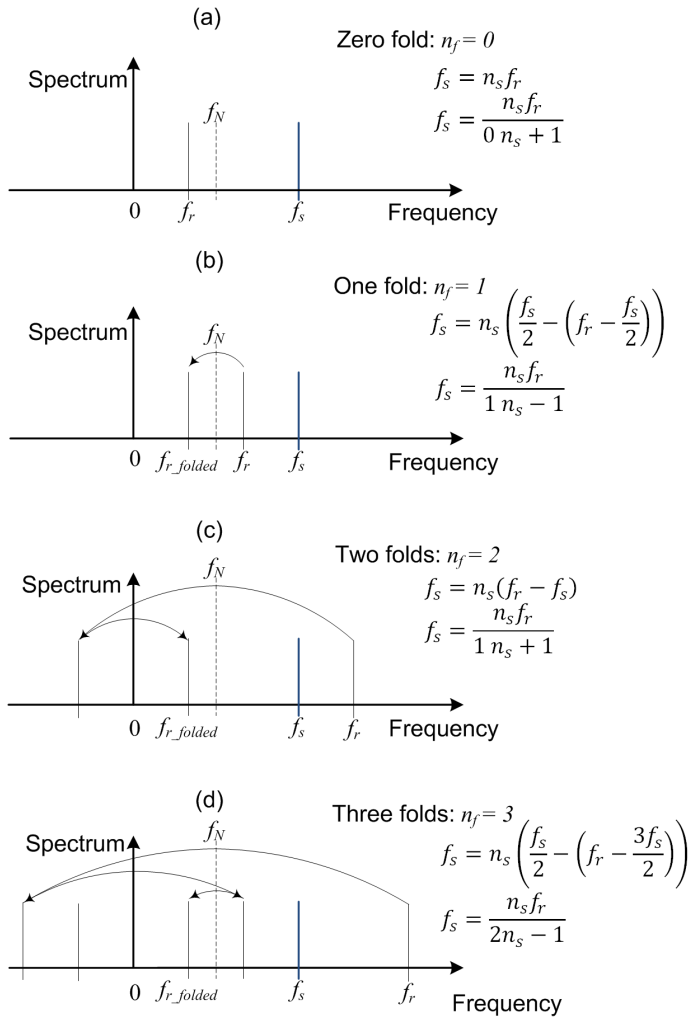

Figure 3.7: Ripple signal with (a) no fold, (b) one fold, (c) two folds, and (d) three folds

ripple frequency, $f_{r_{folded}}$.

Table 3.1: Sampling frequency and folded ripple frequency at different values of n_s with four times folding

n_s	n_f	f_s [kHz]	$f_{r_{folded}}$ [kHz]
4	0	400	100
4	2	80	20
4	12	16	4
12	0	1200	100
12	4	48	4

3.5.2 Real-time Fourier Transformation

A real-time Fourier transformation of the ripple voltage V_r and the ripple current I_r is performed to obtain their magnitudes and phases. The Fourier coefficients of the ripple voltage, A_{V_r} and B_{V_r} as well as of the ripple current, A_{I_r} and B_{I_r} can be obtained using the following discrete transfer functions:

$$\frac{A_{I_r}}{I_r} = \frac{A_{V_r}}{V_r} = \frac{1}{2n_p}\sum_{i=1}^{n_p}\sum_{j=1}^{n_s} sin\left(\frac{2\pi}{n_s}j\right)z^{j-in_s} \tag{3.6}$$

$$\frac{B_{I_r}}{I_r} = \frac{B_{V_r}}{V_r} = \frac{1}{2n_p}\sum_{i=1}^{n_p}\sum_{j=1}^{n_s} cos\left(\frac{2\pi}{n_s}j\right)z^{j-in_s} \tag{3.7}$$

Here, n_p is the number of cycles the Fourier transform is performed across. It should be noted that the division by $2n_p$ does not actually have to be performed, since the impedances of the actuator are determined from ratios of the Fourier coefficients which are independent of n_p. Selection of a larger n_p, has two effects. First, the frequency is filtered around a narrower band. Mathematically this can be stated as follows:

$$f_{PB} = \frac{f_s}{n_s n_p}, \tag{3.8}$$

where, f_{PB} is the passband of the Fourier transform. It should be pointed out that this passband applies to both the folded ripple frequency as well as the original ripple frequency. Too wide a passband can pick up mechanical vibrations close to the folded ripple frequency. Too narrow a passband could miss the ripple frequency, if the ripple frequency is not exactly constant. In addition to the reduction of the passband size, the bandwidth of the capacitance measurement is also reduced when more cycles are employed. Assuming that the Fourier transform provides an average capacitance measurement over the number of cycles used, the bandwidth of the measurement can be approximated as:

$$f_{BW} = \frac{f_s}{n_s n_p \pi}. \tag{3.9}$$

Table 3.2: Passband and bandwidth as a function of sampling periods for a 48 kHz sampling frequency, and $n_s = 12$

Cycles, n_p	Passband, f_{PB} [kHz]	Bandwidth, f_{BW} [kHz]
1	4	1.27
2	2	0.637
4	1	0.318
8	0.5	0.159
12	0.33	0.106
16	0.25	0.08

For the test-bed in this thesis, the ripple voltage frequency is not exactly constant at 100 kHz and so using more than four cycles could lead to a loss of frequency content of the ripple. Also, using more than twelve cycles would result in a capacitance measurement with lower bandwidth than the actuator driving frequency [89].

3.5.3 Parameter Identification from Fourier Series Coefficients

The equivalent RC model for the piezoelectric actuator is presented in Figure 3.8 (a). The phasor diagram is shown in Figure 3.8 (b). By summing up the quantities in real and imaginary directions, the following relationships can be

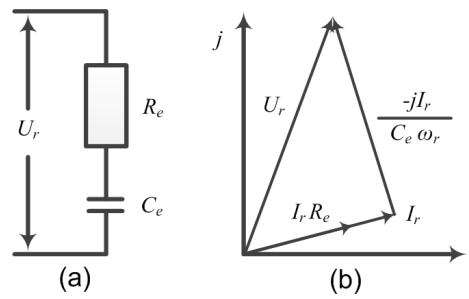

Figure 3.8: (a) Resistance-capacitance model for the piezoelectric actuator (b) phasor diagram

deduced:

$$A_{V_r} = A_{I_r} R_e + \frac{B_{I_r}}{\omega_r C_e} \tag{3.10}$$

$$B_{V_r} = B_{I_r} R_e - \frac{A_{I_r}}{\omega_r C_e} \tag{3.11}$$

Once the Fourier coefficients are obtained, piezoelectric capacitance and resistance can be calculated using Equations 3.12 and 3.13 as follows:

$$C_e = -\frac{1}{\omega_r} \frac{A_{I_r}^2 + B_{I_r}^2}{A_{I_r} B_{V_r} - A_{V_r} B_{I_r}}, \tag{3.12}$$

$$R_e = \frac{A_{I_r} A_{V_r} + B_{V_r} B_{I_r}}{A_{I_r}^2 + B_{I_r}^2}. \tag{3.13}$$

3.6 Results

The measured capacitance and resistance values are observed during a 100 V-10 Hz sinusoidal operation. Plots of driving voltage, actuator displacement, as well as effective capacitance and resistance are shown in Figure 3.9. These mea-

surements help to deduce relationships between different measured quantities such as capacitance-voltage, capacitance-position, and capacitance-resistance relationships. Figure 3.10 shows the relationship between the driving voltage and the effective capacitance. A large hysteresis (~10% of the voltage) is present between the driving voltage and the measured capacitance. Similarly, a large hysteresis is observed between voltage and position in Figure 3.12. However, when effective capacitance is plotted against position in Figure 3.11, minimal hysteresis is observed. The hysteresis between voltage and capacitance and hysteresis between voltage and position cancel each other. In Figure 3.13, the effect of frequency is shown on the capacitance-position relationship. It shows that the capacitance-position relationship slightly changes at relatively large frequency (10 Hz). However, for quasi-static cases, the effect of frequency is small. Two important conclusions can be drawn from these figures: 1) the capacitance which is considered constant in the models (in Section 1.6.2) is not constant during the piezoelectric actuator movement, and 2) the capacitance-position relationship provides a means for position self-sensing at least for low frequency operations due to low hysteresis. These findings lead to two potential contributions in this dissertation: 1) an improved electromechanical model is presented in Chapter 4 which includes the position dependency of the capacitance in the model, and 2) an improved position self-sensing scheme is presented in Chapter 5 which extends the traditional self-sensing schemes applicable in the presence of creep and rate-dependent hysteresis. In Figure 3.14, the effective resistance-capacitance relationship is shown. The resistance values decrease with increased capacitance. The hysteresis present between the resistance and capacitance is 6.25%.

Typically, capacitance is affected by temperature variation which affects the position self-sensing strategy presented in Chapter 5. In Chapter 7, the effect of temperature on capacitance due to self-heat generation and a temperature compensated position self-sensing are presented.

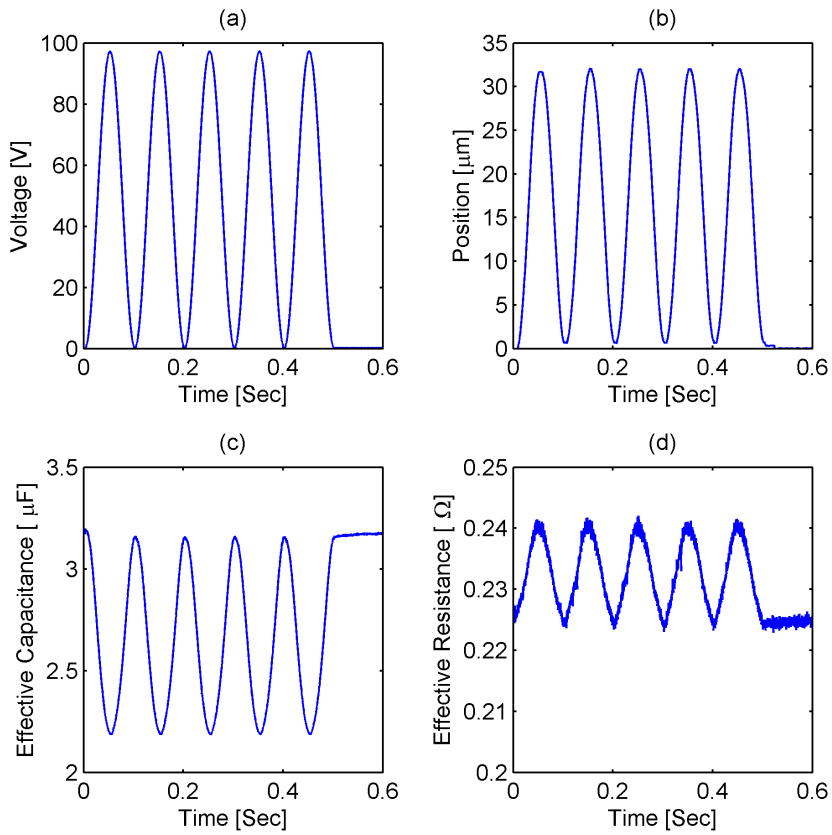

Figure 3.9: (a) Voltage, (b) position, (c) effective capacitance, and (d) effective resistance at 10 Hz

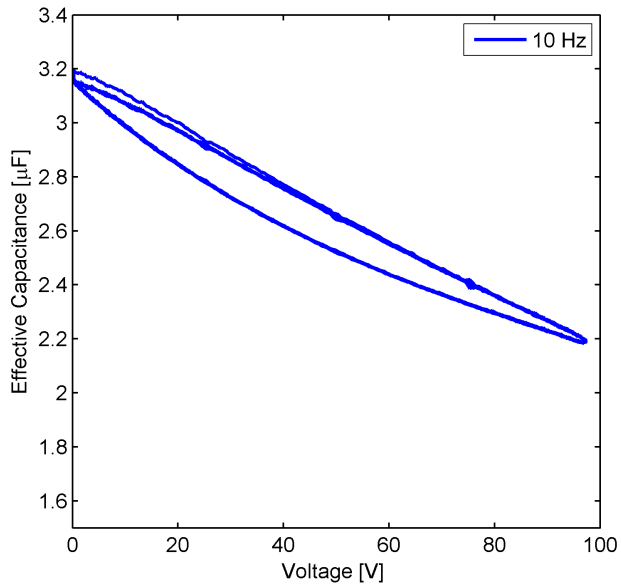

Figure 3.10: Hysteresis in effective capacitance-voltage relationship

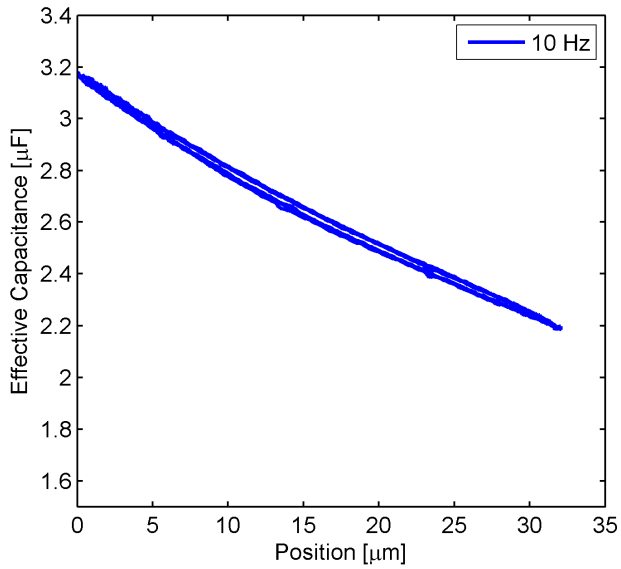

Figure 3.11: Effective capacitance measurement with position

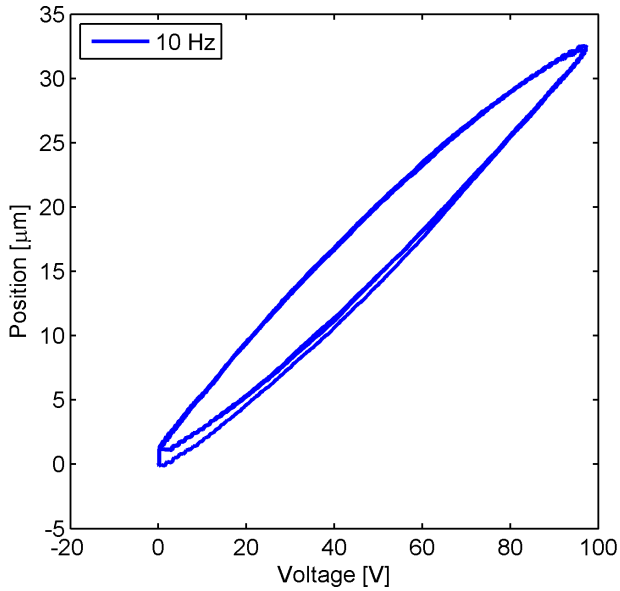

Figure 3.12: Hysteresis in effective position-voltage relationship

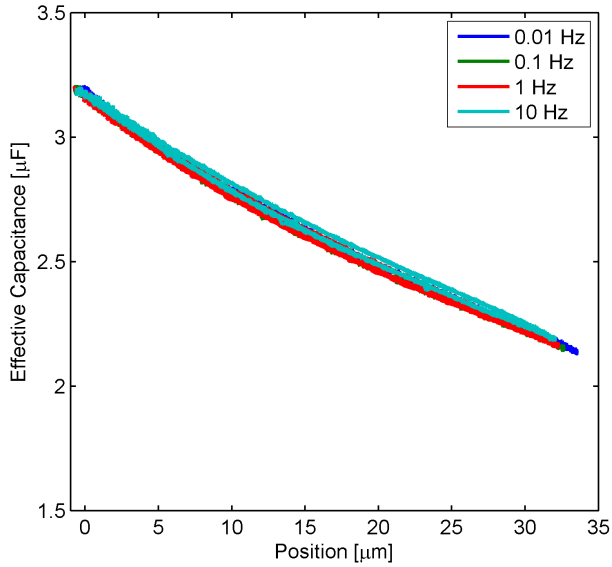

Figure 3.13: Effective capacitance measurement with position at various frequencies

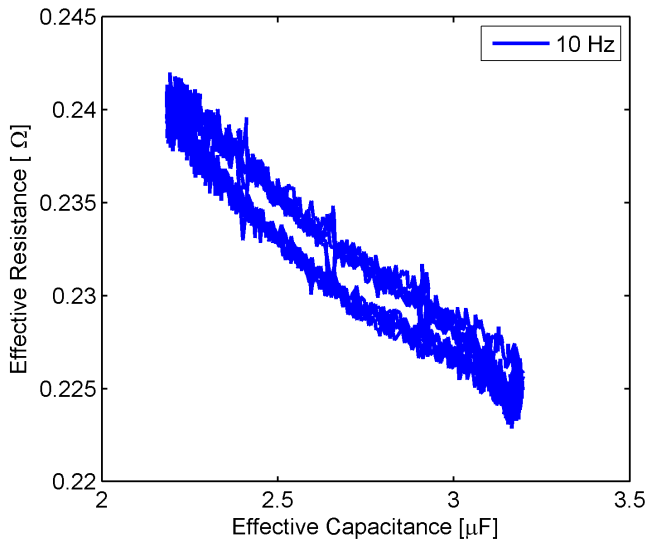

Figure 3.14: Effective resistance measurement with effective capacitance

3.7 Summary

A novel real-time impedance measurement technique is presented in Chapter 3. To obtain a real-time measurement of the piezoelectric clamped capacitance for an accurate model of the piezoelectric actuator, high frequency ripple voltage and ripple current are employed. The high frequency ripple signals are superimposed on the driving signal and hence provide real-time measurement of the impedance. Since the ripple frequency is significantly higher than the first natural frequency of the test bed, no movement is induced by the ripple. Thus the ripple signals can be used to determine clamped impedance. The impedance of the piezoelectric actuator is modeled as an equivalent resistance-capacitance element connected in series. The impedance values are obtained using Fourier series transformations of the ripple voltage and ripple current. This real-time impedance measurement shows that the capacitance variation is related to position change in piezoelectric actuator without significant hysteresis. Based on this finding, an extended electromechanical model is proposed in Chapter 4. In addition, a position self-sensing scheme is developed in Chapter

5 based on the capacitance-position relationship.

Chapter 4

An Improved Electromechanical Model for Piezoelectric Actuators

Piezoelectric actuator models can be classified into two broad groups: 1) physical models, and 2) phenomenological models. The physical models are based on measurable quantities such as voltage, charge, force, displacement or the equivalent quantities such as electric field, current, stress and strain. Usually, the physical models are the augmented version of the linear IEEE model discussed in Section 1.6.1. The eminent Goldfarb and Celanovic model [13] includes the dynamics and hysteresis phenomenon in piezoelectric actuators which are missing in the IEEE model. The dynamics are included using a second order lumped mass system. The hysteresis is modeled using generalized Maxwell's resistive-capacitive operator. The model is presented earlier in Section 1.6.2. Phenomenological models rely upon the input-output relationship (voltage and position) of the piezoelectric actuator. Hence,these models do not require knowledge of the underlying physical interaction between the variables to implement the model which makes these models very popular. However, highly accurate phenomenological models are required to implement the feedforward control. Due to the limitations in the phenomenological models, electromechanical models are used in this study.

In the physical model presented by Goldfarb and Celanovic [13], the piezoelectric actuators are modeled as capacitors in the electric domain. A hysteresis block is added in series with the capacitor model of the actuator (Figure 1.10). In this model, the piezoelectric capacitance (similar to dielectric permittivity in the IEEE model in Section 1.6.1) and force-voltage proportionality constant(similar to piezoelectric strain coefficient in the IEEE model) are assumed

constant. These parameters are identified from the measurements of stiffness and DC gain between charge and displacement [13]. A frequency analyzer program is used to identify the piezoelectric capacitance. The other model parameters such as force-voltage proportionality constant and stiffness are identified experimentally from force vs voltage and force vs displacement relationships respectively. Badel et al. [41] employ a hyperbolic function to model the hysteresis in the Goldfarb model and identify the function coefficients for ascending and descending hysteresis paths. Also, the force-voltage proportionality constant is identified using one of the function parameters in relation to force and voltage. Finally, free capacitance is measured and clamped capacitance is obtained from the free capacitance using constitutive equations. Juhasz et al. [93] propose a parameter identification process for an embedded piezoelectric micropositioning system. In this study, the force-voltage proportionality constant is measured when the hysteresis slope between the applied voltage and the position is constant. Quant et al. [94] also use a similar model as proposed by Goldfarb et al. [13] for a piezoelectric bending actuator. However, in an attempt to provide a better model fit, the force-voltage proportionality constant is considered a 6th order polynomial function of voltage derived from a piezoelectric strain coefficient measurement. The models introduced above are extension of the traditional model proposed by Goldfarb and Celanovic [13]. In most of the cases, the model parameters, such as the capacitance, stiffness and force-voltage proportionality constant are assumed constant. However, all the stated models differ in the parameter identification technique.

Table 4.1 shows how close the identification techniques of different research groups come to the manufacturer specifications. Every model has at least one parameter that is significantly different from the suggested values by the manufacturer. Since the manufacturer measurements are based on the linear IEEE constitutive equations, which do not include hysteresis, the variation between the manufacturer stipulated data and parameters from the different models is expected. However, these parameters should not be orders of magnitude different.

This chapter presents an improved electromechanical model of the piezoelectric actuator which relies upon the real-time capacitance measurement pre-

sented in Chapter 3. A new model is developed based on the position dependent capacitance. This leads to an improved fit between charge and position when compared to the traditional electromechanical model. Thus, the new model can be used to improve the accuracy of charge based sensorless position control. Another advantage of the new model is that the model parameters can be identified from a single set of current, voltage, position and capacitance measurements. Finally, other material parameters such as piezoelectric strain coefficient, d_{33}, piezoelectric coupling coefficient, k_{33}, and the permittivity constant, ϵ_{33} can be deduced by employing the constitutive relationships.

Table 4.1: Comparison of parameters from different piezoelectric models with manufacturer data [95]

		α comparison		C_P comparison		k_P comparison	
Model	Manufacturer - Model number	$\alpha_{ident.}$ $[NV^{-1}]$	$\alpha_{manuf.}$[7] $[NV^{-1}]$	$C_{Pident.}$ $[\mu F]$	$C_{Pmanuf.}$ $[\mu F]$	$k_{Pident.}$ $[N\mu m^{-1}]$	$k_{Pmanuf.}$ $[N\mu m^{-1}]$
Goldfarb et al.	NEC - AE0505D16	10.00	9.31	1.20	1.40	6.00	48.85
Badel et al.	NEC - AE0505D44H40F	7.19	9.31	2.77	3.40	28.70	20.24
Juhasz et al.	PI - P885-50	17.55	8.05	1.50[8]	1.50	100.29	50.00

[7] Obtained from $\alpha = \frac{d_{33}A}{s_{33}t_P}$ where, s_{33} is the mechanical compliance, A is the stack cross sectional area, and t_P is the layer thickness

[8] Manufacturer specified value[18]

4.1 Proposed Piezoelectric Model

In order to better describe the behavior of the experimental test-bed and the piezo stack used within that test-bed, both the constitutive Equations 1.4 and 1.5 in the model presented by Goldfarb and Celanovic describing the mechanical and the electrical domain require modification. The modification proposed in the new model are outlined in the following sections.

4.1.1 Mechanical Subsystem

The mechanical domain of the test setup is described by the force Equation 1.4. The test setup is shown in Figure 2.3. A schematic diagram of the mechanical system is shown in Figure 4.1. The moving mass term includes the mass of the needle assembly, m_n and the mass of the piezo actuator, m_P. Since the piezoelectric actuator behaves like a heavy spring, only one third of the piezo mass is also considered [96]. Traces from the force sensor indicate that the friction between needle and the Teflon sleeve is negligible 4.2. Finally, the stiffness is comprised of the preload spring stiffness, k_s and the piezo stiffness, k_P. The updated force equation describing this model is given in Equations 4.1 and 4.2:

$$\alpha U_P = m\ddot{x} + b\dot{x} + kx, \tag{4.1}$$

$$\alpha U_P = \left(m_n + \frac{m_P}{3}\right)\ddot{x} + b\dot{x} + (k_P + k_s)x. \tag{4.2}$$

4.1.2 Electrical Subsystem

Goldfarb and Celanovic [13] model the piezoelectric actuators as capacitors in the electrical domain. Change in piezoelectric capacitance with voltage is observed in [97, 98], which is not reflected in Equation 1.5. This change of capacitance with position is confirmed by the online effective capacitance measurement presented in Chapter 3. Traditional capacitance measurements employ a relatively low frequency and high voltage (1 kHz, 1 V_{PP}) in comparison to the

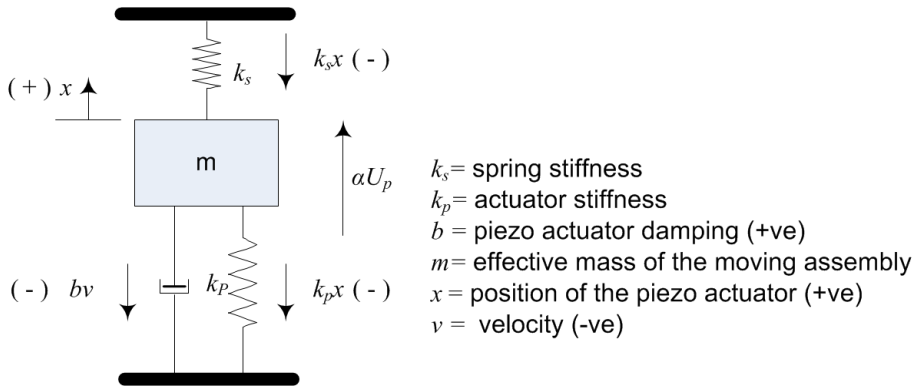

Figure 4.1: Schematic representation of the test setup

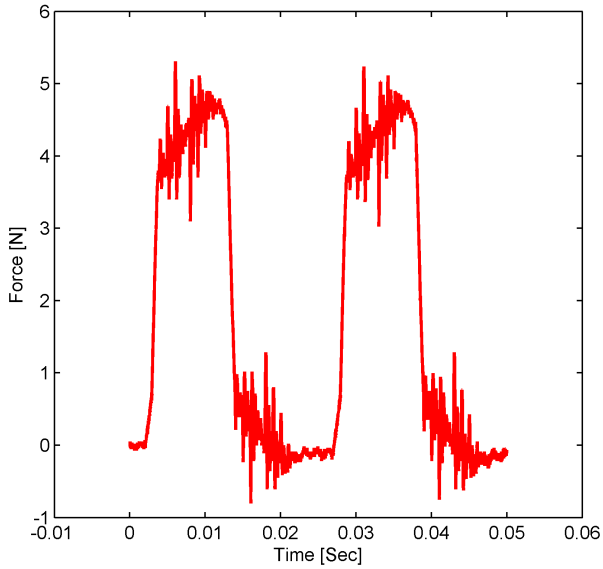

Figure 4.2: Force measurement at 50 Hz

proposed effective capacitance measurement ripple voltage (U_r = 100 kHz, 0.1 V_{PP}). Since the frequency of the proposed measurement is much higher than the first natural mechanical frequency (2500 Hz) of the test setup, the ripple voltage does not induce any movement during measurement. Thus, the proposed effective capacitance measurement provides a clamped capacitance measurement. In addition, the measurement has little hysteresis, since the driving voltages are very low [90]. Figure 4.3, shows the relationship between measured effective capacitance and position for driving frequencies between 10 Hz and 100 Hz.

At low driving frequencies, the inertial and friction terms presented in the constitutive Equation 1.4 can be neglected in comparison to the stiffness term [14, 28]. Hence, the mechanical constitutive equation reduces to:

$$\alpha U_P = kx. \tag{4.3}$$

To include the variable capacitance as seen in Figure 4.3, the clamped capacitance, C_P is described as a linear function of the piezo voltage, U_P, and subsequently is a function of position, x, since U_P and x are linearly related from Equation 4.3 for low driving frequencies:

$$C_P = C_{P0} + \Delta C_U U_P = C_{P0} + \Delta C_x x, \tag{4.4}$$

$$\Delta C_U = \Delta C_x \frac{\alpha}{k}, \tag{4.5}$$

where, C_{P0} is the capacitance value at zero voltage and ΔC_U is the change in capacitance as a function of U_p while ΔC_x is the change in capacitance with position. Adding the linear capacitance-position relationship (in Equation 4.4) to the charge equation presented in Equation 1.5, the following relationship is obtained:

$$q = C_P U_P + \frac{\Delta C_U}{2} U_P^2 + \alpha x. \tag{4.6}$$

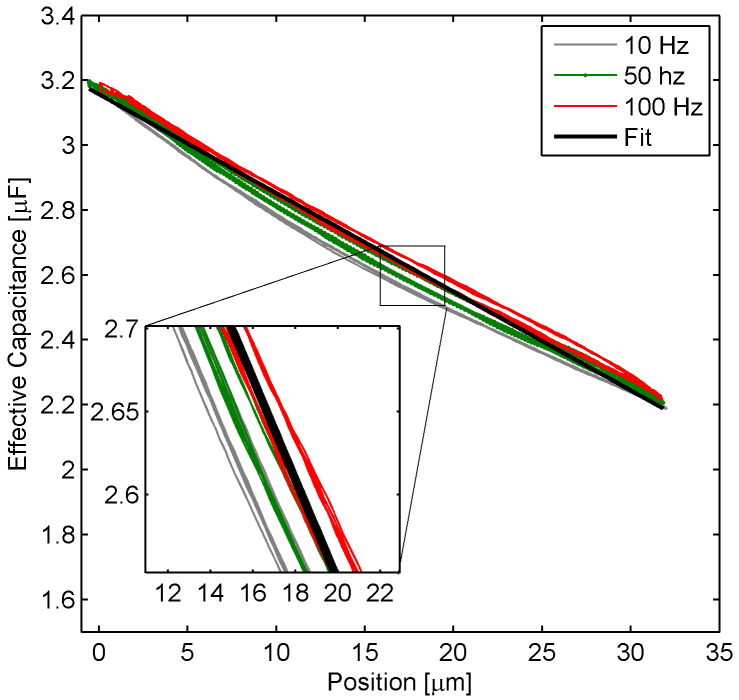

Figure 4.3: Capacitance-position relationship at various frequencies

4.2 Power Balance

In the previous section, an additional term is introduced into the constitutive equation for the electrical domain (Equation 4.6) and no adjustment is made to the mechanical domain (Equation 4.1). This section uses a power balance to show that these equations are still consistent with each other. Ignoring the hysteresis, the total power delivered to the stack is equal to the product of applied current, I, and piezo voltage, U_P. The portion of the power that is not lost to friction is stored in the stack as spring, kinetic, and capacitive energy:

$$U_P I = P_{friction} + \frac{d}{dt}E_{spring} + \frac{d}{dt}E_{kinetic} + \frac{d}{dt}E_{capacitor}. \tag{4.7}$$

For a nonlinear capacitor the energy stored can be calculated as follows [99]:

$$E_{capacitor} = U q_{cap} - \int q_{cap} dU = \frac{1}{2}C_{P0}U^2 + \frac{1}{3}\Delta C_U U^3. \tag{4.8}$$

Substituting Equation 4.8 into Equation 4.7 and replacing U with U_P yields a simple expression for the power balance:

$$\begin{aligned} U_P I = &\frac{d}{dt}\int b\dot{x}dx + \frac{d}{dt}\left(\frac{1}{2}kx^2\right) + \frac{d}{dt}\left(\frac{1}{2}m\dot{x}^2\right) \\ &+ \frac{d}{dt}\left(\frac{1}{2}C_{P0}U_P^2 + \frac{1}{3}\Delta C_U U_P^3\right), \end{aligned} \tag{4.9}$$

$$U_P I = b\dot{x}^2 + kx\dot{x} + m\dot{x}\ddot{x} + C_{P0}U_P\dot{U}_P + \Delta C_U U_P^2 \dot{U}_P. \tag{4.10}$$

It is now demonstrated that the constitutive Equations 4.1 and 4.6 provide the same expression for power balance. First, Equation 4.1 is divided by α in order to obtain an expression for the piezo voltage U_P:

$$U_P = \frac{m\ddot{x} + b\dot{x} + kx}{\alpha}. \tag{4.11}$$

Then, a time derivative is taken of Equation 4.6 in order obtain the current supplied to the stack, I:

$$I = \alpha\dot{x} + C_{P0}\dot{U}_P + \Delta C_U U_P \dot{U}_P. \tag{4.12}$$

Finally, Equations 4.11 and 4.12 are multiplied to obtain the same expression as the original power balance shown in Equation 4.10:

$$U_P I = b\dot{x}^2 + kx\dot{x} + m\dot{x}\ddot{x} + \frac{m\ddot{x} + b\dot{x} + kx}{\alpha}(C_{P0}\dot{U}_P + \Delta C_U U_P \dot{U}_P), \tag{4.13}$$

$$U_P I = b\dot{x}^2 + kx\dot{x} + m\dot{x}\ddot{x} + C_{P0}U_P\dot{U}_P + \Delta C_U U_P^2 \dot{U}_P. \tag{4.14}$$

Since Equations 4.10 and 4.14 are identical, it is concluded that the mechanical constitutive equation is unaffected by the introduction of the nonlinear capacitance in the electrical constitutive equation.

4.3 Parameter Identification

Traditional models have usually assumed that C_P, α, k, and b are time invariant. The proposed model suggests a position dependent capacitance. In order to show the improvements attainable with this approach, a separate identification procedures for the base case with a constant capacitance and the new variable capacitance model are defined in Sections 4.3.1 and 4.3.2. Thereafter, additional material parameters are derived in Sections 4.3.4, 4.3.4.1 and 4.3.4.2.

4.3.1 Identification of α, k, b, and m for the Traditional Model with Constant Capacitance

When Equations 1.4 and 1.5 are combined for quasi static conditions, an expression linking charge linearly to displacement is obtained:

$$q = \left(C_P \frac{k}{\alpha} + \alpha\right) x. \tag{4.15}$$

The relationship between charge and position only allows the identification of one of the three parameters α, k, or C_P. Two of these parameters need to be identified by other relationships. The clamped capacitance can be measured using the technique described in Chapter 3.

The stiffness is obtained by dividing the force, F_{ext} developed at maximum

voltage and zero stroke by the displacement achieved at maximum voltage and no externally applied force. This measurement technique is only an approximation, since it assumes that the hysteresis voltage, U_H, is the same for clamped and free conditions.

$$k = \frac{F_{ext}|_{U_{max}=0,x=0}}{x|_{U_{max}=0,F=0}} \tag{4.16}$$

Given C_P and k, one can then use Equation 4.15 to identify the force-voltage proportionality constant, α from a quasi-static charge vs displacement experiment. In order to obtain values for the damping coefficient b, and mass m, one can perform dynamic experiments. In this case, a minimization of the error between measured charge, $\bar{q}$ and charge calculated from position, velocity and acceleration (using the model) is solved:

$$err_{lin} = \bar{q} - \frac{C_P}{\alpha}(m\ddot{x} + b\dot{x} + kx) - \alpha x. \tag{4.17}$$

This minimization procedure can be performed with a simple quadratic error minimization algorithm, or a nonlinear search algorithm. In this research, a MATLAB function 'fminsearch' is used which is based on the the Nelder-Mead optimization function in [100]. Both approaches provide similar answers. In theory, Equation 4.17 can be used to identify b, and m with the given values of α, C_P, and k. However, the experiments are performed well below the first mechanical eigenfrequency of the stack assembly, and so the sensitivity for determining the moving mass m, is poor. Instead, the mass m, is determined by adding a third of the stack mass m_P, to the needle mass m_n.

4.3.2 Identification of α, k, b, and m for the Proposed Model with Variable Capacitance

The constitutive Equations 4.1 and 4.6 are characterized by the clamped capacitance, C_P, the mass, m, the force-voltage proportionality constant, α, the stiffness, k and the damping, b. Given measurements of capacitance as a function of position, both stiffness k, and force-voltage proportionality constant, α can be obtained directly from the quasi static relationship between charge and

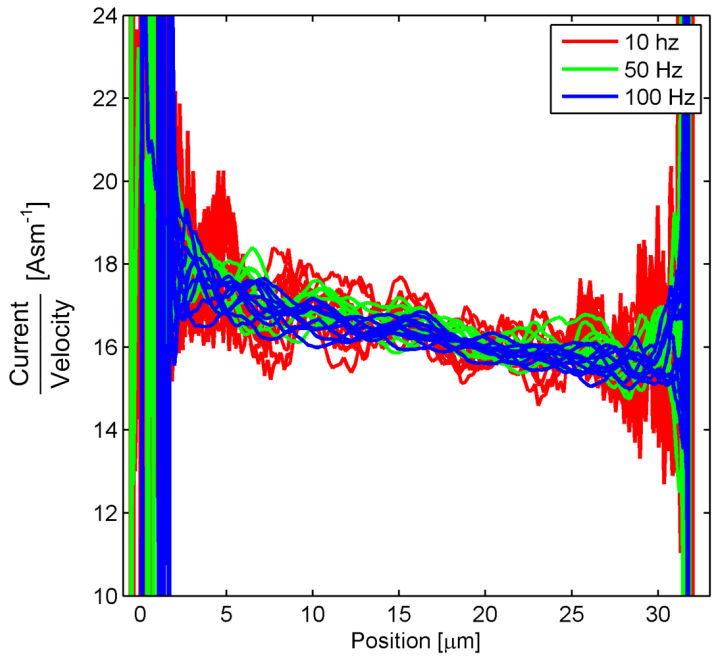

Figure 4.4: Capacitance-position relationship at various frequencies

position, since this is now a second order polynomial:

$$q = C_{P0}\frac{k}{\alpha}x + \frac{\Delta C_x}{2}\frac{k}{\alpha}x^2 + \alpha x. \tag{4.18}$$

An alternative way to determine k and α using quasi static experiments is to fit current over velocity. This avoids integrating current in order to obtain charge [101]:

$$\frac{\dot{q}}{\dot{x}} = \left(\frac{C_{P0}k}{\alpha} + \alpha\right) + \Delta C_x \frac{k}{\alpha}x. \tag{4.19}$$

It is shown in Equation 4.19 that the ratio of current over velocity is not a constant as would be the case for the original model by Goldfarb and Celanovic (compare Equation 4.15). This is confirmed by the measurements shown in Figure 4.4 where driving voltages of different frequencies are applied to the actua-

tor. It should be pointed out that Equation 4.19 leads to a division by zero close to the beginning and the end of the stroke (where velocities are zero). Thus, measurements are only physically meaningful towards the center of the stroke.

The mass of the actuator system is estimated by adding a third of the stack mass m_P, to the needle mass m_n. To obtain the damping coefficient b, dynamic experiments need to be performed. In this case, b, is found by using the Nelder-Mead optimization algorithm (1965) to minimize the error between measured charge, $\bar{q}$ and charge calculated from measured position, velocity, and acceleration:

$$err_{nonlinear} = \left(\bar{q} - C_{P0}U_P - \frac{\Delta C_x}{2}\frac{\alpha}{k}U_P^2 - \alpha x\right), \tag{4.20}$$

where,

$$U_P = \frac{m\ddot{x} + b\dot{x} + kx}{\alpha}. \tag{4.21}$$

4.3.3 Identification of Free Capacitance, C_T

Free capacitance is measured under stress free condition that are present when there is no or constant external load. The relationship between the clamped and free capacitance can be deduced from the constitutive charge Equation 4.6 as follows:

$$\frac{q_P}{U_P} = C_P + \frac{\alpha^2}{k} = C_T. \tag{4.22}$$

where, C_T is the free capacitance. From the free capacitance, the free permittivity can be obtained through Equation 4.23 where, ϵ_T is the free permittivity, A is the area of the electrode (~ to cross sectional area of actuator), n_l is the number for layers in the actuator and ϵ_0 is the permittivity constant at vacuum:

$$\epsilon_T = \frac{C_T A}{\epsilon_0 t_P n_l}. \tag{4.23}$$

4.3.4 Identification of Material Properties

The piezoelectric material properties such as piezoelectric strain coefficient, d_{33} and piezoelectric coupling coefficient, k_{33} can also be obtained from the constitutive relationships once the model parameters are obtained. In this section, the material parameters are attained from the identified model parameters and compared with the manufacturer specification where available.

4.3.4.1 Piezoelectric Strain or Charge Coefficient, d_{33}

The piezoelectric strain or charge coefficient, d_{33} is an important design parameter for piezoelectric actuator systems. It is defined as the strain developed per unit of applied electric field in the piezoelectric materials. Alternatively, this is equivalent to the polarization generated due to the applied stress. The first subscript 3 represents the direction of the strain or polarization while the second subscript represents direction of the applied electric field or stress. Traditionally, it is measured using the linear IEEE constitutive Equation 1.2 which assumes the applied stress is negligible and strain is a function of applied electric field. Measuring both strain and electric field provides the d_{33} measurement. However, the traditional measurement employs the applied voltage instead of the linearized voltage, U_P, as a measure of electric field. As a result, different d_{33} are obtained at different voltage levels due to hysteresis. To minimize this hysteresis effect, traditional measurements are often performed at the maximum level of the applied voltage, U. Also, since d_{33} provides an estimate of the quality of the materials, large signal values provide more practical representation. The term d_{33} is an equivalent term to the force-voltage proportionality constant, α in the electromechanical model. The following equation [102] presents the relationship between d_{33} and α:

$$d_{33} = \frac{\alpha}{n_l k} = \frac{\alpha t_P}{L_P k}, \tag{4.24}$$

where, n_l is the number of layers in the actuator and k is the stiffness of the actuator. The number of layers is calculated from the thickness of the piezoelectric layers, t_P and the length of the actuator, L_P.

4.3.4.2 Piezoelectric Coupling Coefficient, k_{33}

The piezoelectric coupling coefficient, k_{33} is an important parameter which represents the fraction of electromechanical energy conversion in the piezoelectric system. It is an indication of the effectiveness or efficiency with which the piezoelectric actuator converts electrical to mechanical energy or vice versa. The first subscript 3 represents the direction of the applied electric field while the second subscript represents the direction of the mechanical movement. A higher value of the coefficient is desired. It does not include the dielectric or mechanical losses. The coupling coefficient can be obtained from the following relationship [102] of clamped and free capacitance:

$$k_{33}^2 = 1 - \frac{C_P}{C_T}. \tag{4.25}$$

From the identified values of C_P and C_T, the piezoelectric coupling coefficient can be obtained.

4.4 Experimental Results

The model parameters are identified through experiments using the setup discussed in Section 2.2 and the identification algorithms outlined in Section 4.3.

4.4.1 Experimental Procedure

The model identification experiments use a sinusoidal voltage profile with frequencies between 10 Hz, 100Hz and a magnitude of 100V. The actuators are allowed sufficient time to reach a state where little hysteresis voltage is present before starting the experiments. The position measurement is zeroed at the beginning of the measurement and data are recorded for 5 cycles shown in Figure 4.5. At every frequency, 5 sets of data are recorded in order to ensure the statistical significance. The model parameters are obtained using the methods described in Section 4.3 and listed in Table 4.2 together with the manufacturer specifications. Two cases are presented in the table, where Case 1 presents the

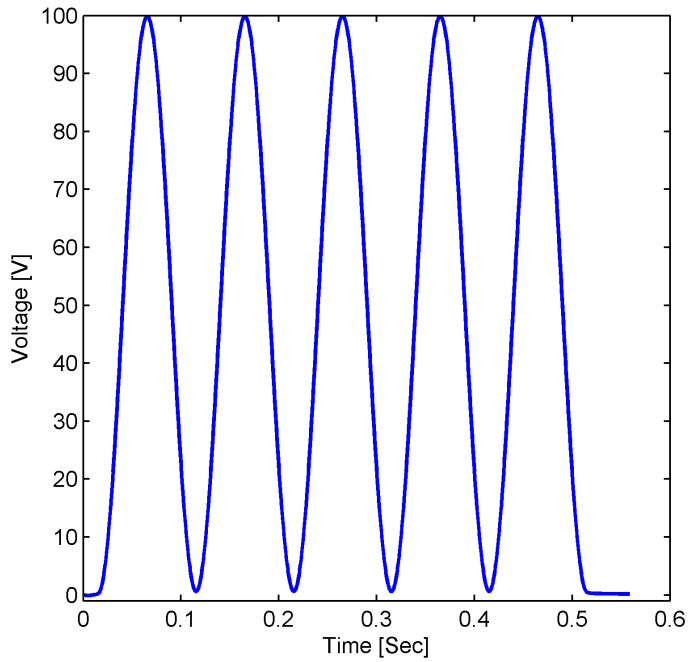

Figure 4.5: Driving signal, U at 10 Hz

traditional model with a constant capacitance while Case 2 depicts the improved model with variable capacitance.

In Case 1, the value of capacitance is considered constant in the traditional model. The value of the capacitance at zero V matches with the value prescribed by the manufacturer in Case 2, the new proposed model. However, in the manufacturer specification, it is prescribed that there is 20% variability present in the capacitance measurement. The slope in the capacitance measurement is not specified by the manufacturer, but similar trends have been reported by [97, 98] when a DC voltage is applied to piezoelectric components. The identified stiffness values are largely different in Case 1 and Case 2. In Case 1, it is measured from static loading test using Equation 4.16 while in Case 2, it is obtained from the dynamic measurement of charge and position using Equation 4.19. This identification is very close to the manufacturer specification. Also, the other parameters such as α, d_{33} and k_{33} values are close to the values stipulated

Table 4.2: Model parameter identification

Model parameters	Unit	Case 1 (Traditional Model, $\Delta C_x = 0$)	Std. dev.[9]	Case 2 (Proposed Model, $\Delta C_x \neq 0$)	Std. dev.[10]	Manufacturer's Specification
Capacitance at 0V, C_{P0}	$[\mu F]$	3.13[11]	0.03	3.13[10]	0.03	3.1[12]
Capacitance at 100V, C_{P100}	$[\mu F]$	3.13[10]	0.03	2.16[10]	0.01	-
Capacitance slope, ΔC_x	$[Fm^{-1}]$	0	–	-0.03	6e-4	-
Actuator Stiffness, k_P	$[N\mu m^{-1}]$	11.2	0	25.3	0.16	25
Actuator damping, b	$[Nsm^{-1}]$	3100	377	2120	120	-
Force-voltage prop. constant, α	$[NV^{-1}]$	14.05	0.03	9.34	0.27	9.01[13]
Piezoelectric strain coeff., d_{33}	$[pmV^{-1}]$	2400	30	695	20	680[14]
Piezoelectric coupl. coeff., k_{33}		0.92	0	0.72	0.01	0.70[14]

[9] Calculated over three sets of experiments
[10] Calculated over three sets of experiments
[11] Identified capacitance values are measured at 100 kHz and 0.1 V
[12] Manufacturer's specified values are measured at 1 kHz and 1 V_{PP} [18]
[13] Obtained from $\alpha = \frac{d_{33} A}{s_{33} t_P}$ [102]
[14] Manufacturer data sheet [103]

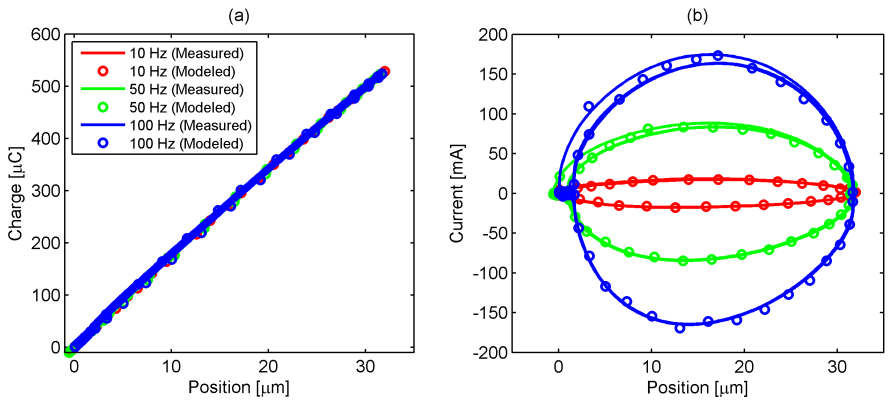

Figure 4.6: (a) Charge-position relationships modeled (proposed) and measured, and (b) current-position relationships modeled and measured for various frequencies

from manufacturer's specification with the proposed model. It is important to note that the identified parameters are sensitive to the capacitance measurement which includes both the C_{P0} and ΔC_x. The sensitivity of the identified parameters to changes in the capacitance measurement is shown in Table 4.3. To identify the parameters, the parameters presented in 4.2 for Case 2 are used considering the capacitance measurement is unaffected.

4.4.2 Model Validation Through Charge-position Relationship

For model validation, measured values of charge-position relationships are compared with the modeled charge-position relationship in Figure 4.6(a) using Equation 4.18. The nearly linear relationship between charge and position is largely independent of driving frequency, since friction forces and inertial forces are small at the tested frequencies. A more detailed comparison for the quality of fit is obtained by plotting current against position as shown in in Figure 4.6(b). Since current is closely related to velocity, one expects to see ellipses that open up with increasing frequency. In Figure 4.7(a) and 4.7(b), the charge-position relationship is compared between the traditional model ($\Delta C_x = 0$) and the proposed model ($\Delta C_x < 0$). The modeling errors, presented in Figure

Table 4.3: Sensitivity of parameter identification to changes in capacitance measurement

Parameters	No change	20% increase in C_{P0}	20% increase in ΔC_x	20% increase in C_{P0} and ΔC_x
k $[N\mu m^{-1}]$	25.1	20.7	24.0	20.9
α $[NV^{-1}]$	9.36	7.72	10.77	9.36
d_{33} $[pmV^{-1}]$	700	697	841	840
k_{33}	0.72	0.66	0.77	0.73
U_{Pmax} [V]	86	86	72	72

4.7(c) and 4.7(d), are calculated using Equation 4.17 for the traditional model and using Equation 4.20 for the proposed model. Figure 4.7 indicates that the proposed model shows slight improvements in terms of fitting the measured charge-position relationship. Both the 10 Hz and the 100 Hz cases show identical trends where the proposed model provides lower fitting errors especially towards the center of the stroke. This is because of the ability of the proposed model to capture the curvature in the charge-displacement relationship with the additional term in the charge constitutive equation.

4.4.3 Hysteresis Voltage

The driving piezoelectric voltage, U is composed of the linear piezoelectric voltage, U_P and the hysteresis voltage, U_H. Once the model parameters are identified, one can obtain U_P using Equation (4.14).The hysteresis voltage, U_H is obtained through the traditional model in Equation 1.6. Figure 4.8(a) shows the driving voltage, piezoelectric voltage and the hysteresis voltage obtained for the traditional model with different frequency ranges. Figure 4.8(b) presents the same voltages for the proposed model. In both cases, the hysteresis voltage and the linear piezoelectric voltage show similar trends for all tested frequencies. However, the hysteresis voltage obtained through the traditional model is significantly large than for the proposed model. To be physically meaningful, hysteresis voltages should be in the order of approximately 20% of the applied voltage. This is the case for the parameters of the proposed model, but not for the traditional model parameters.

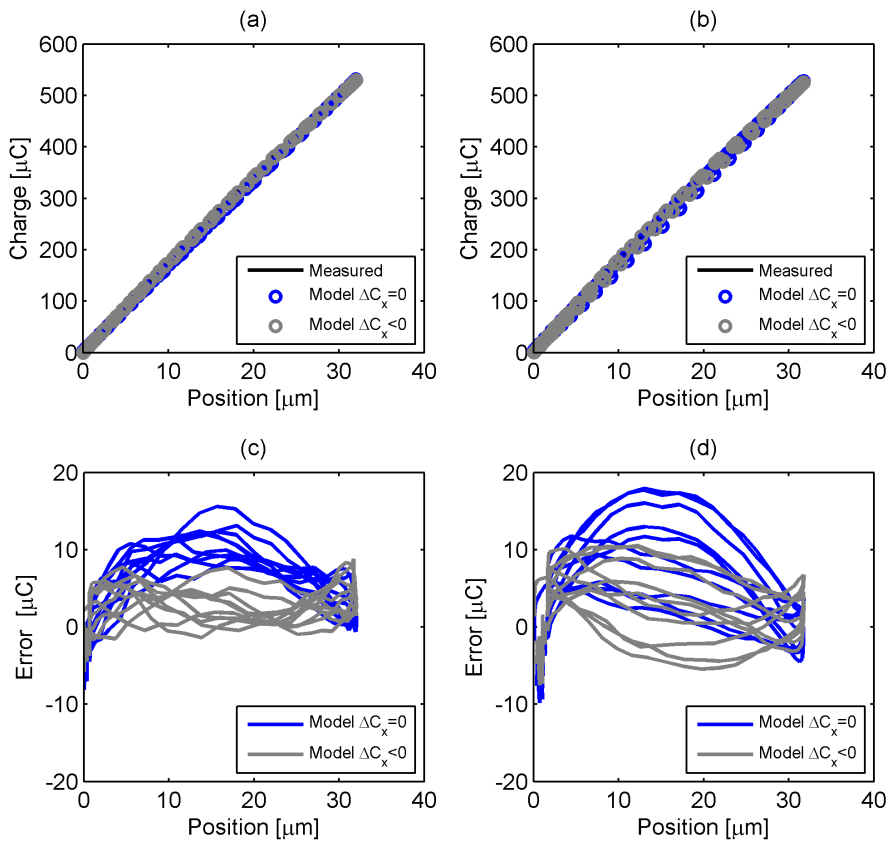

Figure 4.7: Comparison of charge-position relationship: measured, traditional model ($\Delta C_x = 0$) and proposed model ($\Delta C_x < 0$) at (a) 10 Hz, (b) 100 Hz, errors at (c) 10 Hz, and (d) 100 Hz

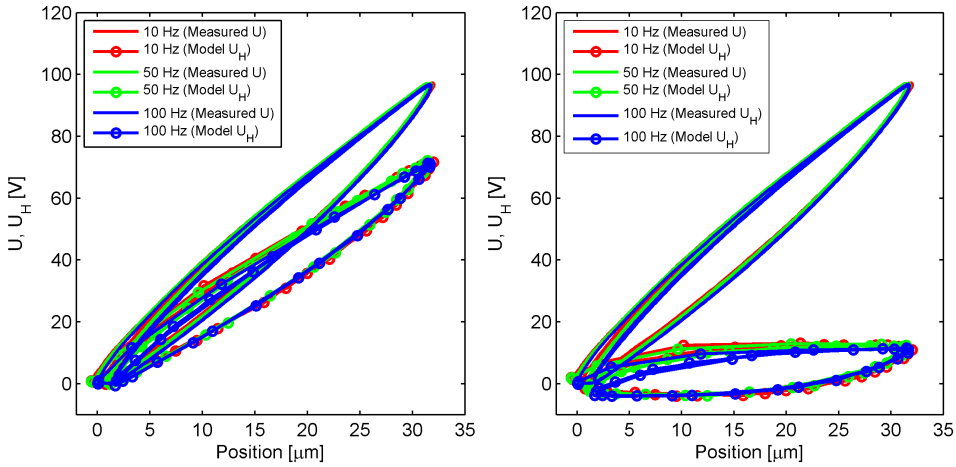

Figure 4.8: (a) U and U_H vs charge for $\Delta C_x = 0$ (traditional model), and (b) U and U_H vs charge for $\Delta C_x < 0$ (proposed model) at 10 Hz and 100 Hz

4.5 Summary

In this chapter, an improved piezoelectric model is proposed by introducing a nonlinear capacitance term. This new term provides a better fit of the relationship between charge and position. A second advantage of this model is that actuator stiffness and force-voltage proportionality constant can be identified from quasi static measurements of position, charge, and effective capacitance. Quantitative comparisons with manufacturer data show that the proposed model provides meaningful identification of the model parameters. Further, quantitative analyses through hysteresis voltage identification justify the improvement of the proposed model over traditional model.

Chapter 5

Position Self-sensing of Piezoelectric Actuators

Piezoelectric actuators demonstrate nonlinear phenomena such as hysteresis and creep at different frequency ranges [26, 30, 43]. Examples of hysteresis and creep behavior are shown in Figure 5.1, where the actuator position is plotted against applied voltage for frequencies ranging from 0 Hz (creep) to 100 Hz. Usually, feedback position sensors are used to mitigate these nonlinearities successfully. However, there are many applications where dedicated position sensors are difficult to implement due to space and/or cost constraints. Examples for applications that suffer from these constraints are fuel injectors, inkjet printing nozzles, micro-pumps etc. Moreover, an additional component may affect the overall reliability of the control system. Chapter 1 highlighted some of the model based sensorless position control techniques for piezoelectric actuators that have been used to avoid additional sensor elements. These techniques are designed to compensate for hysteresis (Section 1.6.3) and creep phenomena (Section 1.3). However, these sensorless control techniques are typically designed for a very narrow frequency range. Thus, they cannot simultaneously compensate for both creep and rate-dependent hysteresis effects. Moreover, an accurate model is a prerequisite for these sensorless control schemes. These models are often difficult to obtain and susceptible to modeling uncertainties [11, 12]. A number of studies include a feedforward model to a dedicated feedback sensor (Section 1.7.3) in order to improve the dynamic properties of the feedback system. This approach improves the bandwidth of the controller and leads to more robustness towards modeling uncertainties.

Position self-sensing (PSS), which was first proposed for vibration suppres-

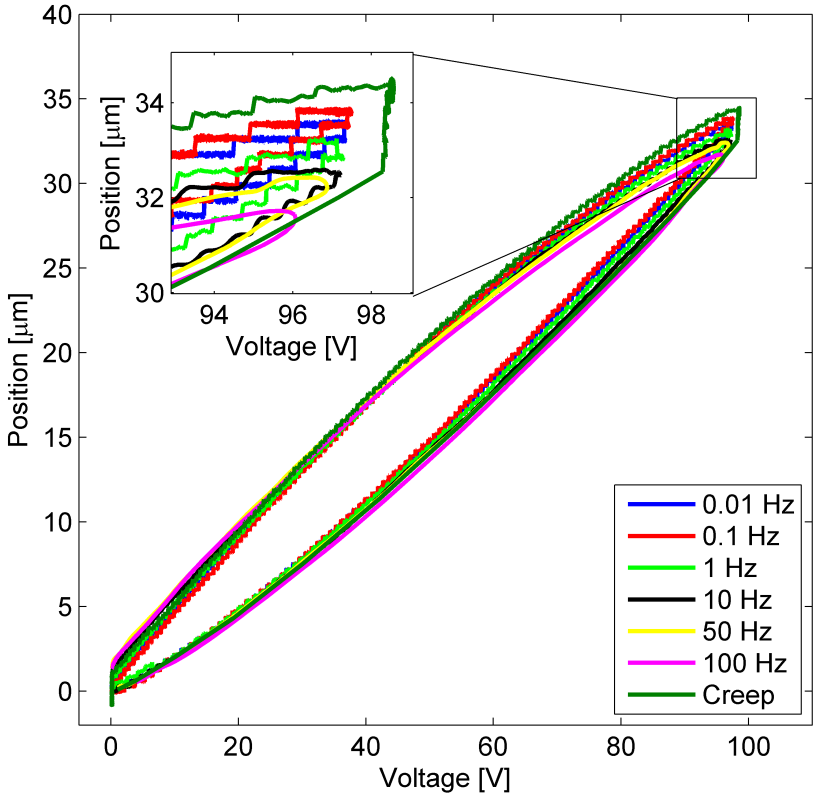

Figure 5.1: Rate-dependent hysteresis and creep at different frequencies (Reprinted with permission [61]. Copyright 2012, American Institute of Physics.)

sion in different structures [72], is another technique used to improve actuator positioning. In this approach, a single piezoelectric element is used both as a sensor and an actuator. True collocation of actuator and sensor is realized based on the direct and indirect effect of piezoelectricity. A capacitance bridge circuit is used to extract strain or position. This approach is often used in piezoelectric cantilevers or patches. Jones et al. [104] implemented this approach with multilayered actuators for micro positioning. The self-sensing approach works well assuming ideal conditions. However, in practice, this approach poses a number of challenges. The main problem is associated with the bridge balancing since it employs a similar capacitor as the piezoelectric capacitance where the accurate measurement of the piezoelectric capacitance is difficult [62, 73]. So, any change in the piezoelectric actuator capacitance other than the strain may affect the measurement and hence the overall control system. The capacitance bridge based self-sensing is presented in Section 1.8.1. Unlike voltage, piezoelectric charge flow is found to be linearly related to the position over a wide range of frequencies [13, 52]. Figure 5.2 shows the charge-position relationship from 10 Hz to 300 Hz with negligible hysteresis. A linear fitting line with a slope of a_0 is also shown in Figure 5.2. Based on this linear relationship, charge based controllers are designed. Charge based PSS can also be realized relying on the linear charge-position relationship. In this case, current is integrated and the piezoelectric actuator position is obtained from the charge measurement. In this approach, the major challenge is the charge drift due to an offset current which result in estimated position drift specially during slow operations (<10 Hz). Section 1.8.2 highlights the charge based self-sensing scheme in more detail. The other self-sensing technique presented in Section 1.8.3 is based on the direct effect of piezoelectricity where a portion of the actuator is designed to function as sensor. Due to the strain in the piezoelectric actuator, a voltage is induced. The induced voltage is proportional to the actuator displacement and position information is obtained from the induced voltage. The major shortcoming in this technique is that the actuator range is reduced since some of the actuator is used as a sensor.

The real-time effective capacitance measurement of the piezoelectric actuator presented in Chapter 3 provides yet another avenue to estimate actuator po-

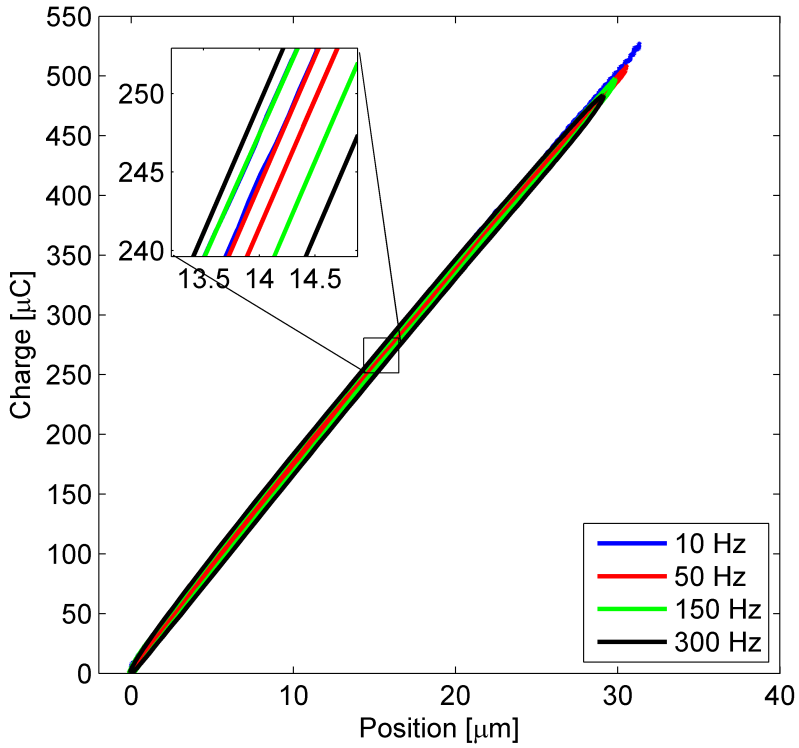

Figure 5.2: Charge-position relationship over a frequency range of 10 Hz – 300 Hz ([88] ©2013 IEEE)

sition. Here one exploits the finding that the position of the actuator is related to effective capacitance with negligible (<3%) hysteresis. The problem with the capacitance based PSS is that the signal is noisy and requires low pass filtering which limits its application to slow operations (<10 Hz).

All of the self-sensing techniques discussed so far have advantages and shortcomings. By combining charge based PSS and capacitance based PSS which on their own only work well for high and low driving frequencies respectively, a position self-sensing for a wide frequency range can be achieved. It is important to define the high and low frequencies at this point. By high frequency, it refers to the range where the actuator is driven below the range to avoid the vibrational dynamics (see Figure 1.4). To this end, a novel hybrid position observer (HPO) is developed which fuses the charge based PSS and capacitance based PSS. It achieves good position estimates over a wide range of frequencies where both creep and hysteresis effects are present. The objective of this chapter is to introduce position estimation using the HPO. The following sections will detail the two PSS approaches, the operating principle of the HPO, and the implementation of the HPO. Finally, the HPO results are compared with a dedicated position sensor.

5.1 Charge Based Position Self-sensing, $\hat{x}_I$

Charge based PSS is based on the linear fitting of the charge-position relationship shown in Figure 5.2. The maximum position error observed in the center of the curve is less than one micrometer (<3% of the maximum stroke) for a frequency range of 10-300 Hz. This experimental linear relationship can also be found analytically. By manipulating the piezoelectric constitutive Equations 1.4 and 1.5, an expression relating charge to position can be obtained,

$$q = C_P \frac{m\ddot{x} + b\dot{x} + kx - F}{\alpha} + \alpha x. \tag{5.1}$$

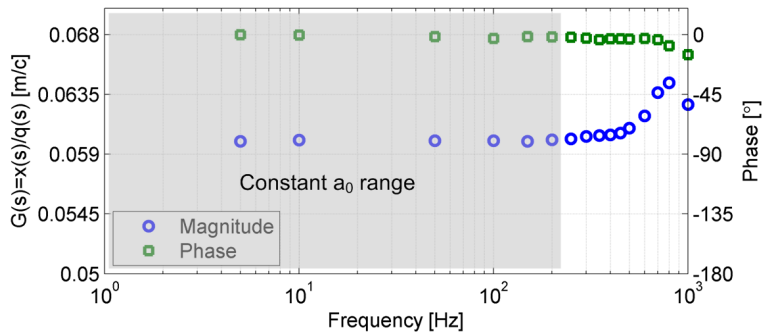

Figure 5.3: Magnitude and phase response ([88] ©2013 IEEE)

If external Force, F is neglected, then Equation 5.1 can be transformed into a transfer function in the Laplace-domain,

$$G(s) = \frac{x(s)}{q(s)} = \frac{x(s)s}{I(s)} = \frac{1}{\frac{C_P}{\alpha}(ms^2 + bs + k) + \alpha}. \tag{5.2}$$

Figure 5.3 shows the measured frequency response of $G(s)$. The targeted frequency range (<150 Hz) in this research is well below the mechanical natural frequency of the test setup (2500 Hz) and the electromechanical resonance frequency (700 Hz). Hence, the dynamic terms in Equation 5.1 are neglected and the following simplified expression is obtained for relating estimated position, $\hat{x}_I$ to measured charge, $\bar{q}$ through $\hat{G}(s)$:

$$\hat{G}(s) = \frac{\hat{x}_I(s)}{\bar{q}(s)} = \frac{1}{\alpha + C_P\frac{k}{\alpha}} = \frac{1}{a_0}. \tag{5.3}$$

The dynamic transfer function $G(s)$ in Equation 5.2 reduces to a constant gain in the reduced frequency transfer function $\hat{G}(s)$. Traditional feedforward charge control schemes use Equation 5.3 by controlling the amount of charge supplied to the piezoelectric actuator. Rather than controlling charge, charge based PSS integrates measured current, I to obtain charge and hence position from the charge measurement. Figure 5.2 presents the position estimation technique from charge measurement based on Equation 5.3. To differentiate between the

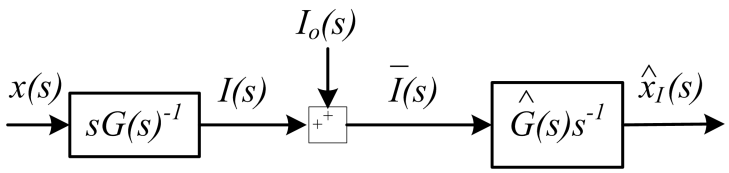

Figure 5.4: Position estimation from charge measurement ([88] ©2013 IEEE)

measured quantities and estimated quantities, a 'bar' above the variables is used to represent the measured quantities and 'hat' is used for estimated values.

The main challenge with this approach is charge leakage, which requires sophisticated hardware architectures. Charge leakage leads to an offset current, I_0 which results in a drift of identified charge and hence estimated position. To identify and compensate for the amount of offset current, a second low frequency position estimate based on an effective piezoelectric capacitance measurement is proposed. The next section details the capacitance based PSS.

5.2 Capacitance Based Position Self-sensing, $\hat{x}_{C_P}$

Effective piezoelectric capacitance measurement is discussed in Chapter 3. Figure 5.5 shows that the piezoelectric capacitance changes with stroke with little hysteresis (<3% maximum stroke). Based on a real-time measurement, effective capacitance provides a means for position self-sensing. To yield the position information from the effective capacitance measurement, a higher order polynomial is chosen. For fitting purpose, 0.1 Hz is selected which lies in between 0.01 Hz to 1 Hz. Equation 5.4 presents the fitting function, Γ for capacitance based PSS,

$$\Gamma = \hat{x}_{C_P}(\bar{C}_P) = b_0 + \sum_{j=1}^{5} b_j C_P^j, \tag{5.4}$$

where, j is the order of the polynomial and b_0 and b_j are the constant and the coefficients of the polynomial. To obtain the order of the polynomial, j, the relationship between capacitance and position is fitted with different orders and the residuals and standard errors were compared to obtain a reliable fitting of the

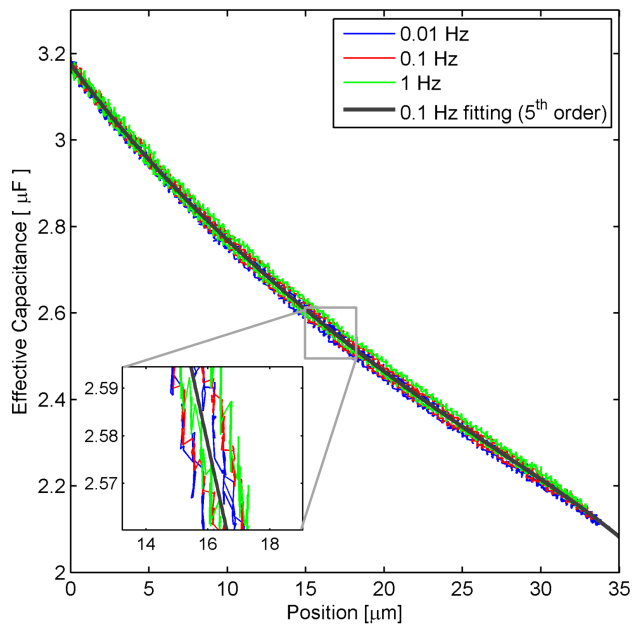

Figure 5.5: Capacitance-position relationship at low frequencies

capacitance and position. The Microsoft Excel® Data Analysis Toolbox is used to analyze the data. Table 5.1 presents the standard errors and maximal residual errors of the fitting at different polynomial orders of capacitance-position relationships at 0.1 Hz.

Polynomials of different orders and logarithm relationship are presented in Figure 5.6. The residual errors for different fits are presented in Figure 5.7. The residual plots show that the overall errors are close for different orders. However, for order 3 the error is large at the end of stroke (~1 μm) while for order 5, the error is close to 0.4 μm. Although the improvement due to higher order fitting is not significant in comparison to the maximum residual errors, the higher order fitting is important for creep since the error due to creep is similar in magnitude (~1μm) for lower order fitting (j=3).

Based on the maximum residual errors in Table 5.1 and considering the effect of creep, the order of the polynomial fit is selected at 5 which provides a reasonable fit for the capacitance-position relationship. In addition to the residual error, the adjusted R^2 values indicate that an order of 5 or 6 provides the best

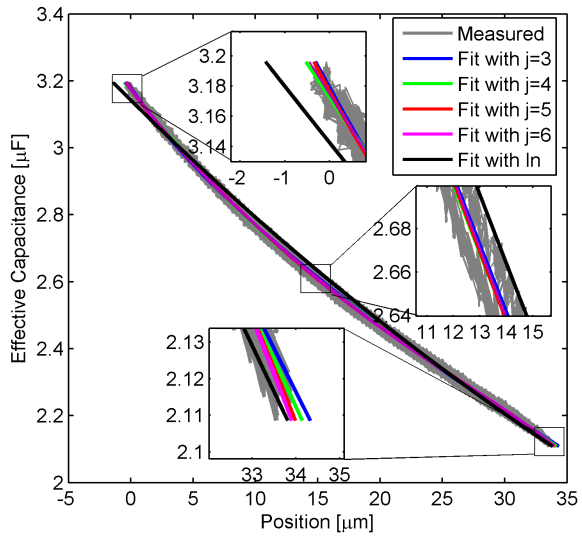

Figure 5.6: Capacitance-position relationship at low frequencies

regression model. The ANOVA of the regression model (j =5) is shown in Table 5.2 where coefficients and intercept for the model are shown. The p-values indicate that all the coefficients are significantly important. The block diagram

Table 5.1: Fitting errors in regression models of different orders

Parameters	j=3	j=4	j=5	j=6	ln
Maximum residual error [μm]	1.34	1.24	1.17	1.15	1.49
R^2 value	0.99881	0.99886	0.99889	0.99889	0.997
Adjusted R^2 value	0.99881	0.99886	0.99889	0.99889	–

of the capacitance based PSS is shown in Figure 5.8. Due to the noise in the capacitance measurement, the capacitance based PSS is only applicable for low frequencies.

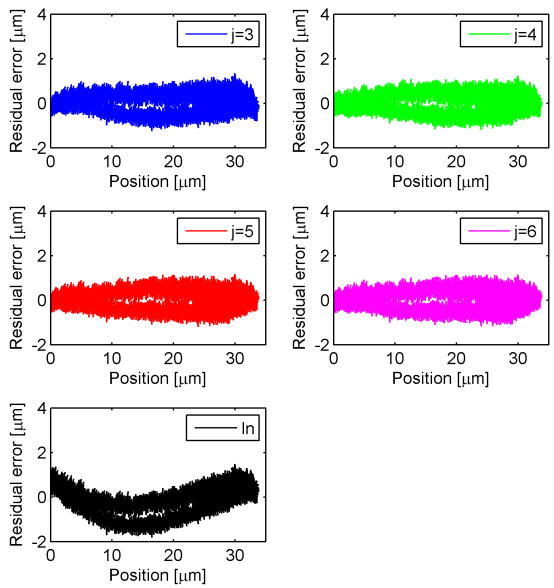

Figure 5.7: Capacitance-position relationship at low frequencies

Table 5.2: ANOVA table for capacitance based PSS regression model

ANOVA for j=5	Df	SS	MS	F	Significance F
Regression	5	2058890	411777.9	2581465	0
Residual	14369	2292.046	0.159513		
Total	14374	2061182			

	Coefficients	t Stat	p-value
b_0	-4560.5	-19.9951	0
b_1	8773.922	19.99799	0
b_2	-6589.93	-19.6115	0
b_3	2445.475	19.09276	0
b_4	-450.855	-18.5542	0
b_5	33.10029	18.03204	0

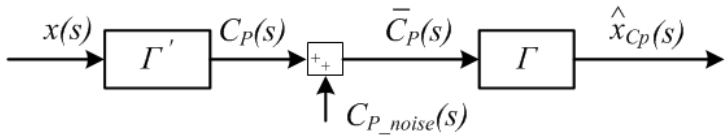

Figure 5.8: Position estimation from capacitance measurement ([88] ©2013 IEEE)

5.3 Hybrid Position Observer Design

Since the charge based PSS provides position estimate at relatively high frequencies (below the high dynamic range shown in Figure 1.4) and capacitance based PSS is suitable only at low frequencies, a hybrid position observer (HPO) is proposed which utilizes both PSS signals for position estimation. The block diagram of the hybrid position observer is shown in Figure 5.9 where the previously discussed charge based PSS is fused with capacitance based PSS. The shaded section of the Figure represents the real system while, the clear section represents the HPO. The structure of the HPO is very similar to a conventional observer. The plant model, which is represented by $\frac{\hat{G}(s)}{s}$ is driven by the measured current, $\bar{I}$. The position obtained through effective capacitance, $\hat{x}_{C_P}$ can be thought of as a measurement unit in a traditional observer structure. In contrary to a conventional observer however, the feedback term $L(s)$ is not used to adjust the poles of the plant, but rather to estimate the offset current, $\hat{I}_0$ present in the measured current, $\bar{I}$. The estimated $\hat{I}_0$ is then subtracted from the measured current to eliminate the drift in charge based PSS. This is achieved through the use of a proportional plus integral operator:

$$L(s) = L_P + \frac{L_I}{s}. \tag{5.5}$$

The identified current offset is then subtracted from the current measurement. Assuming that the modeled plant, $\hat{G}(s)$ equals the real plant, $G(s)$, the following transfer functions for the estimated position signal, $\hat{x}$ can be obtained:

$$\frac{\hat{x}(s)}{x_I(s)} = \frac{1}{1 + s^{-1}\hat{G}(s)L(s)} = \frac{a_0 s^2}{a_0 s^2 + L_P s + L_I}, \tag{5.6}$$

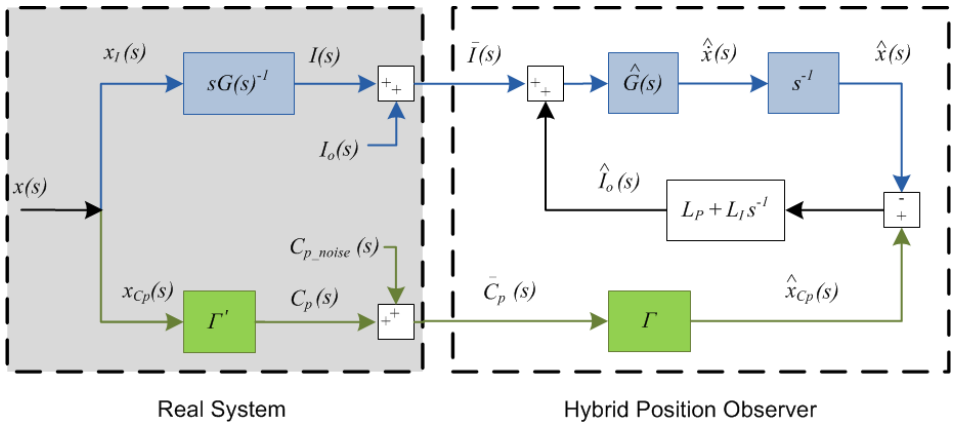

Figure 5.9: Hybrid position observer (Reprinted with permission [61]. Copyright 2012, American Institute of Physics.)

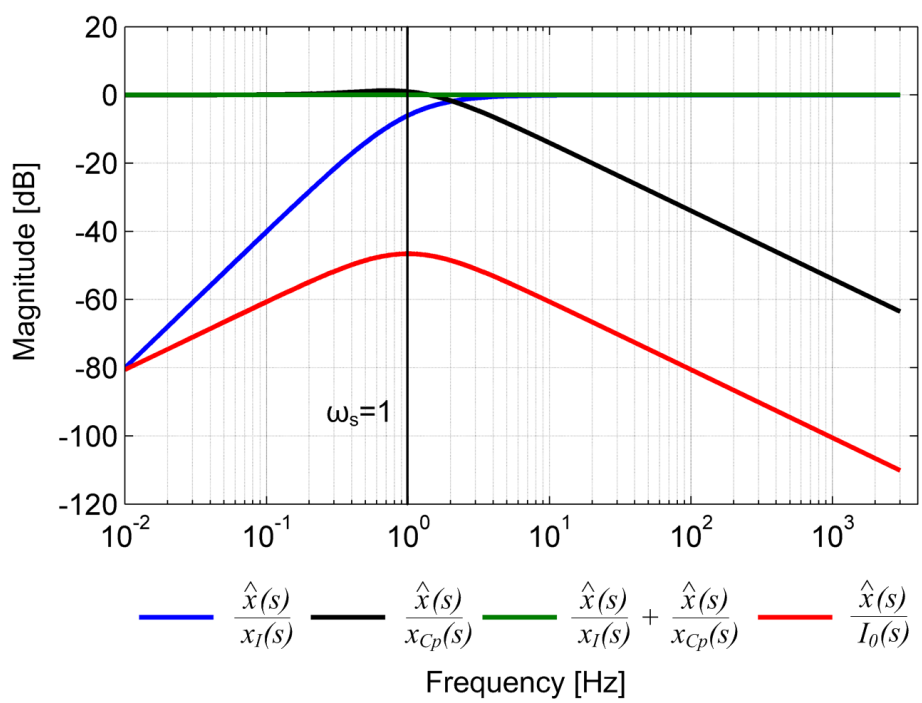

Figure 5.10: Magnitude plot of different transfer function (Reprinted with permission [61]. Copyright 2012, American Institute of Physics.)

Table 5.3: Hybrid position observer parameters ([88] ©2013 IEEE)

Parameter	Units	Value
Charge-position transfer fucntion, a_0	$C \cdot m^{-1}$	17
Observer transition frequency, ω_S	$rad \cdot s^{-1}$	2π
Observer damping, ζ_S		1
Observer proportional gain, L_P	$C \cdot rad \cdot s^{-1} \cdot m^{-1}$	213.60
Observer integral gain, L_I	$C \cdot rad^2 \cdot s^{-2} \cdot m^{-1}$	641

$$\frac{\hat{x}(s)}{I_o(s)} = \frac{\hat{G}(s)}{1 + s^{-1}\hat{G}(s)L(s)} = \frac{s}{a_0 s^2 + L_P s + L_I}. \tag{5.7}$$

Assuming further, $\hat{x}_{C_P}(s) = x_{C_P}(s)$, the following relationship can be deduced:

$$\frac{\hat{x}(s)}{x_{C_P}} = \frac{s^{-1}\hat{G}(s)L(s)}{1 + s^{-1}\hat{G}(s)L(s)} = \frac{L_P s + L_I}{a_0 s^2 + L_P s + L_I}. \tag{5.8}$$

Figure 5.10 presents the magnitude response of the resulting transfer functions for $\frac{\hat{x}(s)}{x_I(s)}$, $\frac{\hat{x}(s)}{x_{C_P}(s)}$, $\frac{\hat{x}(s)}{x(s)}$ and $\frac{\hat{x}(s)}{I_0(s)}$. Below the switching frequency, ω_S=1 Hz, the capacitance based PSS (black line) is dominant and above ω_S, charge based PSS (blue line) is favoured. The sum of the two PSS techniques has a constant unity gain (green line). Also, the offset current, $I_0(s)$ (red line) is attenuated with at least $-45\ dB$. Constant offset currents are rejected entirely. Thus, the estimated output obtains the same magnitude as the actual position, x and a low frequency current offset, I_0 is eliminated. Moreover, the capacitance based PSS provides position estimates at low frequencies. By choosing appropriate values for the coefficients of $L(s)$, a transition frequency, ω_S is selected between the effective capacitance based PSS and the charge based PSS.

$$L_P = 2\omega_S a_0, L_I = \omega_S^2 a_0. \tag{5.9}$$

The switching frequency, ω_S is selected larger than the frequency of the offset current, I_0 and smaller than the noise in the capacitance measurement. In the experiments, good results are obtained with $\omega_S = 2\pi$ rad$\cdot s^{-1}$. A complete set of HPO parameters is listed in Table 5.3.

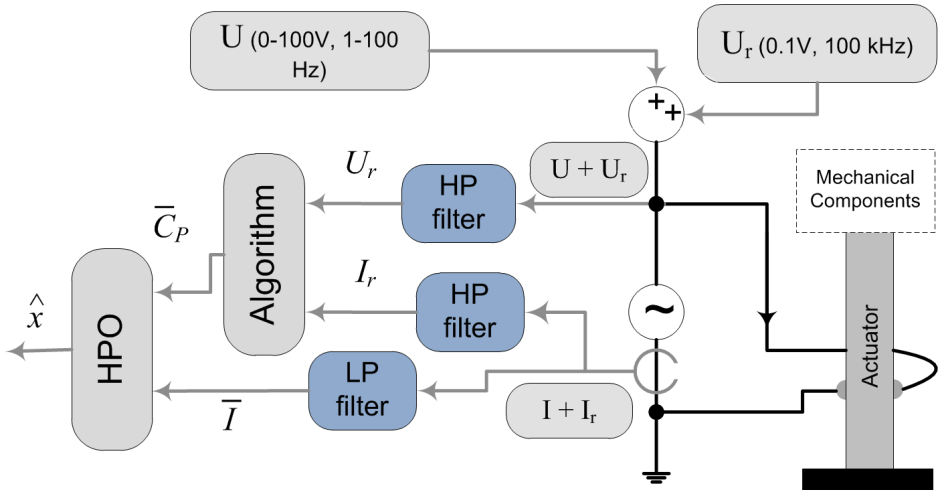

Figure 5.11: Hybrid position observer implementation ([88] ©2013 IEEE)

5.4 Hybrid Position Observer Implementation

The flowchart of the HPO self-sensing setup is presented in Figure 5.9. The actuator is fed with a low frequency driving voltage, U for positioning and high frequency ripple voltage, U_r for effective capacitance measurement. The low frequency voltage, U creates a driving current, I which upon integration, provides a charge measurement that is employed to infer the position from Equation 5.3. The high frequency voltage, U_r provides a high frequency ripple current which are separated and processed to obtain the effective capacitance measurement through the algorithm shown in Chapter 3. A second position measurement is obtained from the effective capacitance measurement using Equation 5.4. Based on the two position self-sensing measurements, the HPO provides a reliable position estimate over a frequency range from 0 to 125 Hz.

5.5 Open Loop HPO Performance

To evaluate the performance of the HPO, the position estimated from the HPO is compared with a position sensor (laser vibrometer) during open loop operations. In the first experiment, the actuator is driven with sinusoidal fre-

Table 5.4: Observer error, ($\epsilon_O = \bar{x} - \hat{x}$) at different frequencies (Reprinted with permission [61]. Copyright 2012, American Institute of Physics.)

Frequency $[Hz]$	Maximum error $[\mu m]$	Maximum Stroke $[\mu m]$	% Error
0.01	0.88	33.82	2.6
0.1	0.42	33.56	1.3
1	0.59	33.11	1.8
10	1.00	32.56	3.1
50	0.79	32.41	2.4
100	0.78	31.68	2.5

quencies between 0.01 Hz – 100 Hz and a magnitude of 100 V. Figures 5.12 and 5.13 show the measured position, HPO position and error between the two measured responses. The error percentages are also shown in Table 5.4. For a frequency range of 0.01 Hz to 100 Hz, the maximum error is recorded at 3.1% of the maximum stroke.

In addition to the variable frequency range, the HPO is also tested in the presence of creep. To test the creep behavior, a sinusoidal transient of 0.01 seconds (50 Hz) length and 100 V magnitude is followed by a constant 100 V driving voltage over 175 seconds. Figure 5.14 shows the results of this experiment. The HPO shows a maximum error of 2.16% during the transient and the steady-state portion of the experiment. In the steady-state region, the error is less than 1.5%. The amount of creep is not substantial in comparison to the hysteresis behavior. Since the observer error does not increase during the constant voltage phase, and both laser and HPO show the same trend in position, it is concluded that the HPO provides an estimation of creep at least qualitatively. This will be verified further in Chapter 6 that describes closed loop control using the HPO as a feedback sensor.

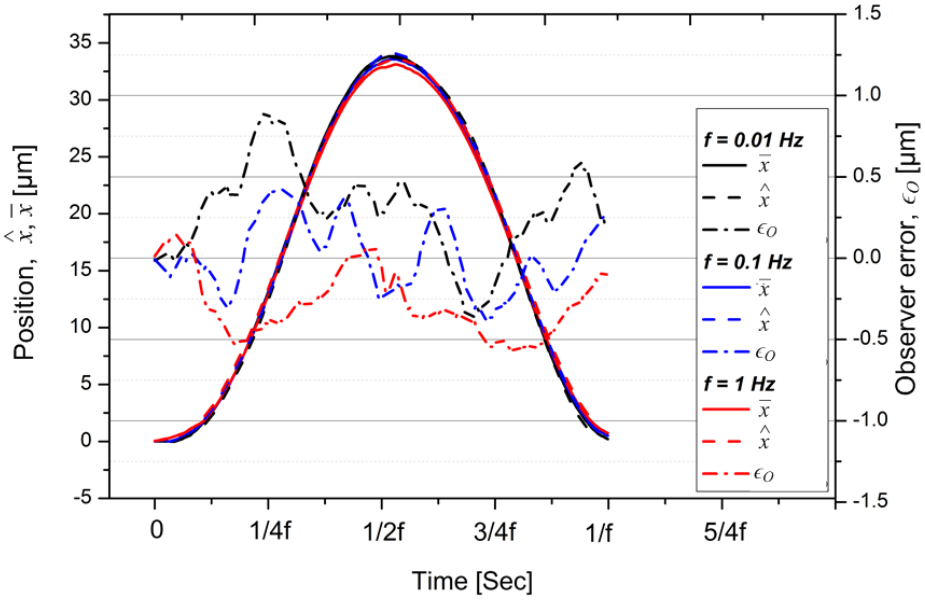

Figure 5.12: Measured position, HPO position and observer error between 0.01 Hz and 1 Hz (Reprinted with permission [61]. Copyright 2012, American Institute of Physics.)

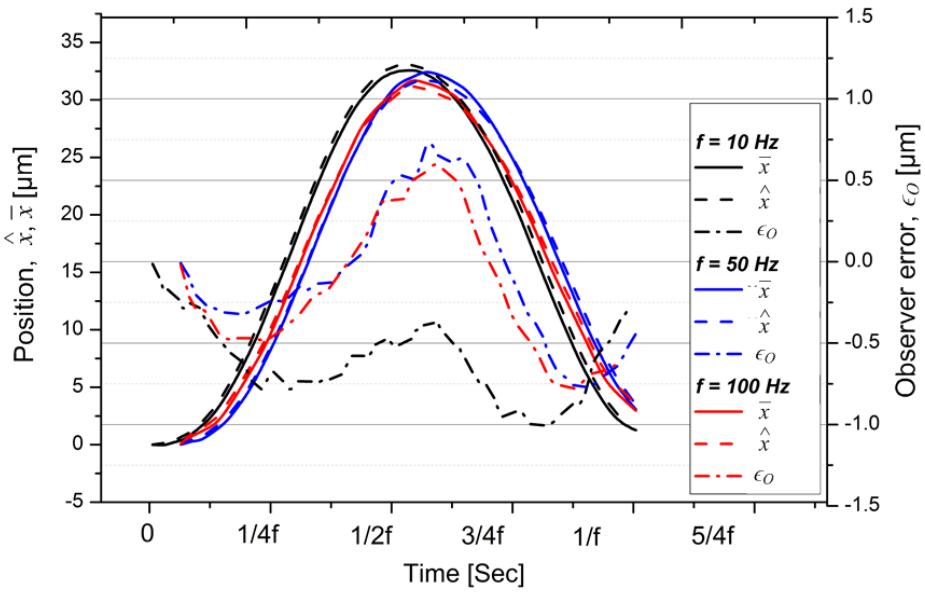

Figure 5.13: Measured position, HPO position and observer error between 10 Hz and 100 Hz (Reprinted with permission [61]. Copyright 2012, American Institute of Physics.)

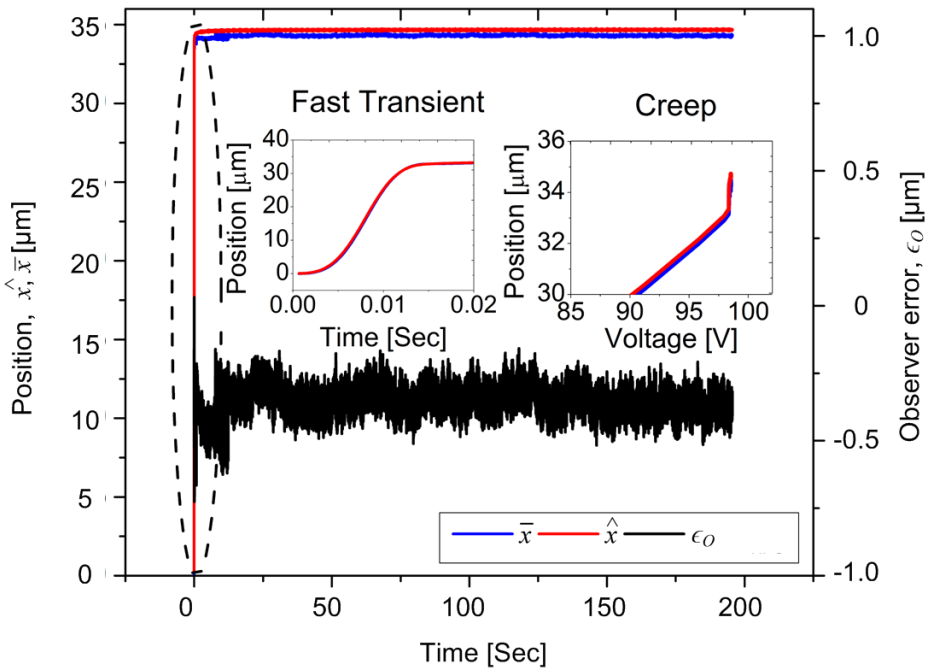

Figure 5.14: Measured position, HPO position and observer error between 50 Hz and DC signal in the presence of creep (Reprinted with permission [61]. Copyright 2012, American Institute of Physics.)

5.6 Summary

Position self-sensing technique provides an alternative to traditional position sensors where mounting a dedicated position sensor is not feasible. In this chapter, a novel HPO approach is presented which relies on two different PSS schemes: 1) PSS based on current or charge measurement and 2) PSS based on effective capacitance measurement. The charge based PSS provides a good PSS signal at high frequencies while the capacitance based PSS provides reliable position estimate at low frequencies. The proposed HPO provides an improved position self-sensing over a wide frequency range by combining the advantages of each PSS technique. The HPO performance is compared with a traditional position sensor in open loop condition for sinusoidal signals with frequencies between 0 Hz and 100 Hz. This frequency range contains both creep and rate-dependent hysteresis. The proposed HPO provides around 3% error over the whole range of operation which makes it applicable for real-time applications and a potential substitute of traditional position sensors.

Chapter 6

Self-sensing Position Control of Piezoelectric Actuators

A novel position observer (HPO) is developed in Chapter 5 by fusing two self-sensing signals to obtain an improved position signal over a wide frequency range. It is also shown how accurately the HPO can predict the position in open loop and the results are compared with a traditional sensor. The objective of this chapter is to show that the HPO can be used as a reliable substitute for a traditional position feedback sensor in the control of soft piezoelectric actuators. To show the HPO performance in closed loop, results with HPO feedback is compared with the results obtained by a traditional position sensor. To minimize the steady-state error, a simple integral controller is used in this research. Different types of profiles including long DC signals and AC signals with variable frequencies and lifts are part of the comparison.

The advantages of the HPO feedback system are: 1) it is based on self-sensing technique (no position sensor is required), 2) it is voltage controlled (no sophisticated hardware requirement), 3) it does not require a hysteresis model, and 4) a wide frequency range from DC to 125 Hz.

6.1 The Integral Controller

Integral controllers with dedicated feedback sensors are often used in piezoelectric systems due to hysteresis and unknown force disturbances. The major advantage of the I–controller is it provides high gain which can overcome hysteresis problems when operated at frequencies below the vibrational dynamics [11]. One of the pitfalls of the I–controller is a velocity dependent error at high frequencies typical for a Type–I control system. At higher frequencies, the track-

ing error is quite substantial and more advanced control strategies that include a feedforward branch [15, 27, 46, 48] could be implemented for improved tracking. However, the main objective in this chapter is to validate the performance of the HPO in the closed loop and so no feedforward strategy is added.

The simple integral control schematic is shown in Figure 6.1. The plant model, $P(s)$ is obtained from the constitutive relationship in Equations 1.4 and 1.6, assuming zero hysteresis voltage, U_H, and neglecting small external forces, F. Since the targeted frequency range is much lower than the mechanical natural frequency of the plant, the mass and damping terms can be neglected and the following relationship is established for the plant model:

$$P(s) = \frac{x(s)}{U_P(s)} = \frac{\alpha}{ms^2 + bs + k} \approx \frac{\alpha}{k}. \tag{6.1}$$

The overall transfer function for this simple linear plant with an integral controller gain, K_I is given by:

$$\frac{x(s)}{x_R(s)} = \frac{K_I \frac{\alpha}{k}}{s + K_I \frac{\alpha}{k}} = \frac{\omega_C}{s + \omega_C}. \tag{6.2}$$

The position controller gain is obtained by selecting a control bandwidth, ω_C, and using the identified model parameter, $\frac{k}{\alpha}$,

$$K_I = \frac{\omega_C k}{\alpha}. \tag{6.3}$$

In this application, ω_C is selected at 250 Hz which is at least twice the maximum targeted frequency range. The ratio of $\frac{k}{\alpha}$ can be obtained from the parameter identification section. For simplicity, the term can also be estimated from the ratio of maximum voltage to maximum stroke neglecting hysteresis at maximum displacement using Equation 4.3.

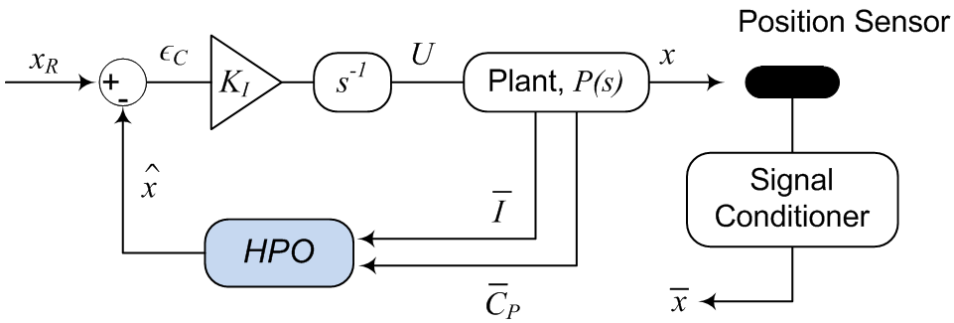

Figure 6.1: An integral controller schematic

6.2 Experimental Results

To achieve sensorless position control, the HPO is used as a feedback position sensor in the piezoelectric system. To investigate the performance of the HPO in a controlled environment, different profiles have been tested: 1) step profile with variable lift (P_1), 2) sinusoidal profiles (P_2), and 3) DC profile with fast transient (P_3). To gauge the accuracy of the HPO, a laser vibrometer is added to the experiment for reference position measurements. The laser vibrometer is not used in the control loop. It simply provides an absolute reference to compare the position estimates of HPO to measured position (from laser vibrometer). The primary objective of the experiments then is to investigate the tracking error between the position measurement of the laser vibrometer, $\bar{x}$, and the position estimate of the HPO, $\hat{x}$. This error is denoted as observer error, ϵ_O. The other error of interest is the total error, ϵ_T which is calculated from the difference between the reference position, x_R and the position measured with the reference laser sensor, $\bar{x}$. The controller error, ϵ_C is calculated from the difference between the reference position, x_R, and the HPO position, $\hat{x}$.

6.2.1 Step Profile with Variable Strokes, P_1

The HPO performance is evaluated for profile, P_1 (in Figure 6.2(a)) which includes the variable lifts (minor loops) in both ascending and descending paths. Figure 6.2(a) shows the reference signal, x_R, the open loop response and the

closed loop response. The open loop response shows a large overshoot (due to step profile) while in the closed loop response with the HPO feedback, there is no overshoot observed. The response times are in the same order of magnitude (<5 ms) for both the open loop and the closed loop experiments. In Figure 6.2(b) the errors are plotted. The observer error in closed loop operation between the laser vibrometer and the HPO, $\epsilon_{O_{CL}}$ is recorded at less than 0.82 μm, both during transients and in the steady-state conditions. To compare the steady-state errors, steady-state segments (t_{ss}:'a'–'h') are defined by Equation 6.4 where, t_p is the width of the pulse and t_s is the settling time of the measured signal.

$$t_{ss} = t_p - t_s. \tag{6.4}$$

Settling time, t_s is equal to 5 time constants, $\frac{5}{\omega_C}$ where, ω_C is the controller bandwidth. The open loop total error ($\epsilon_{T_{OL}}$) and closed loop total error ($\epsilon_{T_{CL}}$) are also compared over segments 'a'– 'h' in Figure 6.2. Due to hysteresis in the open loop condition, $\epsilon_{T_{OL}}$ reaches up to 2.75 μm. In the closed loop condition, $\epsilon_{T_{CL}}$ is less than 0.67 mum. In the segments 'a'– 'h', maximum values of total error, $\epsilon_{T_{CL}}$ and maximum values of observer error, $\epsilon_{O_{CL}}$ are marked with circles. Due to the variation in the experiments, 50 tests were performed and statistical inference is obtained over the segments 'a'– 'h' based on the maximum values of $\epsilon_{T_{CL}}$, $\epsilon_{T_{OL}}$, and $\epsilon_{O_{CL}}$ in each test. The statistical results over the maximum errors ($\epsilon_{T_{CL}}$, $\epsilon_{T_{OL}}$, and $\epsilon_{O_{CL}}$) are shown in Table 6.1. The mean of the maximum total error during open loop experiments is 2.69 μm which is 8.97% of the maximum stroke. The mean of the maximum total error in closed loop, $\epsilon_{T_{CL_{max}}}$ is 0.78 μm which is 2.6% of the maximum position and a 71% improvement over the conventional open loop control strategy. The mean of the maximum observer error, $\epsilon_{O_{CL_{max}}}$ is 0.72 μm which is 2.4% of the maximum lift.

6.2.2 Sinusoidal Profile with Different Frequencies, P_2

Four types of sinusoidal profiles are used to show the tracking performance of the control system. The first sinusoidal profile, P_{2a}, uses a single low fre-

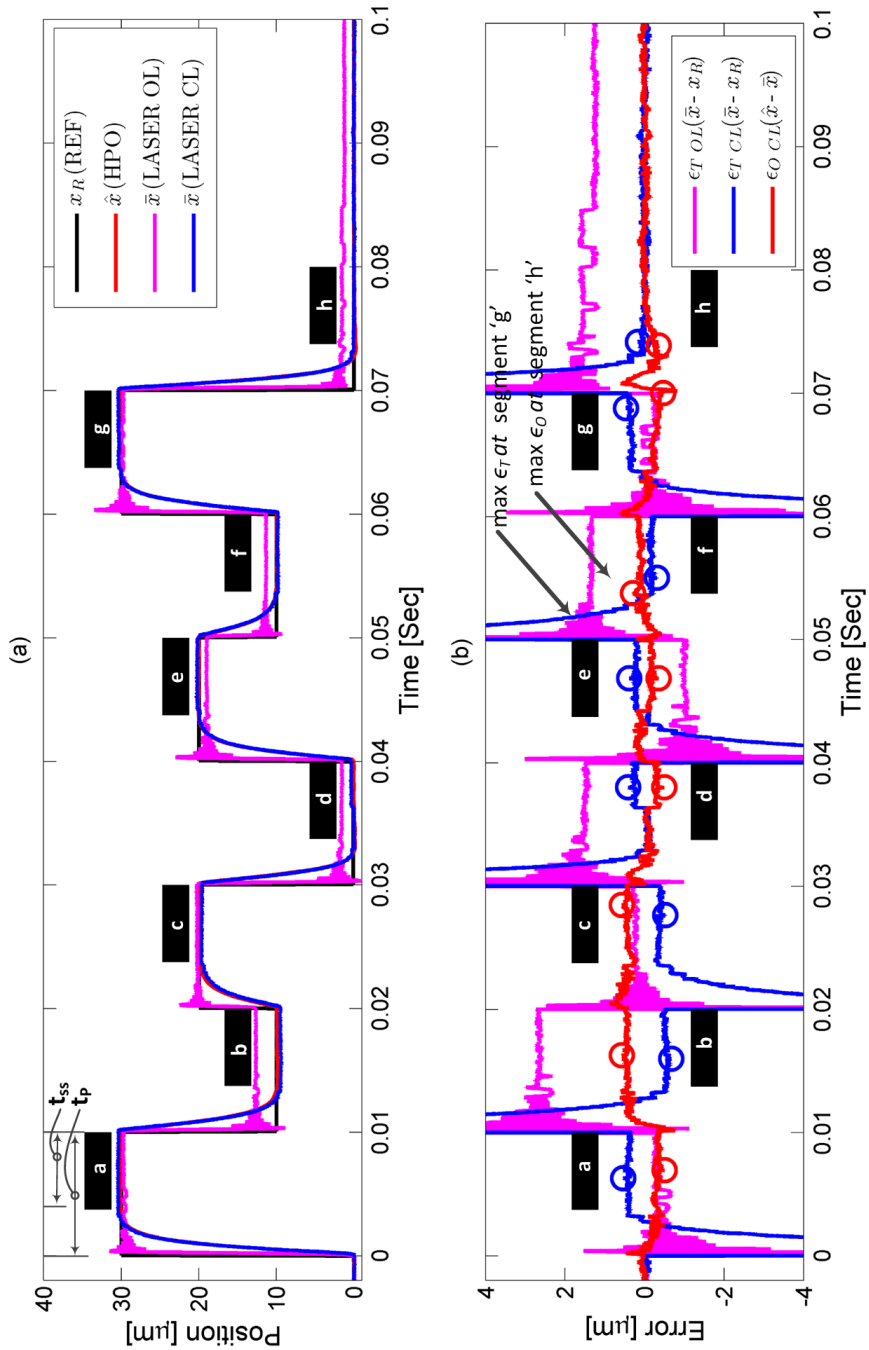

Figure 6.2: (a) P_1 reference position, HPO position, measured open loop and closed loop position (b) Total error (open loop and closed loop) and closed loop observer error; maximum closed loop total error and observer error in each segment ([88] ©2013 IEEE)

Table 6.1: Steady-state errors at segments 'a'– 'h' for P_1 ([88] ©2013 IEEE)

Test Statistics [μm]	*Segments* a	b	c	d	e	f	g	h
$\max(\epsilon_{T_{OLmax}})$	0.89	3.08	0.89	1.75	1.73	1.62	0.76	1.85
$\text{mean}(\epsilon_{T_{OLmax}})$	0.54	2.69	0.60	1.38	1.33	1.34	0.48	1.52
$\sigma(\epsilon_{T_{OLmax}})$	0.15	0.16	0.14	0.14	0.17	0.15	0.10	0.17
$\max(\epsilon_{T_{CLmax}})$	0.83	0.99	0.83	0.82	0.89	0.66	0.95	0.63
$\text{mean}(\epsilon_{T_{CLmax}})$	0.45	0.78	0.58	0.34	0.40	0.36	0.63	0.31
$\sigma(\epsilon_{T_{CLmax}})$	0.18	0.14	0.17	0.15	0.17	0.11	0.17	0.13
$\max(\epsilon_{O_{CLmax}})$	0.78	0.93	0.85	0.90	0.78	0.64	0.92	0.84
$\text{mean}(\epsilon_{O_{CLmax}})$	0.41	0.72	0.56	0.44	0.39	0.38	0.58	0.40
$\sigma(\epsilon_{O_{CLmax}})$	0.18	0.14	0.15	0.15	0.14	0.11	0.16	0.14

quency at $\frac{1}{25^{th}}$ of the controller bandwidth:

$$P_{2a} : x_R = [15 - 15cos(20\pi t)]\mu m.$$

The second profile, P_{2b}, uses a single high frequency at half the controller bandwidth:

$$P_{2b} : x_R = [15 - 15cos(250\pi t)]\mu m.$$

The third profile, P_{2c}, uses four separate frequencies with the highest frequency at $\frac{1}{5^{th}}$ of the controller bandwidth:

$$P_{2c} : x_R = 17.6 - 4.4[cos(20\pi t) + cos(30\pi t) + cos(80\pi t) + cos(100\pi t)]\mu m.$$

The fourth profile, P_{2d}, uses four separate frequencies with the highest frequency at $\frac{1}{2.5^{th}}$ of the controller bandwidth.

$$P_{2d} : x_R = 17.6 - 4.4[cos(60\pi t) + cos(100\pi t) + cos(150\pi t) + cos(200\pi t)])\mu m.$$

Figure 6.3(a) shows the open loop and closed loop responses of P_{2a} (at 10 Hz). The errors are plotted in Figure 6.3(b). The observer error in closed loop,

Table 6.2: Error comparison for different profiles ([88] ©2013 IEEE)

Profile type	Error type	Error [μm]	% error
P_{2a}	$\epsilon_{O_{CL}}$	0.82	2.74
	$\epsilon_{C_{OL}}$	0.69	2.3
	$\epsilon_{T_{CL}}$	1.46	4.86
	$\epsilon_{T_{OL}}$	3.51	11.72
P_{2b}	$\epsilon_{O_{CL}}$	0.92	3.08
	$\epsilon_{C_{CL}}$	9.84	32.82
	$\epsilon_{T_{CL}}$	9.7	32.34
	$\epsilon_{T_{OL}}$	6.93	23.11
P_{2c}	$\epsilon_{O_{CL}}$	0.91	3.04
	$\epsilon_{C_{OL}}$	2.32	7.74
	$\epsilon_{T_{CL}}$	2.81	9.29
	$\epsilon_{T_{OL}}$	4.52	15.08
P_{2d}	$\epsilon_{O_{CL}}$	0.89	2.95
	$\epsilon_{C_{CL}}$	4.42	14.74
	$\epsilon_{T_{CL}}$	4.74	15.81
	$\epsilon_{T_{OL}}$	5.86	19.54

$\epsilon_{O_{CL}}$ is less than $0.82\mu m$ which is 2.74% of the total error. There is a considerable (64%) improvement observed in closed loop total error, $\epsilon_{T_{CL}}$ over open loop total error, $\epsilon_{T_{CL}}$ using a simple I–controller (see Table 6.2). Since the driving frequency at 10 Hz is substantially lower than the control loop frequency of 250 Hz, the Type–II controller is able to substantially reduce hysteresis error and track the reference position closely for low frequency tracking control. When the same controller is applied for P_{2b} profile (125 Hz), large $\epsilon_{T_{CL}}$ is observed (Figure 6.4, Table 6.2). Even though the total errors shown in Table 6.2 are in the same order of magnitude for both the open and the closed loop condition, the sources of error are different. In the open loop condition, hysteresis is the main source of error; in the closed loop condition the error is mainly due to the phase lag introduced by the Type–I control system at high frequency. This can be confirmed from the controller error, $\epsilon_{C_{CL}}$ in Table 6.2 for 10 Hz and 125 Hz. The controller error, $\epsilon_{C_{CL}}$ is quite small in P_{2a} while in case of P_{2b} the controller error is quite high. However, the $\epsilon_{O_{CL}}$ is still in small (3%) and similar to the low frequency case (P_{2a}).

Figures 6.5(a) and 6.6(a) show the responses in open loop and closed loop conditions for profiles P_{2c} and P_{2d}, respectively. The profiles are selected so that multiple frequency components (10 Hz to 50 Hz in P_{2c} and 30 Hz to 100 Hz in P_{2d}) as well as the minor loops can be included in the tests. Similar to the fixed frequency results, the $\epsilon_{T_{CL}}$ increases at high frequencies. However, from Table 6.2, we can conclude that the HPO performance is not affected by the frequency changes even in the presence of mixed frequency cases (rate-dependency). The errors for P_{2c} and P_{2d} are shown in Figures 6.5(b) and 6.6(b), respectively.

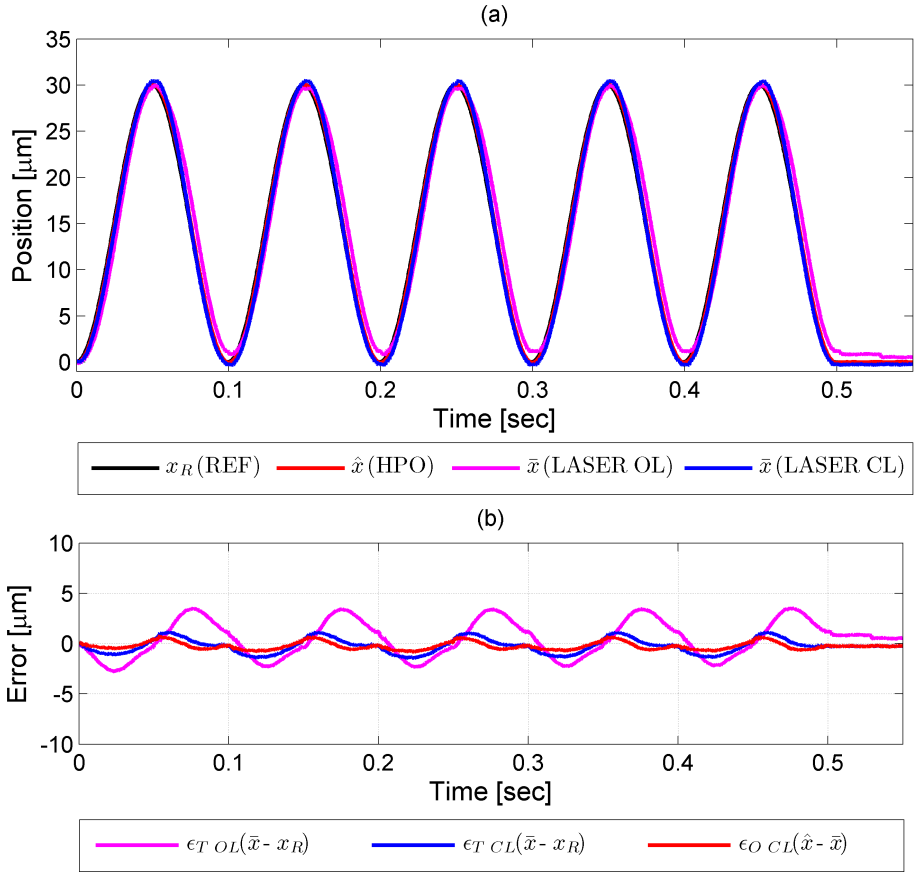

Figure 6.3: (a) P_{2a} (10 Hz) reference position, HPO position, measured open loop and closed loop position (b) Total error (Open loop and closed loop) and closed loop observer error ([88] ©2013 IEEE)

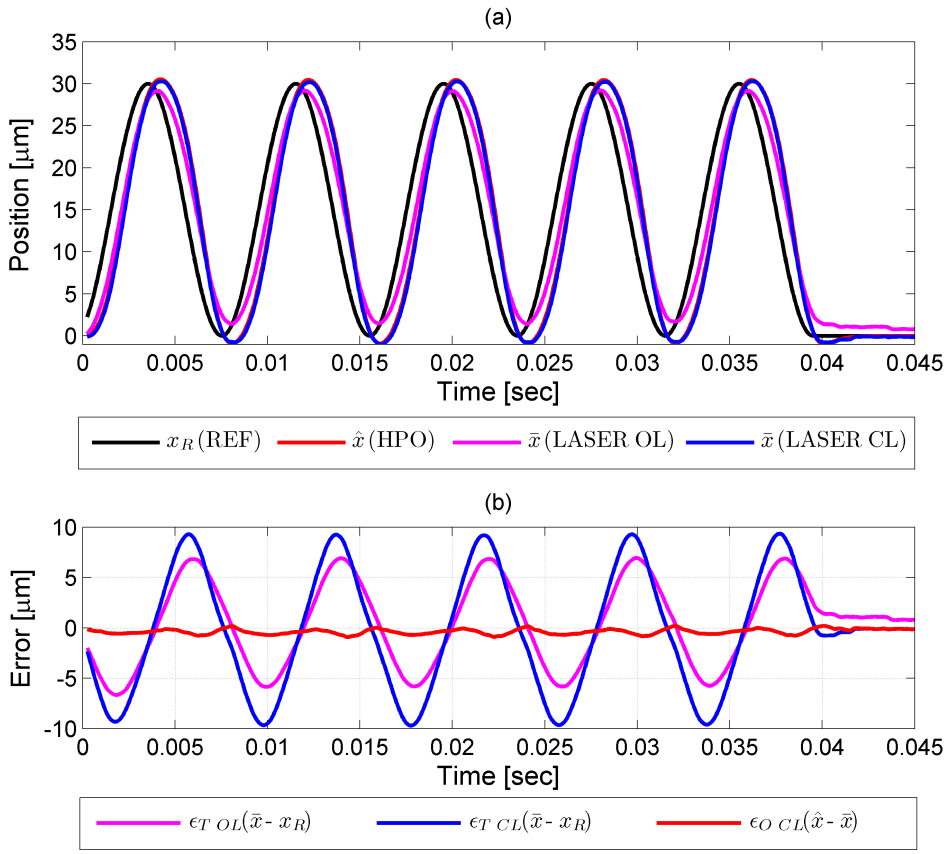

Figure 6.4: (a) P_{2b} (125 Hz) reference position, HPO position, measured open loop, and closed loop position (b) Total error (open loop and closed loop) and closed loop observer error ([88] ©2013 IEEE)

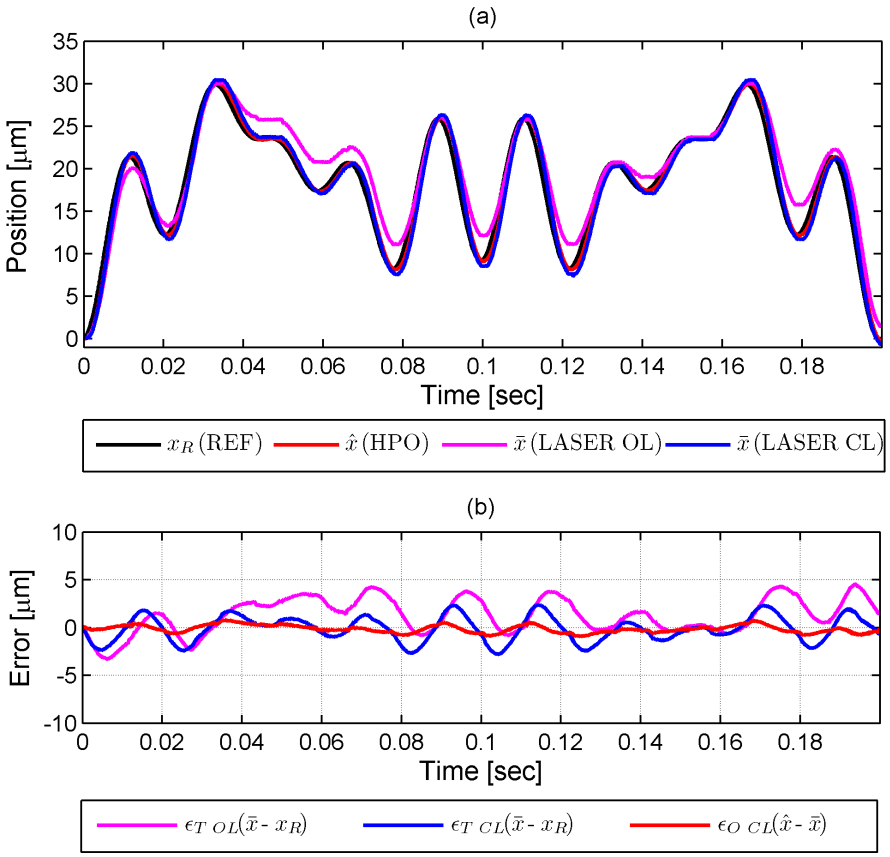

Figure 6.5: (a) P_{2c}) reference position, HPO position, measured open loop, and closed loop position (b) Total error (open loop and closed loop) and closed loop observer error ([88] ©2013 IEEE)

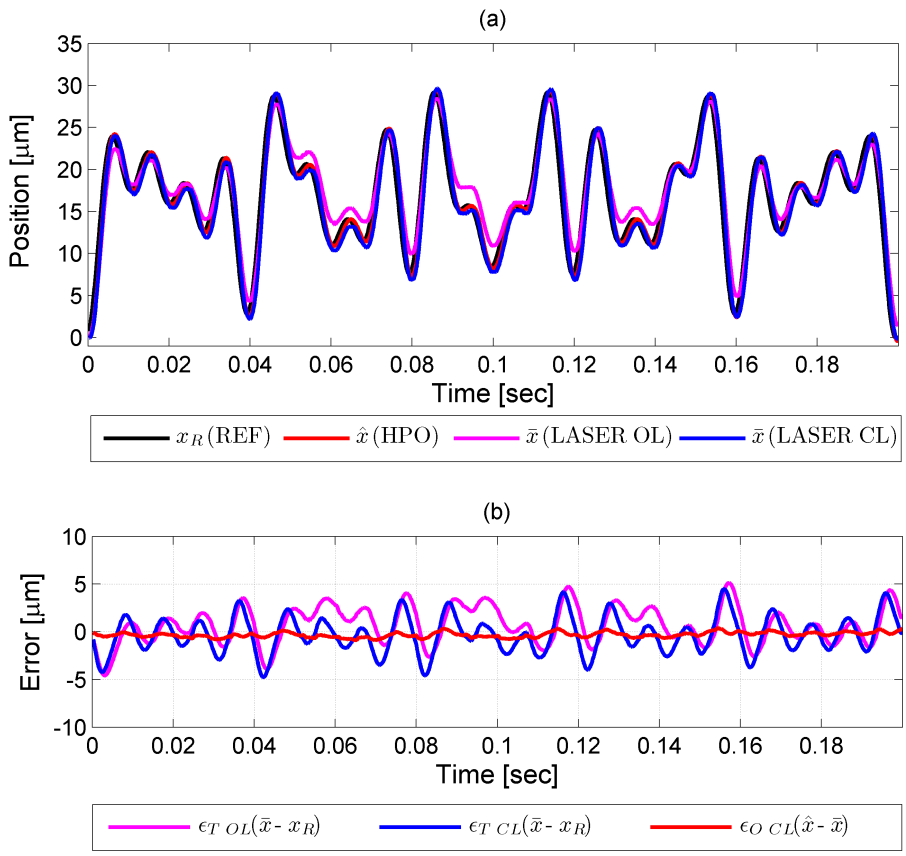

Figure 6.6: (a) P_{2d} reference position, HPO position, measured open loop, and closed loop position (b) Total error (open loop and closed loop) and closed loop observer error ([88] ©2013 IEEE)

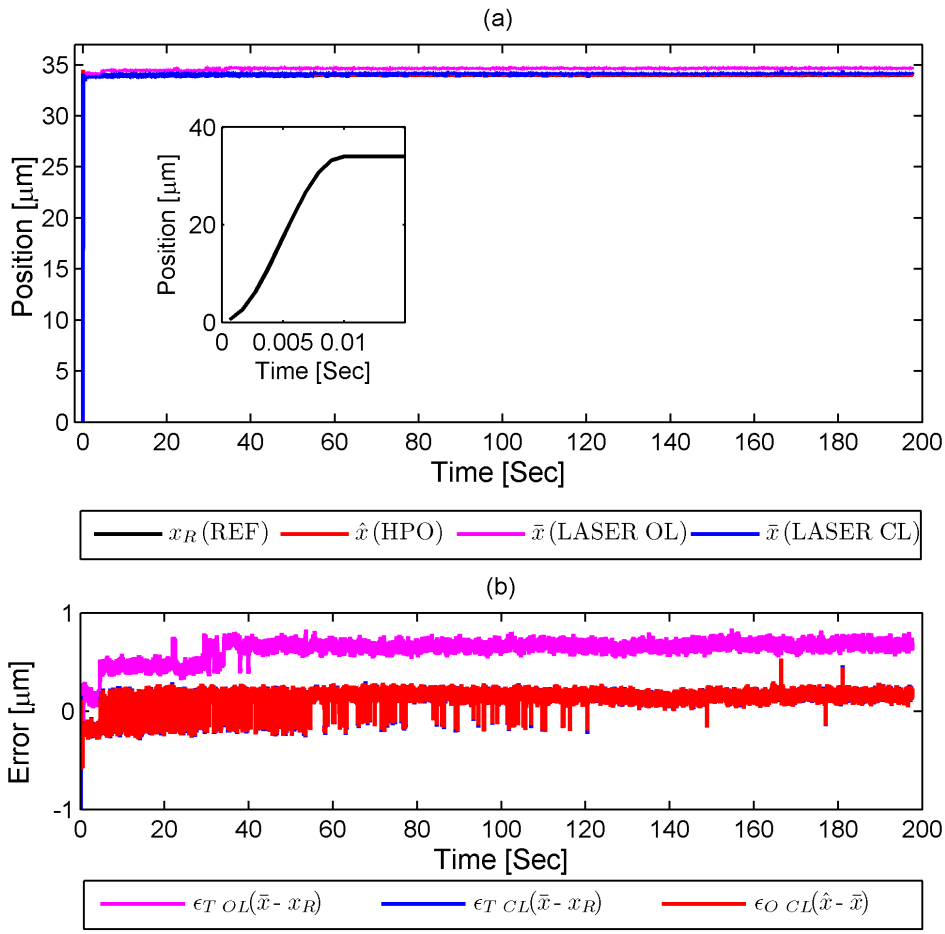

Figure 6.7: (a) P_3 reference position, HPO position, measured open loop, and closed loop position (b) Total error (open loop and closed loop) and closed loop observer error (Reprinted with permission [61]. Copyright 2012, American Institute of Physics.)

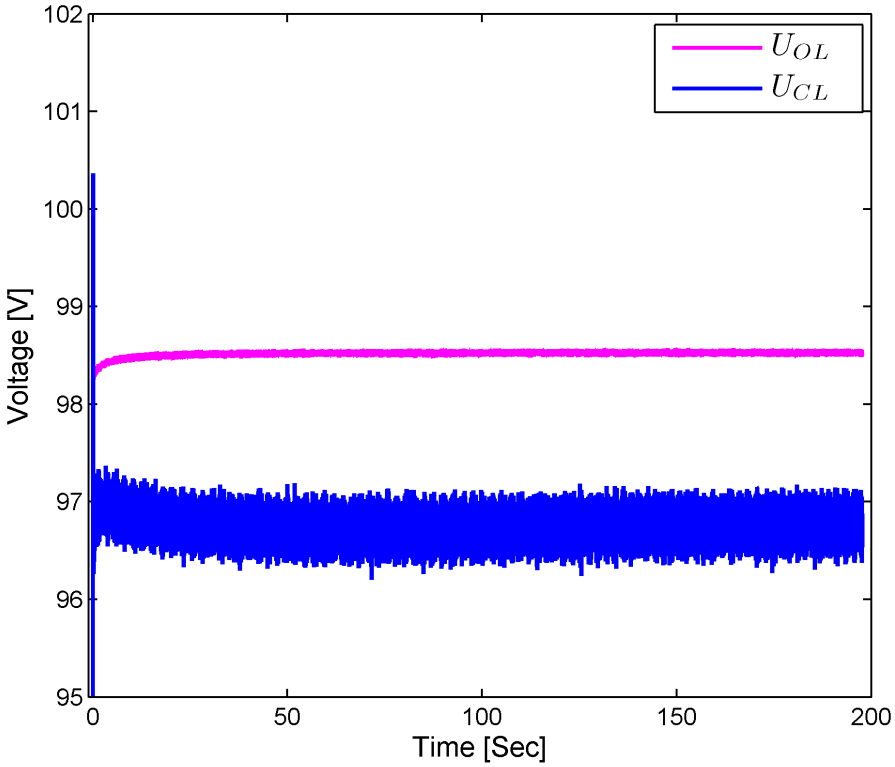

Figure 6.8: Voltage profiles in open loop and closed loop condition

6.2.3 DC Profile with Fast Transient Section, P_3

This profile is selected to compare the HPO performance in the presence of creep with a fast transient path. The transient part of the profile is a 50 Hz signal followed by a DC signal over 175 seconds. The results are shown in Figure 6.7. Although the amount of creep is not large in open loop condition (<1 μm), the improvement is visible in the error when the HPO feedback is introduced in closed loop control. In addition to that, the voltage signal is shown for both open loop and closed loop conditions in Figure 6.8. The voltage signal is increasing over time in the open loop while the controlled voltage in the closed loop is decreasing which tries to minimize the creep voltage and hence the position. The HPO error for profile P_3 is 0.53 μm.

6.3 Summary

In this chapter, the HPO is used as a feedback sensor to achieve sensorless feedback control. It is shown that the HPO feedback results in a maximum observer error of 3% of maximum scale when compared to a laser reference sensor over a very wide frequency range (DC to 125 Hz). There is a 58% improvement in low frequency tracking operation observed compared to open loop operation with the HPO feedback. The observer error does not increase with the frequency. However, the overall tracking error is increased due to the controller error (Table 6.2). The HPO performance compares well with other sensorless position control algorithms shown in the literature (in Section 1.9). Different profiles are selected to include the creep behavior, rate dependency and minor loops. However, since a Type–I control system was used, tracking error at frequencies approaching the bandwidth of the control loop are high. A feedforward controller could be added to the control system shown here in order improve tracking performance at higher frequencies. However, this would distract from the HPO performance and so it was opted not to include a feedforward term in the controller implementation shown here.

Chapter 7

Self-heat Generation

A large number of piezoelectric actuators are made of soft PZT materials which provide high piezoelectric coefficient, d. However, soft PZT material possesses a high dielectric loss factor, $\tan\delta$ [20]. For non-resonant applications such as in high speed positioning stages or high speed inkjet printing, it is reported that the total loss encountered is primarily due to dielectric loss [86]. In contrary, for resonant applications such as in ultrasonic cleaning, the total loss is related to the mechanical or elastic losses in the actuator [86]. Irrespective of the type of the application (resonant or non-resonant), during continuous operation, the total loss, due to dielectric loss or elastic loss, contributes to the temperature rise of the actuator [86]. This phenomenon is known as self-heat generation. The self-heating phenomenon for PEAs was first addressed in [21] where it is shown that under continuous high frequency and high voltage loading, significant heat generation is observed. In Chapter 5, it has been shown that the HPO is able to predict position over a frequency range of 0 Hz to 100 Hz. However, self-heat generation occurs already at 50 Hz operation if the actuator is continuously driven over a long period of time [85]. The temperature increase due to self-heat generation affects the capacitance of the piezoelectric actuator. This indicates that during continuous operation even at 50 Hz, the performance of the HPO may deteriorate since it uses capacitance based PSS. Hence, it is necessary to predict the temperature rise of the piezoelectric actuator due to self-heat generation. Also, the estimated temperature may be used to ensure that the actuator is not operated beyond the Curie temperature (150°), where it may lose piezoelectric properties.

In [21, 85], it is shown that the temperature rise due to self-heating in non-resonant applications is a function of driving frequency, f, electric field, E and effective volume to surface area ratio, $\frac{v_e}{A}$. A model to predict the self-heating

temperature is shown in Equation (7.1):

$$T - T_0 = \frac{u f v_e}{k_T A}\left(1 - e^{-\frac{k_T A}{v \rho c} t}\right), \tag{7.1}$$

where, u is the loss of the sample per driving cycle per unit volume, k_T is the overall heat transfer coefficient, ρ is the density of the PZT material, v is the actuator volume and t is the time [21]. The loss term u is obtained from the P-E hysteresis loop using a Sawyer-Tower circuit, whereas P is the polarization and E is the electric field. It is reported that the parameter, u is dependent on temperature variation. The term k_T accounts for the convection and radiation heat transfer. It is reported that k_T is constant for low electric fields and varies when exposed to high electric fields. In addition, the term k_T, slightly varies with temperature. The prescribed range of k_T is $20 - 40 W m^{-2} \cdot K^{-1}$. To summarize, the prediction of actuator temperature by using [21, 85] requires the knowledge of driving frequency, as well as parameters u and k_T that themselves are dependent on temperature.

The literatures found to date describe how to model the temperature increase due to self-heat generation where a hysteresis loss component and frequency is known. The limitations are: 1) the hysteresis loss component itself is a temperature dependent parameter, 2) the models require the exact knowledge of frequency which limits the model to predict the temperature for mixed frequency operation, and 3) the term k_T is a function of electric field and driving frequency. In this chapter, self-heat generation is modeled in piezoelectric actuators using the constitutive relationship of first law of thermodynamics and power loss due to hysteresis voltage in the actuator. The model does not require any known frequency and hence should be independent of the type of the profile and knowledge of frequency. However, since the constitutive equations are used in the model, position signal is required as an input to the model. It should be noted that self-heating of non-resonant operations of the PEAs is considered only, since the actuators usually operate at frequencies lower than the first mechanical resonant frequency. This leads to the assumption that the dielectric losses are the main contributor to the total losses which result in self-heat generation.

This chapter is organized as follows. In Section 7.1, a self-heat generation model that requires voltage, current, as well as position is presented to estimate the temperature. Experiments to characterize the temperature behavior are shown in Section 7.2. The parameter identification of the model is presented in Section 7.3. Experimental results, showing temperature estimates using a dedicated position sensor input are shown in Section 7.4. To obtain a sensorless (eliminating position sensor) temperature prediction, a temperature compensated HPO and temperature model is shown in Section 7.5. Finally, the combination of temperature compensated HPO and the new temperature model are validated in Section 7.6.

7.1 Proposed Model

The self-heat generation model proposed in this chapter is based on the law of energy conservation of a closed system presented in [21]:

$$\dot{q}_G - \dot{q}_D = \rho c v \frac{dT}{dt} \tag{7.2}$$

where, $\dot{q}_G$ is the rate of heat generation, $\dot{q}_D$ is the rate of heat dissipation, ρ, c and v are the density, specific heat and total volume of the actuator, respectively. It is assumed that the system is in perfect insulation. For non-resonant applications, it is reported that the dielectric loss is equivalent to the hysteresis loss and hence, is the major contributor of heat generation [20, 21, 85, 86]. Therefore, Equation (7.2) can be rewritten as follows:

$$P_{Loss} - k_T A \triangle T = U_H I - k_T A \triangle T = \rho c v \frac{dT}{dt}, \tag{7.3}$$

where, P_{Loss} is the power loss due to hysteresis loss, k_T is the overall heat transfer coefficient, ΔT is the temperature difference between the actuator and the environment due to self-heating and A is the surface area of the actuator. The overall heat transfer coefficient considers the heat conduction, convection and radiation [21]. The term U_H is the hysteresis voltage in [13] and I is the current.

The transfer function between P_{Loss} and ΔT is shown in Equation 7.4:

$$\Delta T = \frac{P_{Loss} \cdot \gamma}{s \cdot \tau + 1} \tag{7.4}$$

where,

$$\tau = \frac{\rho v c}{k_T A}, \tag{7.5}$$

$$\gamma = \frac{1}{k_T A}, \tag{7.6}$$

$$P_{Loss} = U_H I. \tag{7.7}$$

7.2 Experimental Approach

The experimental setup discussed in Chapter 2 is used for the self-heating experiments. The actuator surface temperature is measured using a non-contact infrared sensor (Micro-epsilon thermometer CT-CF15) to avoid friction between the sensor and the actuator. For the current measurement, a high resolution current probe (TEKTRONIX-TCP312) is used. A high frequency laser vibrometer (POLYTEC-HSV2002) is employed to measure the position of the actuator. The test-bed is shown in Figure 2.3.

Figure 7.1 shows the time responses of the actuator temperature when step changes in frequency are applied. Operating at less than 20 Hz results in negligible self-heating while beyond 200 Hz, resonant vibrations start to become noticeable, since the first natural frequency of the test-bed is 2500 Hz. To obtain maximum temperature rise, a sinusoidal unipolar voltage of 100 V, which is equivalent to 1.8 kV mm^{-1}, is applied to the actuator. The actuators are operated for more than 400 seconds to reach the steady-state temperature. Figure 7.1 shows that the time constant is independent of the applied frequency, but the steady-state value of the final temperature increases with frequency. Figure 7.2 shows that there is a linear relationship between the steady-state temperature and the driving frequency. This is consistent with [20, 21, 83]. In agreement with [21, 83], it is also observed in Figure 7.3 that the change in temperature

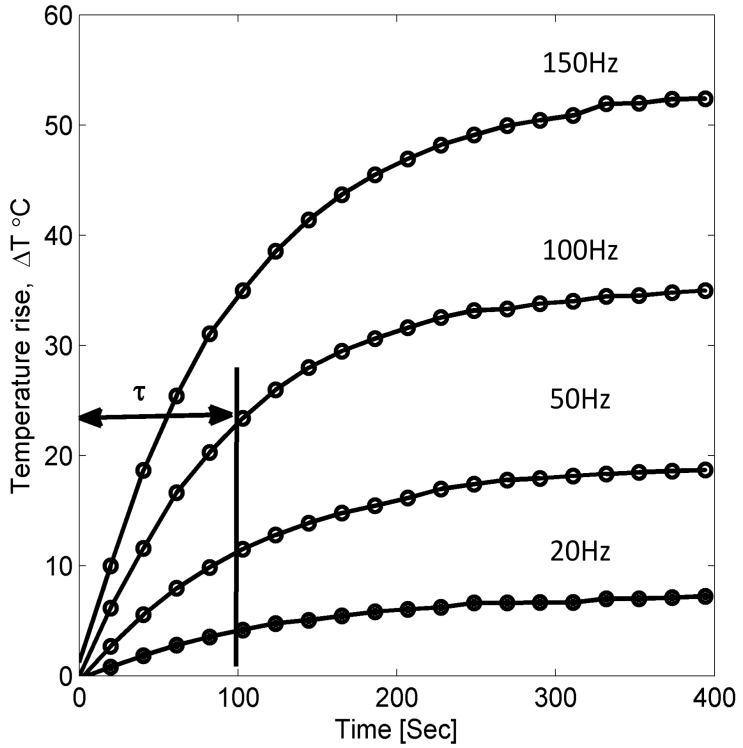

Figure 7.1: Effect of frequencies on self-heat generation. It is important to note that the frequencies are high enough to result in self-heat generation. However, the frequencies are still well below the resonant frequency (see Figure 1.4) of the test-bed and hence a quasi-static approximation is still valid.

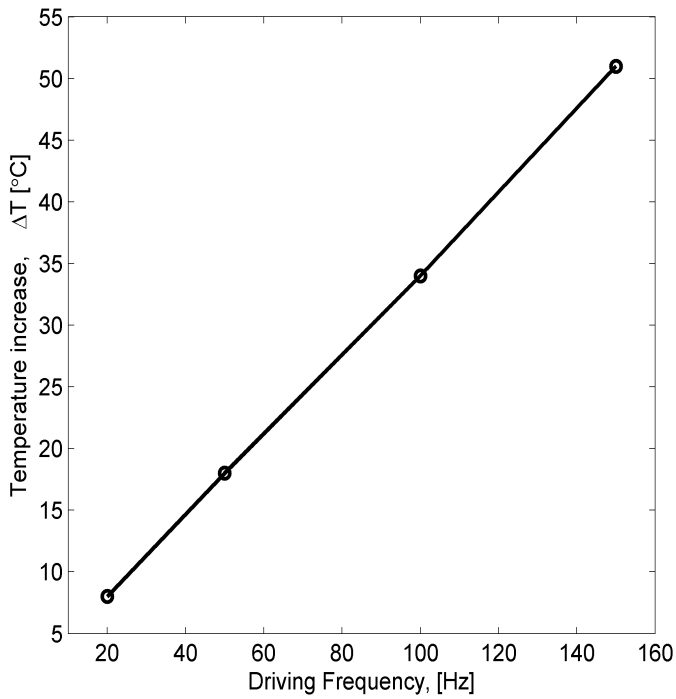

Figure 7.2: Change in steady-state temperature increase with driving frequency (at 100 V sinusoidal signal)

is related to the square of the applied voltage. The temperature increase is not substantial when the driving voltage is less than 50 V at 150 Hz.

7.3 Parameter Identification

The model presented in Section 7.1 requires two parameters to be identified: τ and γ. The time constant, τ is 100 seconds for the frequency ranges from 20 Hz to 150 Hz obtained from Figure 7.1. The value of overall heat transfer coefficient, k_T can be attained from Equation 7.5. Using the values of total surface area, A and k_T, the second model parameter, γ, is obtained from Equation 7.6. The term U_H, in Equation 7.7 can be obtained from the piezoelectric constitutive equations proposed by Goldfarb et al. in [13]. The constitutive force equation

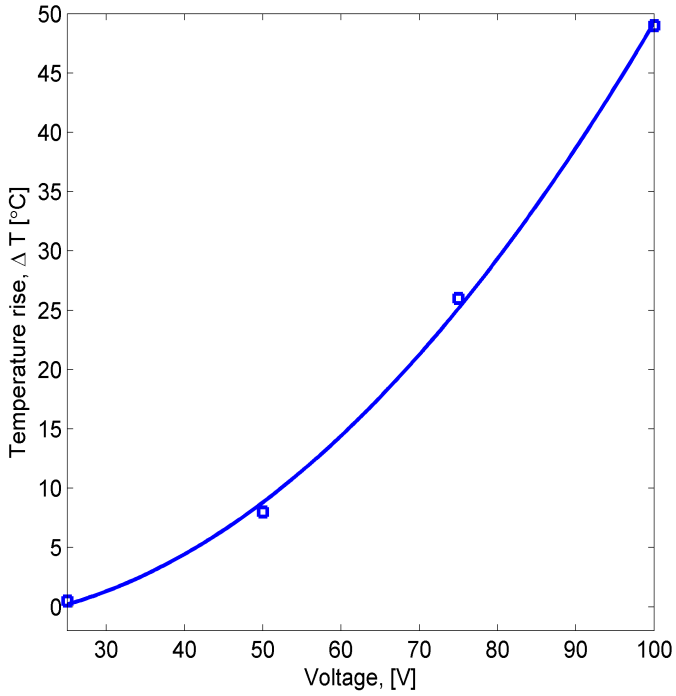

Figure 7.3: Change in temperature increase with driving voltage (at 150 Hz)

at quasi-static region and the expression for hysteresis voltage is recalled from Equations 4.3 and 4.8 as follows:

$$kx = \alpha U_P \tag{7.8}$$

$$U_H = U - U_P \tag{7.9}$$

where, k is the stack stiffness, α is the force-voltage proportionality constant, and U_P is the linear piezoelectric voltage. Using Equations (7.7), (7.8) and (7.9) the following function can be obtained for power loss due to hysteresis:

$$P_{Loss} = (U - \frac{k}{\alpha}x)I \tag{7.10}$$

where, x is the measured position of the actuator. At maximum supply voltage, U_{max}, and maximum displacement, x_{max}, the term $\frac{k}{\alpha}$ can be attained from Equation (7.11):

$$\frac{k}{\alpha} = \frac{U_{max}}{x_{max}}. \tag{7.11}$$

It is important to note that although self-heat generation occurs at high frequency operations, the range of frequency is still below than the dynamic range mentioned in Figure 1.2. Hence, the quasi-static approximation is still valid for the frequency range where self-heating phenomenon occurs. The final model for self-heating is shown in Equation 7.12 where T_{Ref} is the reference temperature. The flowchart is shown in Figure 7.4.

$$T_{SH} = T_{Ref} + \frac{(U - \frac{k}{\alpha}x)I \cdot \gamma}{\tau \cdot s + 1} \tag{7.12}$$

The properties of the PZT material are summarized in Table 2.1 and the self-heating model parameters are shown in Table 7.1. The parameters are obtained by fitting the experimental results shown in Figure 7.1 and Equations 7.5 and 7.6. The ratio of $\frac{k}{\alpha}$ is considered unaffected since the maximum stroke is unaffected due to temperature variation in the setup. The value of the overall heat transfer coefficient, k_T compares well with the prescribed values in [21].

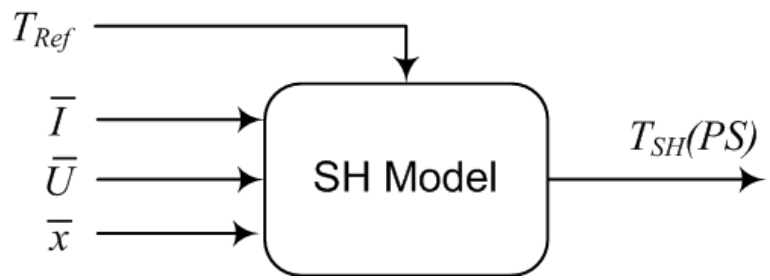

Figure 7.4: Self-heat generation model with position sensor input

Table 7.1: Self-heating model parameters

Parameters	Values
Time constant, τ	100 sec.
Overall heat transfer coefficient, k_T	$28\ W \cdot m^{-2} \cdot K^{-1}$
γ	$57\ W \cdot K^{-1}$
Stiffness to coupling coeff. ratio, $\frac{k}{\alpha}$	2.85 e6 $V \cdot m^{-1}$
Ambient temperature, T_{Ref}	$23°C$

7.4 Temperature Prediction Using a Dedicated Position Sensor

Once the model parameters are identified, real-time measurements of current, voltage and position provide an accurate measurement of temperature rise of the actuator due to self-heating. The experimental results and the predicted temperatures (from the model) for various driving frequencies are plotted in Figure 7.5. Both the temperature rise and fall can be predicted using the proposed self-heating model. For recording the temperature fall, the actuator is driven at 150 Hz-50 V, 10 Hz-100 V and 0 Hz-0 V. In another experiment, the actuator is driven by a combination of voltages and frequencies to observe the performance of the model under complex operating conditions. The results are shown in Figure 7.6. The prediction error is within ±2° which is less than 3% of the maximum temperature rise due to self-heating at 150 Hz-100 V.

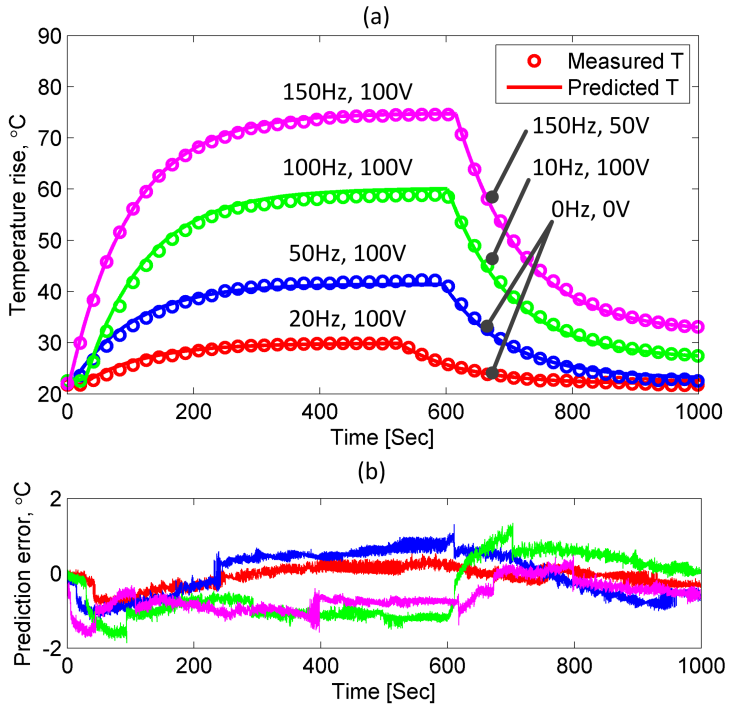

Figure 7.5: (a) Self-heat generation at different frequencies: measured and predicted temperature (b) prediction error

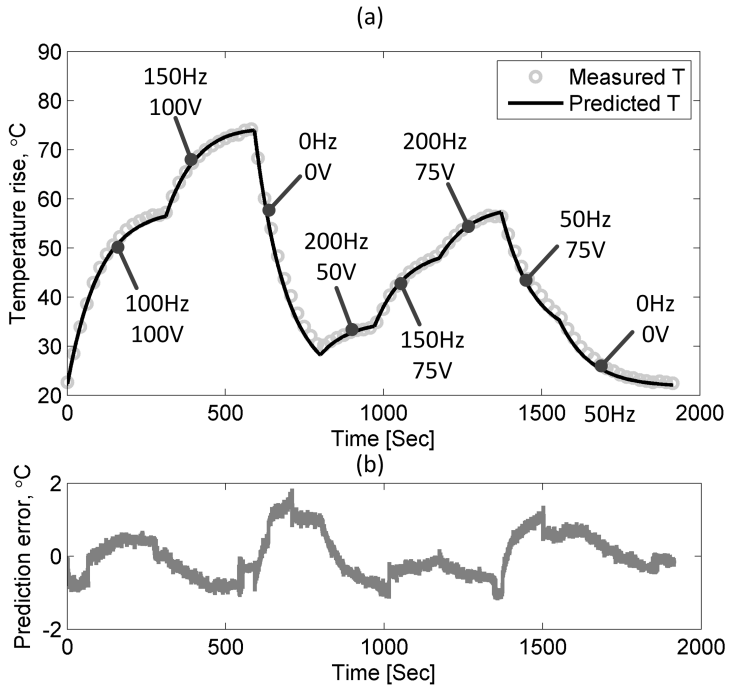

Figure 7.6: (a) Temperature profile using self-heating by driving at different frequencies and voltages: measured and predicted temperature (b) Prediction error

7.5 Temperature Compensation of HPO

In Section 7.3, a self-heat generation model is proposed which predicts the temperature increase due to self-heating based on driving current, driving voltage and a position measurement. This limits the model to a system where a dedicated position measurement is available. In this section, the HPO presented in Chapter 5 will be employed as a position input to the self-heat generation model to obtain a pure self-sensing temperature and position estimation.

Before employing the HPO signal as an input to the self-heating model, the effect of temperature on the capacitance based PSS needs to be evaluated. Figure 7.7 (a), shows the effect of temperature variation on the capacitance-position relationship. The capacitance increases with temperature increase while the position is unaffected at least for the investigated temperature range (upto 60°C). Figure 7.7(b) shows the corresponding capacitance-time relationships. It is observed that temperature creates an offset in the capacitance measurements. The size of the offset is linearly related to temperature. This offset in the capacitance-position relationship is expected to affect the HPO estimation. Since the self-heating phenomenon is dependent on frequency of operation, the effect of frequency on the capacitance-position relationship is also shown in Figure 7.8. Only small variation in the charge-position relationship is observed due to frequency variation.

From Figure 7.7, it is evident that a new fitting function is required to define the capacitance-position relationship with temperature variation to obtain a reasonable estimate of position from the capacitance based PSS. The new fitting function, Γ_T is presented in Equation 7.13 which requires a temperature input to predict the position from capacitance measurement in the presence of temperature variation:

$$\Gamma_T = \hat{x}_{C_P}(C_P, T) = b_{T0} + \sum_{n=1}^{N} b_{Tn}\bar{C}_P^n + g\hat{T}, \tag{7.13}$$

where, b_{T0} is the intercept, b_{Tn} is the expression for coefficients for capacitance and g is the temperature coefficient. The coefficients are obtained through a re-

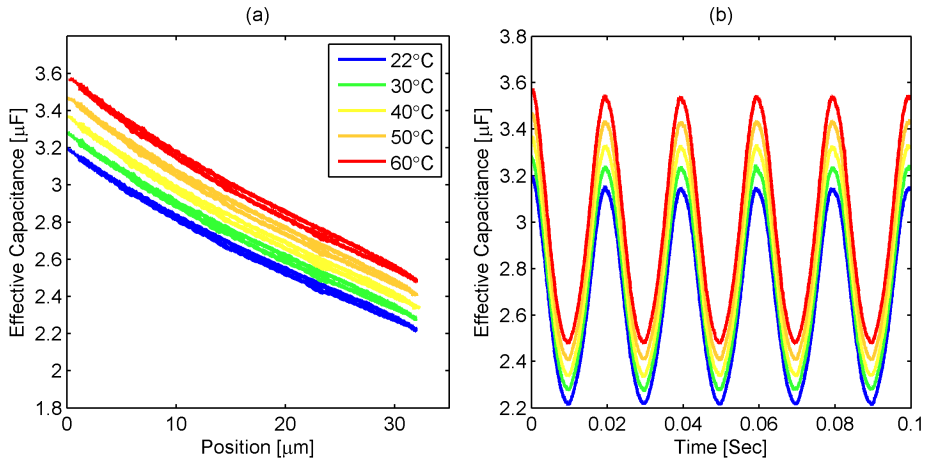

Figure 7.7: Effect of temperature on (a) capacitance-position relationship (b) capacitance measurement at 50Hz

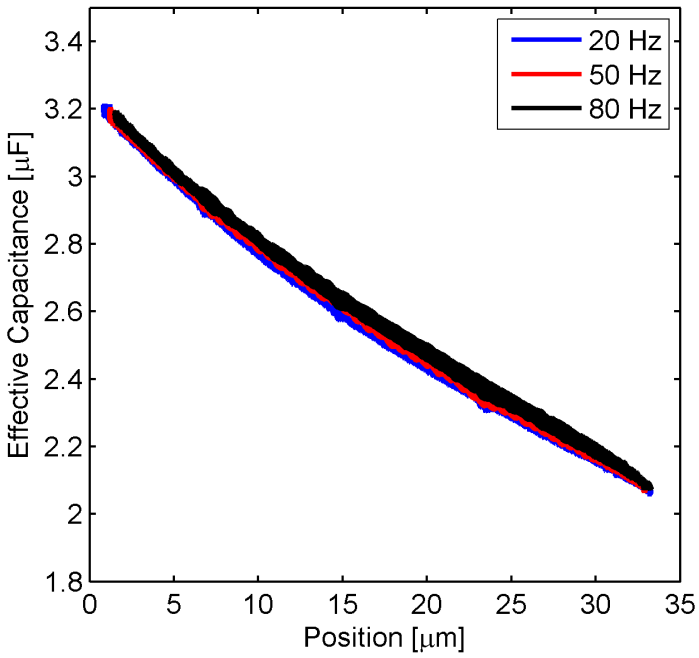

Figure 7.8: Effect of frequency on capacitance-position relationship

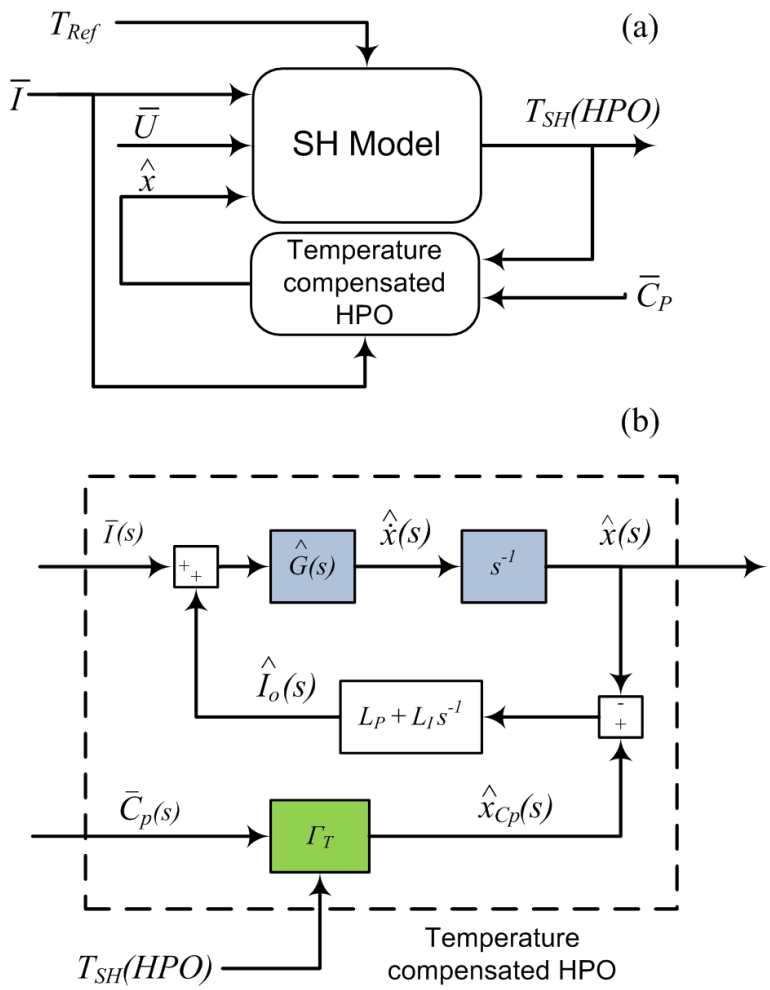

Figure 7.9: (a) Self-heat generation model with HPO input (b) temperature compensated HPO

gression analysis. The orders are selected by comparing the adjusted R^2 value which indicates that an order more than 5 would not improve the adjusted R^2 value (Table 7.2). Also, an interaction between capacitance and temperature does not have any effect on adjusted R^2 value. In addition to that, the p-value for the interaction is quite high (0.33) which indicates that the coefficient for interaction is redundant. The model is obtained based on 50 Hz data. The comparison is shown in Table 7.2.

Table 7.2: Comparison of the regression statistics

	n=4	n=5	n=6	n=5 with C_P and T interaction
Regression Statistics				
R Square	0.998189	0.998194	0.998194	0.998193
Adjusted R Square	0.998188	0.998193	0.998193	0.998193
Standard Error	0.474422	0.473808	0.47377	0.473825

An updated HPO structure is shown in Figure 7.8 which includes temperature compensation using the self-heat generation model (from Equation 7.13). The compensated HPO output is fed back to the self-heat generation model. This feedback mechanism between the HPO and the temperature model works quite well, because the temperature variation is relatively slow in comparison to the piezoelectric position changes.

7.6 Temperature and Position Predictions Using the HPO and the Self-Heating Model

A sensorless temperature prediction due to self-heating was presented in Section 7.5 where the temperature compensated HPO is employed as an input to the self-heating model to estimate the position of the actuator. In this section, experiments are carried out to validate temperature and position predictions using the HPO as the position input to the temperature model. To distinguish between the two position inputs to the temperature model, $T_{SH}(PS)$ is used to define the self-heating model using the laser position input while $T_{SH}(HPO)$ is

Table 7.3: ANOVA table for capacitance based PSS regression model with temperature

ANOVA for n=5					
	df	SS	MS	F	Significance F
Regression	6	992110.4	165351.7	1096054	0
Residual	7993	1205.832	0.150861		
Total	7999	993316.2			

	Coefficients	t Stat	p-value
b_{T0}	-870.776	-7.50918	0
b_{T1}	1639.54	7.873573	0
b_{T2}	-1132.54	-7.61792	0
b_{T3}	376.6851	7.140752	0
b_{T4}	-61.8409	-6.64742	0
b_{T5}	4.036799	6.187723	0
g	0.263115	860.7364	0

used to denote the self-heating model that uses temperature compensated HPO position input.

In Figures 7.10 and 7.11, 100 Hz and 50 Hz self-heating temperature predictions are shown for both $T_{SH}(PS)$ and $T_{SH}(HPO)$. The measurements are compared with the infrared sensor and found to agree within less than 2°. In Figure 7.12, a mixed frequency case is tested where temperature cycling is obtained with a combination of frequencies to heat up and cool down the actuator. Heating up is achieved through a series of sections ('a'–'c') with increasing frequencies (20 Hz–50 Hz–100 Hz). This sequence of driving frequencies leads to a final temperature larger than 50°C. To cool the actuators back down, driving frequencies of 50 Hz and 0 Hz ('d' and 'e') are used. The HPO position compares well with the laser sensor position in Figure 7.13 (a). The laser vibrometer has some drift in long term measurements which is visible in sections ('a' and 'd') in the profile. Although the contact between the needle and the PEA is very small (hence most of the heat is assumed to be transferred through convection and conduction is neglected), combined effect of expansion of the needle and contraction of the piezoelectric actuator due to temperature increase may con-

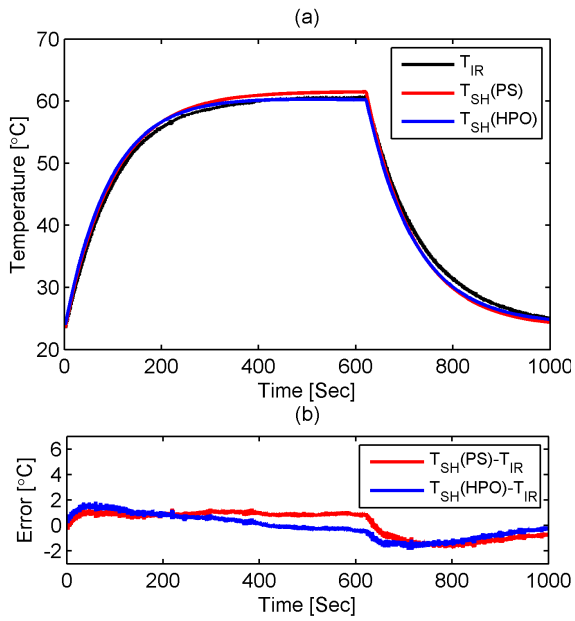

Figure 7.10: (a) Temperature prediction by self-heat generation model (b) errors in prediction at 100 Hz

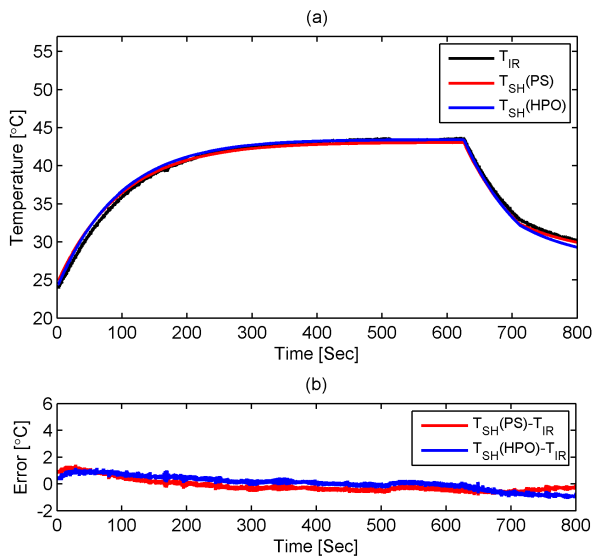

Figure 7.11: (a) Temperature prediction by self-heat generation model (b) errors in prediction at 50 Hz

tribute to this drift. However, it is interesting to see that at the maximum temperature region (section 'c'), the laser measurement does not show any drift while in section 'd' (temperature decreasing), a maximum drift of 0.6 μm is observed. Further, careful investigation including the temperature distribution in the needle assembly and actuator is required to conclude on thermal expansion of the PEA and the needle assembly; however, this is not included in the scope of this study.

The HPO position also shows some changes at the beginning of frequency switches (beginning of different sections). This is attributed to the change in the unmodeled capacitance frequency dependency shown in Figure 7.12. The HPO output is used in the self-heating model to predict the temperature and which in turn is feed back to the HPO to compensate the temperature. This circular feedback is possible due to the slow temperature variation in comparison to the position change of the actuator. Considering the presence of laser drift and HPO error due to frequency changes, the maximum observer error is recorded at 1.38 μm (4.18% of the maximum stroke) in Figure 7.12(c) over the frequency range of 0 Hz to 100 Hz and a temperature change of up to 55°C. To the best knowledge of the author, this is the first time in scientific literature that a successful position estimation algorithm has been presented for a wide range of frequencies and operating temperatures. The HPO output is used in the self-heating model to predict the temperature and which in turn is feed back to the HPO to compensate the temperature. This circular feedback is possible due to the slow temperature variation in comparison to the position change of the actuator. The errors in temperature prediction from the two different position sources (position sensor and HPO) are compared in Figure 7.12 (d). In some portions, $T_{SH}(PS)$, which uses the laser position measurement, provides slightly better temperature predictions than the HPO based values of $T_{SH}(HPO)$. However, the maximum error is recorded 1.45°C in both the cases.

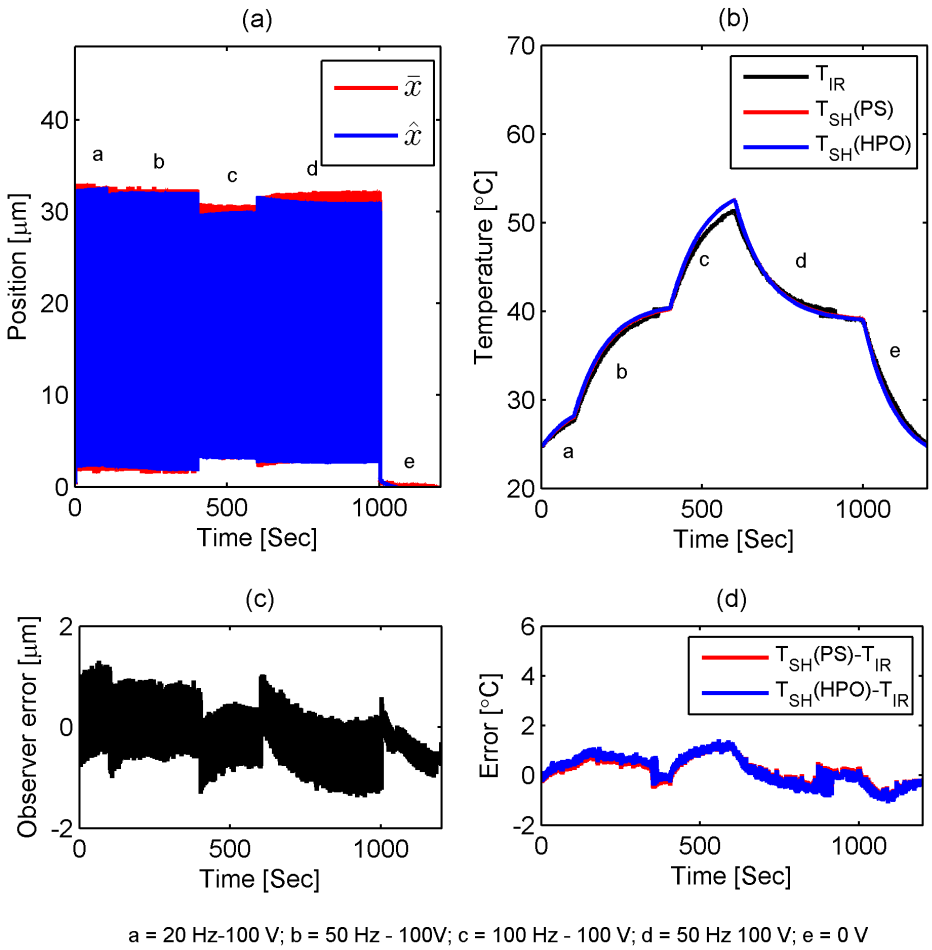

Figure 7.12: (a) Position measurements (HPO and sensor), (b) Self-heating at mixed frequency cases, (c) error in HPO, and (d) errors in temperature prediction

7.7 Summary

A novel sensorless temperature measurement is presented in this chapter which is based on power loss due to self-heating and the piezoelectric constitutive relationship. The advantage of the proposed model is that it does not require the knowledge of the driving frequency in contrast to the earlier developed models. Moreover, the new method is much simpler than the models in [21, 85], which require the term energy loss per cycle per volume, u and the overall heat transfer coefficient, k_T which are functions of the electric field and temperature. The proposed model is tested in fixed and mixed frequency cases and compared with a traditional temperature sensor. The temperature prediction is accurate with in ±2°C which is close to 3% of the investigated range. When the HPO is updated to include temperature dependencies and combined with the new model, sensorless temperature and position estimation is obtained in the presence of self-heating. This provides a maximum position error of 4.18% over the frequency range of 0 Hz to 100 Hz and up to $55°C$ of temperature increase due to self-heat generation.

Chapter 8

Conclusions and Future Research

The foremost objective of this dissertation is to develop a PSS technique for position feedback control in PEA over a wide frequency range where creep and rate-dependent hysteresis lead to large errors in traditional feedforward positioning systems. In addition to that, a self-heat generation model is developed and temperature compensation of the position self-sensing scheme is proposed in this research. The research outcome can be extended to different applications some of which are outlined in the future research section.

8.1 Conclusions

The research findings are based on a novel real-time piezoelectric impedance measurement algorithm which facilitates the parameter identification of the electromechanical models. The measurement technique superimposes a high frequency voltage ripple onto the normal driving voltage and extracts impedance of PEA from the relationship between voltage and current ripples. Since the measurement frequency is very high in comparison to the natural frequency of the test bed, the measurement is obtained in a clamped condition. This leads to a relationship between capacitance and position where the hysteresis is negligible (<3%). The capacitance value decreases with the actuator displacement. This finding leads to two major conclusions: 1) the capacitance in the electromechanical model is not constant, and 2) the capacitance-position relationship provides a means for position self-sensing through a regression model. The first conclusion indicates that an improved electromechanical model is required to include the position dependent capacitance. The proposed modeled is verified experimentally and compared with the traditional model. Based on the updated electromechanical model, a novel parameter identification technique is

proposed where a single set of experiments provide all the required parameters in the model. In addition to that, some important material parameters such as piezoelectric strain coefficient, coupling coefficient, and permittivity constant are also obtained through constitutive relationships. These values compare well with the manufacturers specified values.

The second conclusion of the capacitance-position relationship (through regression model) promotes a self-sensing technique applicable to slow operations where creep and hysteresis are present. By combining this capacitance based PSS technique with conventional charge based PSS, using a novel hybrid position observer, position is estimated over an extended frequency range where creep and rate dependent hysteresis are prominent. This is achieved by exploiting the advantages of each technique where the hysteresis free charge based PSS provides the position estimate at high frequencies (lower than the dynamic range) while the capacitance based PSS (Γ) is employed at slow operations. The major problem with the charge based PSS is the drift in position estimation due to offset currents in the charge measurement. The capacitance based measurement then serves two purposes: 1) to provide a PSS signal at low frequency operation where charge is difficult to measure, 2) to eliminate offset currents in the charge based PSS. The performance of the position observer is compared with a traditional position sensor. The comparison shows that position observer is able to predict the position from static operations up to 100 Hz with an error close to 3% of full scale.

The developed HPO is then tested in a controlled environment with different waveforms from variable lift step profiles to mixed frequency sinusoidal profiles. The creep profile is also tested in conjunction with a fast transient section. A simple Integral-controller is implemented to observe the performance. Similar to the open loop conditions, the HPO is compared to a reference sensor and the error is recorded at around 3% of full scale. Even though the HPO error is fairly constant at all frequencies, the overall controller error increases at higher frequencies, since a simple Type-I controller was used in the experiments. In the future, other control schemes like Type-II controllers or feedforward/feedback controllers presented in the literature may be implemented to reduce the controller error at higher frequencies. Self-heating phenomena are

observed in piezoelectric actuators when operated at relatively high frequencies over an extended period of time. The frequency range, over which the HPO is proposed, is high enough to generate heat due to self-heating when continuously operated. The temperature of the actuator may increase up to 60°C at 100 Hz driving frequency. The temperature rise may have several effects: 1) the life of the actuator is reduced if continued over an extended period of time, 2) the stroke of the actuator may be affected, and 3) the position self-sensing scheme may be affected. A self-heat generation model is proposed based on the power loss of the piezoelectric actuator that relies on the electromechanical model of the actuator. The advantages of the model are: 1) unlike the other self-heating models, it does not require a known frequency of operation which makes the model applicable for different profiles, and 2) it is based on the power loss of the actuator over time due to self-heating and not dependent on other temperature dependent parameters such as overall heat transfer coefficient and hysteresis loss per unit volume. Since, self-heating is a function of voltage, frequency and length of actuation, the experiments to validate this model contain multiple frequencies and voltage magnitudes. Since the temperature model requires driving voltage, driving current, and measured position as its inputs, the model is tested both with a laser position measurement, and a temperature compensated HPO as the position input. The temperature prediction error is less than 2°C for both position sensor input and HPO input to the self-heat generation model which is close to 3% of the maximum investigated scale. The errors position estimates obtained with the combined HPO and temperature model is less than 5%.

The major goals in this research are met with experimental validations. The following contributions are significant in this research:

- A novel impedance measurement algorithm is proposed which provides real-time clamped capacitance and resistance measurement for piezoelectric actuators.

- An improved electromechanical model and parameter identification is proposed based on the real-time capacitance measurement.

- A novel hybrid position observer is presented which relies upon two self-sensing techniques to provide improved position information over an ex-

tended frequency range where creep and rate-dependent hysteresis are present. The HPO is helpful for sensorless position control in piezoelectric actuators.

- A self-heat generation model is presented which predicts the temperature rise in the piezoelectric actuator due to self-heat generation.
- A novel sensorless temperature and position estimation technique is presented based on temperature compensated HPO to predict self-heating temperature variation.

8.2 Future Research

Some of the future research possibilities are outlined as follows:

- The real-time impedance measurement presented in this thesis provides capacitance and resistance measurements for piezoelectric actuators. The impedance measurement is obtained at constant loading condition where force changes are negligible. In future research, the effect of preloading or external load variation should be investigated.
- During the work on this thesis it is observed, that capacitance and resistance values of new actuators stabilize over the first several thousand cycles of use. Even though no measurable changes are observed after this initial break in period during the work on this thesis, it is expected that over the life of the actuator changes will take place. This may result due to failing of the piezoelectric layers, or cracks developing in the actuator. Hence, by comparing the capacitance/resistance measurement, a health monitoring strategy can be developed for the piezoelectric actuator.
- The HPO is tested in closed loop condition with a Type-I controller where the reference tracking performance is poor for high frequency profiles. It has been shown in the literature that a feedforward branch is often used to improve the dynamic performance of the feedback controller. However, most of the control systems are based on a dedicated position sensor. The proposed HPO can be used as a replacement of the traditional

sensor where a simple hysteresis model can be included in the feedforward branch of the controller to improve the tracking performance.

- When the HPO is updated for the self-heat generation cases, a good estimate for piezoelectric actuator positioning is obtained. In further investigations, the HPO should be tested over a wide temperature range specially from subzero condition to high temperature range up to 100°C. This study will be helpful to implement the HPO in applications such as piezoelectric fuel injectors.

- Piezoelectric paint sensors (PPS) [105, 106] are a relatively new technology to obtain structural health monitoring for large infrastructures such as bridges, buildings, etc. The main advantage of the paint sensor is that it can be used on different surfaces where traditional strain sensors cannot be mounted easily. The impedance measurement of the PPS may provide a relationship between the capacitance and crack related strains which can be used for structural crack monitoring in large structures. Often traditional strain sensors are equipped with temperature sensors which correct the temperature related changes in the sensor signal. The proposed impedance/resistance measurement can be used to correct the temperature related error in the impedance/capacitance measurement to monitor the crack growth.

- Piezoelectric micro-cantilever beams are used to detect the mass of biomarkers through the shift in the natural frequency of the beam [107]. The newly developed impedance measurement can be helpful to identify the temperature of the biomarker in addition to the mass. This can be helpful to detect cancer cells which have higher temperatures than other cells due to rapid replication of the cells.

Bibliography

[1] T. Ikeda, *Fundamentals of Piezoelectricity*. New York, USA: Oxford University Press, 1996. → pages 2

[2] J. Yang, *An introduction to the theory of piezoelectricity*. Springer, 2004. → pages 2

[3] R. Guo, L. E. Cross, S. E. Park, B. Noheda, D. E. Cox, and G. Shirane, "Origin of the high piezoelectric response in $pbzr_{1-x}ti_xo_3$," *Physical Review Letters*, vol. 84, no. 23, pp. 5423–5426, 2000. → pages 3

[4] I. Patel, *Advances in Ceramics - Electric and Magnetic Ceramics, Bioceramics, Ceramics and Environment*. InTech, 2011. → pages 3, 4

[5] J. e. Huber, N. a. Fleck, C. M. Landis, and R. M. McMeeking, "A constitutive model for ferroelectric polycrystals," *Journal of the Mechanics and Physics of Solids*, vol. 47, no. 8, pp. 1663–1697, 1999. → pages 3

[6] G. Ballas, Rudiger, *Piezoelectric multilayer beam bending actuators: static and dynamic behavior and aspects of sensor integration*. Springer, 2007. → pages 4

[7] L. Gaul and J. Becker, "Model-based piezoelectric hysteresis and creep compensation for highly-dynamic feedforward rest-to-rest motion control of piezoelectrically actuated flexible structures," *International Journal of Engineering Science*, vol. 47, no. 11-12, pp. 1193–1207, 2009. → pages 6, 7

[8] S. Salapaka, A. Sebastian, J. P. Cleveland, and M. V. Salapaka, "High bandwidth nano-positioner: A robust control approach," *Review of Scientific Instruments*, vol. 73, no. 9, pp. 3232–3241, 2002. → pages 7, 8

[9] H. Jung, J. Y. Shim, and D. Gweon, "New open-loop actuating method of piezoelectric actuators for removing hysteresis and creep," *Review of Scientific Instruments*, vol. 71, no. 9, pp. 3436–3440, 2000. → pages

[10] R. Changhai and S. Lining, "Hysteresis and creep compensation for piezoelectric actuator in open-loop operation," *Sensors and Actuators A: Physical*, vol. 122, no. 1, pp. 124–130, 2005. → pages 8, 27

[11] S. Devasia, E. Eleftheriou, and S. O. R. Moheimani, "A survey of control issues in nanopositioning," *Control Systems Technology, IEEE Transactions on*, vol. 15, no. 5, pp. 802–823, 2007. → pages 8, 30, 31, 38, 98, 117

[12] D. Croft, G. Shed, and S. Devasia, "Creep, hysteresis, and vibration compensation for piezoactuators: Atomic force microscopy application," *Journal of Dynamic Systems, Measurement, and Control*, vol. 123, no. 1, pp. 35–43, 2001. → pages 9, 19, 24, 25, 26, 27, 98

[13] M. Goldfarb and N. Celanovic, "Modeling piezoelectric stack actuators for control of micromanipulation," *Control Systems Magazine, IEEE*, vol. 17, no. 3, pp. 69–79, 1997. → pages 9, 12, 14, 15, 16, 18, 30, 31, 35, 43, 45, 57, 76, 77, 80, 100, 135, 138

[14] H. J. M. T. S. Adriaens, W. L. De Koning, and R. Banning, "Modeling piezoelectric actuators," *Mechatronics, IEEE/ASME Transactions on*, vol. 5, no. 4, pp. 331–341, 2000. → pages 10, 17, 82

[15] H. Hu, H. Georgiou, and R. Ben-Mrad, "Enhancement of tracking ability in piezoceramic actuators subject to dynamic excitation conditions," *Mechatronics, IEEE/ASME Transactions on*, vol. 10, no. 2, pp. 230–239, 2005. → pages 9, 30, 118

[16] K. K. Leang and S. Devasia, "Hysteresis, creep, and vibration compensation for piezoactuators: Feedback and feedforward control," in *The 2nd IFAC Conference on Mechatronic Systems*, 2002, pp. 283–289. → pages 9

[17] G. Clayton, S. Tien, A. Fleming, S. Moheimani, and S. Devasia, "Inverse-feedforward of charge-controlled piezopositioners," *Mechatronics*, vol. 18, no. 5, pp. 273–281, 2008. → pages 9, 26, 31, 32, 33, 35

[18] PI. (2008) Physik instrumente manufacturer specification@ONLINE. [Online]. Available: http://www.physikinstrumente.com/en/products/prspecs.php?sortnr=100810 → pages 9, 47, 49, 79, 92

[19] H. Zhou, B. Henson, A. Bell, A. Blackwood, A. Beck, and R. Burn, "Linear piezo-actuator and its applications," *University of Leeds*, pp. 1–5, 2011. [Online]. Available: http://zhouhx.tripod.com/piezopaper.pdf. → pages 9

[20] M. S. Senousy, F. X. Li, D. Mumford, M. Gadala, and R. K. N. D. Rajapakse, "Thermo-electro-mechanical performance of piezoelectric stack actuators for fuel injector applications," *Journal of Intelligent Material Systems and Structures*, vol. 20, no. 4, pp. 387–399, 2009. → pages 10, 47, 53, 133, 135, 136

[21] J. Zheng, S. Takahashi, S. Yoshikawa, K. Uchino, and J. d. Vries, "Heat generation in multilayer piezoelectric actuators," *Journal of the American Ceramic Society*, vol. 79, no. 12, pp. 3193–3198, 1996. → pages 10, 41, 133, 134, 135, 136, 140, 152

[22] L. Q. Yao, J. G. Zhang, L. Lu, and M. O. Lai, "Nonlinear static characteristics of piezoelectric bending actuators under strong applied electric field," *Sensors and Actuators A: Physical*, vol. 115, no. 1, pp. 168–175, 2004. → pages 10, 12

[23] "IEEE standard on piezoelectricity," *ANSI/IEEE Std 176-1987*, 1988. → pages 11

[24] A. Badel, Q. Jinhao, and T. Nakano, "Self-sensing force control of a piezoelectric actuator," *Ultrasonics, Ferroelectrics and Frequency Control, IEEE Transactions on*, vol. 55, no. 12, pp. 2571–2581, 2008. → pages 13, 26, 30, 57

[25] J. A. Main, E. Garcia, and D. V. Newton, "Precision position control of piezoelectric actuators using charge feedback," *Journal of Guidance, control, and dynamics*, vol. 18, no. 5, pp. 1068–1073, 1995. → pages 14, 35

[26] H. M. S. Georgiou and R. B. Mrad, "Dynamic electromechanical drift model for PZT," *Mechatronics*, vol. 18, no. 2, pp. 81–89, 2008. → pages 17, 18, 98

[27] S. Bashash and N. Jalili, "Robust multiple frequency trajectory tracking control of piezoelectrically driven micro/nanopositioning systems," *Control Systems Technology, IEEE Transactions on*, vol. 15, no. 5, pp. 867–878, 2007. → pages 17, 18, 26, 30, 40, 118

[28] H. M. S. Georgiou and R. B. Mrad, “Electromechanical modeling of piezoceramic actuators for dynamic loading applications,” *Journal of Dynamic Systems, Measurement, and Control*, vol. 128, no. 3, pp. 558–567, 2006. → pages 17, 20, 82

[29] H. Janocha and K. Kuhnen, “Real-time compensation of hysteresis and creep in piezoelectric actuators,” *Sensors and Actuators A: Physical*, vol. 79, no. 2, pp. 83–89, 2000. → pages 18, 19, 20, 27

[30] A. Wei Tech, P. K. Khosla, and C. N. Riviere, “Feedforward controller with inverse rate-dependent model for piezoelectric actuators in trajectory-tracking applications,” *Mechatronics, IEEE/ASME Transactions on*, vol. 12; 12, no. 2, pp. 134–142, 2007. → pages 18, 20, 21, 22, 23, 24, 26, 30, 40, 98

[31] U. X. Tan, W. T. Latt, F. Widjaja, C. Y. Shee, C. N. Riviere, and W. T. Ang, “Tracking control of hysteretic piezoelectric actuator using adaptive rate-dependent controller,” *Sensors and Actuators A: Physical*, vol. 150, no. 1, pp. 116–123, 2009. → pages 40

[32] D. Song and C. J. Li, “Modeling of piezo actuator’s nonlinear and frequency dependent dynamics,” *Mechatronics*, vol. 9, no. 4, pp. 391–410, 1999. → pages 18, 23

[33] H. Hu and R. B. Mrad, “On the classical preisach model for hysteresis in piezoceramic actuators,” *Mechatronics*, vol. 13, no. 2, pp. 85–94, 2002. → pages 19, 23

[34] I. Mayergoyz, “Mathematical models of hysteresis,” *Magnetics, IEEE Transactions on*, vol. 22, no. 5, pp. 603–608, 1986. → pages 20

[35] J. Peng, “Modeling and control of piezoelectric actuators,” *PhD Thesis*, 2012. → pages 21

[36] Y. Yu, Z. Xiao, N. G. Naganathan, and R. V. Dukkipati, “Dynamic preisach modelling of hysteresis for the piezoceramic actuator system,” *Mechanism and Machine Theory*, vol. 37, no. 1, pp. 75–89, 2002. → pages 23

[37] M. A. Janaideh, “Development of the rate-dependent prandtl–ishlinskii model for smartÂăactuators,” *Smart Materials and Structures*, vol. 17, no. 3, pp. 035 026–035 036, 2008. → pages 23

[38] M. Rakotondrabe, "Bouc–wen modeling and inverse multiplicative structure to compensate hysteresis nonlinearity in piezoelectric actuators," *Automation Science and Engineering, IEEE Transactions on*, vol. 8, no. 2, pp. 428–431, 2011. → pages 24, 26, 27

[39] W.-F. Xie, J. Fu, H. Yao, and C. Su, "Observer based control of piezoelectric actuators with classical duhem modeled hysteresis," in *American Control Conference*, 2009, pp. 4221–4226. → pages 24

[40] N. J. Saeid Bashash and, "Intelligence rules of hysteresis in the feedforward trajectory control of piezoelectrically-driven nanostagers," *Journal of Micromechanics and Microengineering*, vol. 17, no. 2, pp. 342–350, 2007. → pages 24, 27

[41] A. Badel, Q. Jinhao, and T. Nakano, "A new simple asymmetric hysteresis operator and its application to inverse control of piezoelectric actuators," *Ultrasonics, Ferroelectrics and Frequency Control, IEEE Transactions on*, vol. 55, no. 5, pp. 1086–1094, 2008. → pages 24, 77

[42] B. D. Coleman and M. L. Hodgdon, "A constitutive relation for rate-independent hysteresis in ferromagnetically soft materials," *International Journal of Engineering Science*, vol. 24, no. 6, pp. 897–919, 1986. → pages 24

[43] B. Mokaberi and A. A. G. Requicha, "Compensation of scanner creep and hysteresis for afm nanomanipulation," *Automation Science and Engineering, IEEE Transactions on*, vol. 5, no. 2, pp. 197–206, 2008. → pages 26, 98

[44] M. Rakotondrabe, C. Clevy, and P. Lutz, "Complete open loop control of hysteretic, creeped, and oscillating piezoelectric cantilevers," *Automation Science and Engineering, IEEE Transactions on*, vol. 7, no. 3, pp. 440–450, 2010. → pages 26, 27, 30

[45] M. Rakotondrabe, "Classical prandtl-ishlinskii modeling and inverse multiplicative structure to compensate hysteresis in piezoactuators," in *American Control Conference*. IEEE, 2012, pp. 1646–1651. → pages 26, 40

[46] D. H. Wang, W. Zhu, and Q. Yang, "Linearization of stack piezoelectric ceramic actuators based on bouc-wen model," *Journal of Intelligent Material Systems and Structures*, vol. 22, no. 5, pp. 401–413, 2011. → pages 26, 27, 30, 40, 118

[47] K. K. Leang and S. Devasia, "Feedback-linearized inverse feedforward for creep, hysteresis, and vibration compensation in afm piezoactuators," *Control Systems Technology, IEEE Transactions on*, vol. 15, no. 5, pp. 927–935, 2007. → pages 26, 30, 31, 40

[48] G. Song, Z. Jinqiang, Z. Xiaoqin, and J. A. D. Abreu-Garcia, "Tracking control of a piezoceramic actuator with hysteresis compensation using inverse preisach model," *Mechatronics, IEEE/ASME Transactions on*, vol. 10, no. 2, pp. 198–209, 2005. → pages 26, 30, 40, 118

[49] M. Rakotondrabe, Y. Haddab, and P. Lutz, "Quadrilateral modelling and robust control of a nonlinear piezoelectric cantilever," *Control Systems Technology, IEEE Transactions on*, vol. 17, no. 3, pp. 528–539, 2009. → pages

[50] A. S. Putra, S. Huang, K. K. Tan, S. K. Panda, and T. H. Lee, "Self-sensing actuation with adaptive control in applications with switching trajectory," *Mechatronics, IEEE/ASME Transactions on*, vol. 13, no. 1, pp. 104–111, 2008. → pages 26

[51] K. A. Yi and R. J. Veillette, "A charge controller for linear operation of a piezoelectric stack actuator," *Control Systems Technology, IEEE Transactions on*, vol. 13, no. 4, pp. 517–526, 2005. → pages 26

[52] B. J. G. Vautier and S. O. R. Moheimani, "Charge driven piezoelectric actuators for structural vibration control: issues and implementation," *Smart Materials and Structures*, vol. 14, no. 4, pp. 575–586, 2005. → pages 32, 100

[53] A. J. Fleming and S. O. R. Moheimani, "Improved current and charge amplifiers for driving piezoelectric loads, and issues in signal processing design for synthesis of shunt damping circuits," *Journal of Intelligent Material Systems and Structures*, vol. 15, no. 2, pp. 77–92, 2004. → pages 26, 31, 32, 35

[54] P. Ronkanen, P. Kallio, M. Vilkko, and H. N. Koivo, "Displacement control of piezoelectric actuators using current and voltage," *Mechatronics, IEEE/ASME Transactions on*, vol. 16, no. 1, pp. 160–166, 2011. → pages 26

[55] S. Lining, R. Changhai, R. Weibin, C. Liguo, and K. Minxiu, "Tracking control of piezoelectric actuator based on a new mathematical model," *Journal of Micromechanics and Microengineering*, vol. 14, no. 11, pp. 1439–1444, 2004. → pages 27

[56] S. H. Chang, C. K. Tseng, and H. C. Chien, "An ultra-precision xy/spl theta//sub z/piezo-micropositioner. i. design and analysis," *Ultrasonics, Ferroelectrics and Frequency Control, IEEE Transactions on*, vol. 46, no. 4, pp. 897–905, 1999. → pages 27

[57] S.-S. Ku, U. Pinsopon, S. Cetinkunt, and S.-i. Nakajima, "Design, fabrication, and real-time neural network control of a three-degrees-of-freedom nanopositioner," *Mechatronics, IEEE/ASME Transactions on*, vol. 5, no. 3, pp. 273–280, 2000. → pages 27

[58] P. Kallio, M. Lind, Q. Zhou, and H. N. Koivo, "A 3-DOF piezohydraulic parallel micromanipulator," in *Robotics and Automation, IEEE International Conference on*. IEEE, 1998. → pages 27

[59] K. Takagi, J.-F. Li, S. Yokoyama, and R. Watanabe, "Fabrication and evaluation of pzt/pt piezoelectric composites and functionally graded actuators," *Journal of the European Ceramic Society*, vol. 23, no. 10, pp. 1577–1583, 2003. → pages 27

[60] Y. Haddab, N. Chaillet, and A. Bourjault, "A microgripper using smart piezoelectric actuators," in *Intelligent Robots and Systems, IEEE/RSJ International Conference on*, vol. 1, 2000, pp. 659–664. → pages 27, 30

[61] N. Islam, Mohammad and R. Seethaler, "Note: Position self-sensing for piezoelectric actuators in the presence of creep and rate-dependent hysteresis," *Review of Scientific Instruments*, vol. 83, no. 11, pp. 116 101–116 103, 2012. → pages 27, 99, 109, 112, 113, 114, 115, 129

[62] I. A. Ivan, M. Rakotondrabe, P. Lutz, and N. Chaillet, "Quasistatic displacement self-sensing method for cantilevered piezoelectric actuators," *Review of Scientific Instruments*, vol. 80, no. 6, pp. 065 102–065 111, 2009. → pages 28, 31, 35, 40, 100

[63] L. E.-W. Sung, Baek-Ju and I.-s. Kim, "Displacement control of piezoelectric actuator using the pid controller and system identification method," in *Power System Technology and IEEE Power India Conference, Joint International Conference on*, 2008. → pages 30

[64] G. Gu and L. Zhu, "High-speed tracking control of piezoelectric actuators using an ellipse-based hysteresis model," *Review of Scientific Instruments*, vol. 81, no. 8, pp. 085 104–085 109, 2010. → pages

[65] E. Kouno and P. McKeown, "A fast response piezoelectric actuator for servo correction of systematic errors in precision machining," *CIRP Annals-Manufacturing Technology*, vol. 33, no. 1, pp. 369–372, 1984. → pages

[66] J. F. Cuttino, J. Miller, A. C., and D. E. Schinstock, "Performance optimization of a fast tool servo for single-point diamond turning machines," *Mechatronics, IEEE/ASME Transactions on*, vol. 4, no. 2, pp. 169–179, 1999. → pages 30

[67] W. Qiang, H. Chengzhong, and Z. Dong, "Precision control of piezoelectric actuated mechanism in scanning tunneling microscope," in *Intelligent Control and Automation , 8th World Congress on*, 2008, pp. 1262–1267. → pages 30

[68] Y. Okazaki, "A micro-positioning tool post using a piezoelectric actuator for diamond turning machines," *Precision Engineering*, vol. 12, no. 3, pp. 151–156, 1990. → pages 30

[69] M. Rakotondrabe, J. Agnus, K. Rabenorosoa, and N. Chaillet, "Characterization, modeling and robust control of a nonlinear 2-dof piezocantilever for micromanipulation/microassembly," in *Intelligent Robots and Systems, IEEE/RSJ International Conference on*. IEEE, 2009, pp. 767–774. → pages 30

[70] A. Badel, J. Qiu, G. Sebald, and D. Guyomar, "Self-sensing high speed controller for piezoelectric actuator," *Journal of Intelligent Material Systems and Structures*, vol. 19, no. 3, pp. 395–405, 2008. → pages 30, 40

[71] K. Furutani, M. Urushibata, and N. Mohri, "Improvement of control method for piezoelectric actuator by combining induced charge feedback with inverse transfer function compensation," in *Robotics and Automation, IEEE International Conference on*. IEEE, 1998. → pages 32, 35

[72] J. J. Dosch, D. J. Inman, and E. Garcia, "A self-sensing piezoelectric actuator for collocated control," *Journal of Intelligent Material Systems and Structures*, vol. 3, no. 1, pp. 166–185, 1992. → pages 33, 100

[73] S. O. R. Moheimani, "A survey of recent innovations in vibration damping and control using shunted piezoelectric transducers," *Control Systems Technology, IEEE Transactions on*, vol. 11, no. 4, pp. 482–494, 2003. → pages 33, 34, 35, 100

[74] M. Kanjuro and K. M. Junjiro Onoda and, "A self-sensing method for switching vibration suppression with a piezoelectric actuator," *Smart Materials and Structures*, vol. 16, no. 2, pp. 455–461, 2007. → pages

[75] W. W. Law, W. H. Liao, and J. Huang, "Vibration control of structures with self-sensing piezoelectric actuators incorporating adaptive mechanisms," *Smart Materials and Structures*, vol. 12, no. 5, pp. 720–730, 2003. → pages 33

[76] S. O. R. Moheimani, "Invited review article: Accurate and fast nanopositioning with piezoelectric tube scanners: Emerging trends and future challenges," *Review of Scientific Instruments*, vol. 79, no. 7, pp. 071 101–071 111, 2008. → pages 33

[77] E. Anderson, N. Hagood, and J. Goodlife, "Self-sensing piezoelectric actuation- analysis and application to controlled structures," in *AIAA/ASME/ASCE/AHS/ASC Structures, Structural Dynamics and Materials Conference, 33rd, Dallas, TX*. ASME/ASCE, 1992, pp. 2141–2155. → pages 35

[78] S. Carabelli and A. Tonoli, "System properties of flexible structures with self-sensing piezoelectric transducers," *Journal of sound and vibration*, vol. 235, no. 1, pp. 1–23, 2000. → pages 35

[79] D. G. Cole and R. L. Clark, "Adaptive compensation of piezoelectric sensoriactuators," *The Journal of the Acoustical Society of America*, vol. 95, no. 5, pp. 2989–2989, 1994. → pages 35

[80] M. Rakotondrabe, I. A. Ivan, S. Khadraoui, C. Clevy, P. Lutz, and N. Chaillet, "Dynamic displacement self-sensing and robust control of cantilever piezoelectric actuators dedicated for microassembly," in *Advanced Intelligent Mechatronics, IEEE/ASME International Conference on*. IEEE/ASME, 2010, pp. 557–562. → pages 36

[81] S. O. R. Moheimani and Y. K. Yong, "Simultaneous sensing and actuation with a piezoelectric tube scanner," *Review of Scientific Instruments*, vol. 79, no. 7, pp. 073 702–073 706, 2008. → pages 36

[82] S. Bashash and N. Jalili, "A polynomial-based linear mapping strategy for feedforward compensation of hysteresis in piezoelectric actuators," *Journal of Dynamic Systems, Measurement, and Control*, vol. 130, no. 3, pp. 031 008–031 017, 2008. → pages 40

[83] P. Ronkanen, P. Kallio, M. Vilkko, and H. N. Koivo, "Self-heating of piezoelectric actuators: measurement and compensation," in *Micro-Nanomechatronics and Human Science, 2004 and The Fourth Symposium Micro-Nanomechatronics for Information-Based Society, 2004. Proceedings of the 2004 International Symposium on*, pp. 313–318. → pages 41, 42, 136

[84] M. S. Senousy, R. K. N. D. Rajapakse, D. Mumford, and M. S. Gadala, "Self-heat generation in piezoelectric stack actuators used in fuel injectors," *Smart Materials and Structures*, vol. 18, pp. 045 008–045 018, 2009. → pages 41

[85] J. Pritchard, R. Ramesh, and C. R. Bowen, "Time–temperature profiles of multi–layer actuators," *Sensors and Actuators A: Physical*, vol. 115, no. 1, pp. 140–145, 2004. → pages 41, 133, 134, 135, 152

[86] K. Uchino, J. Zheng, Y. Chen, X. Du, J. Ryu, Y. Gao, S. Ural, S. Priya, and S. Hirose, "Loss mechanisms and high power piezoelectrics," in *Frontiers of Ferroelectricity*. Springer US, 2007, pp. 217–228. → pages 41, 133, 135

[87] P. J. Chen and S. T. Montgomery, "A macroscopic theory for the existence of the hysteresis and butterfly loops in ferroelectricity," *Ferroelectrics*, vol. 23, no. 1, pp. 199–207, 1980. → pages 41

[88] N. Islam, Mohammad and R. Seethaler, "Sensorless position control for piezoelectric actuators using a hybrid position observer," *Mechatronics, IEEE/ASME Transactions on*, vol. PP, no. 99, pp. 1–9, 2013. → pages 54, 101, 103, 104, 108, 110, 111, 121, 122, 123, 125, 126, 127, 128

[89] M. Islam, R. Seethaler, and D. Mumford, "Hysteresis independent on-line capacitance measurement for piezoelectric stack actuator," in *Electrical and Computer Engineering (CCECE), 24th Canadian Conference on*, 2011, pp. 1149–1153. → pages 57, 60, 64, 68

[90] S. Sherrit, H. D. Wiederick, B. K. Mukherjee, and M. Sayer, "Field dependence of the complex piezoelectric, dielectric, and elastic constants of motorola pzt 3203 hd ceramic," pp. 99–109, 1997. → pages 58, 82

[91] R. Seethaler and N. Islam, Mohammad, "Apparatus and method for in situ impedance measurement of a piezoelectric actuator," 2012, WIPO Patent 2,012,149,649. → pages 58, 65

[92] C. Bruce and M. Ron, *Op Amp For Everone*. Oxford, UK: Elsevier, 2009. → pages 63

[93] L. Juhasz, J. Maas, and B. Borovac, "Parameter identification and hysteresis compensation of embedded piezoelectric stack actuators," *Mechatronics*, vol. 21, no. 1, pp. 329–338, 2011. → pages 77

[94] M. Quant, H. Elizalde, A. Flores, R. Ramarez, P. Orta, and G. Song, "A comprehensive model for piezoceramic actuators: modelling, validation and application," *Smart Materials and Structures*, vol. 18, no. 12, pp. 125 011–125 024, 2009. → pages 77

[95] M. N. Islam and R. J. Seethaler, "An improved electromechanical model and parameter identification technique for piezoelectric actuators," *Journal of Intelligent Material Systems and Structures*, vol. 24, no. 9, pp. 1049–1058, 2013. → pages 79

[96] C. W. De Silva, *Vibration: Fundamentals and Practice*. Boca Raton: CRC Press, 2000. → pages 80

[97] S. Sherrit, C. M. Jones, J. B. Aldrich, C. Blodget, X. Bao, M. Badescu, and Y. Bar-Cohen, "Multilayer piezoelectric stack actuator characterization," in *Smart Structures and Materials & Nondestructive Evaluation and Health Monitoring, The 15th International Symposium on*, 2008, pp. 692 909–692 919. → pages 80, 91

[98] D.-Y. Chen and J. Phillips, "Electric field dependence of piezoelectric coefficient in ferroelectric thin films," *Journal of Electroceramics*, vol. 17, no. 2, pp. 613–617, 2006. → pages 80, 91

[99] U. Drofenik, A. Musing, and J. W. Kolar, "Voltage-dependent capacitors in power electronic multi-domain simulations," in *Power Electronics Conference (IPEC), International*, 2010, pp. 643–650. → pages 84

[100] J. A. Nelder and R. Mead, "A simplex method for function minimization," *The Computer Journal*, vol. 7, no. 4, pp. 308–313, 1965. → pages 86

[101] M. N. Islam and R. Seethaler, "Identification of constitutive parameters for piezo stack actuators based on online capacitance measurements," in *Mechatronic and embedded systems and applications, ASME/IEEE international conference on*. ASME, 2011, pp. 457–464. → pages 87

[102] D. J. Leo, *Active Vibration Control*. John Wiley and Sons, Inc., 2008, pp. 467–510. → pages 89, 90, 92

[103] PI. (2008) Physik instrumente manufacturer specification@ONLINE. [Online]. Available: http://www.piceramic.com/pdf/piezo_material.pdf → pages 92

[104] L. Jones and H. W. E Garcia and, "Self-sensing control as applied to a PZT stack actuator used as a micropositioner," *Smart Materials and Structures*, vol. 3, no. 2, pp. 147–156, 1994. → pages 100

[105] X. Li and Y. Zhang, "Analytical study of piezoelectric paint sensor for acoustic emission-based fracture monitoring," *Fatigue & Fracture of Engineering Materials & Structures*, vol. 31, no. 8, pp. 684–694, 2008. → pages 157

[106] G. Song, H. Gu, and H. Li, "Application of the piezoelectric materials for health monitoring in civil engineering: An overview," *Earth & Space*, pp. 680–687, 2004. → pages 157

[107] K. S. Hwang, S.-M. Lee, S. K. Kim, J. H. Lee, and T. S. Kim, "Micro-and nanocantilever devices and systems for biomolecule detection," *Annual Review of Analytical Chemistry*, vol. 2, pp. 77–98, 2009. → pages 157